МІНІСТЕРСТВО ОСВІТИ І НАУКИ УКРАЇНИ
ДВНЗ «УЖГОРОДСЬКИЙ НАЦІОНАЛЬНИЙ УНІВЕРСИТЕТ»

НАУКОВИЙ ВІСНИК
УЖГОРОДСЬКОГО УНІВЕРСИТЕТУ

СЕРІЯ
«ФІЗИКА»

Науковий журнал

Випуск 53
2023

УЖГОРОД
2023

ISSN 2415-8038

Засновником журналу Науковий вісник Ужгородського університету. Серія «Фізика» є ДВНЗ «Ужгородський національний університет», фізичний факультет та Закарпатське фізичне товариство

Рекомендовано до друку та поширення через мережу Інтернет Вченою Радою ДВНЗ «Ужгородський національний університет» (протокол № 7 від 20 червня 2023 р.)

Свідоцтво про державну реєстрацію друкованого засобу масової інформації
Серія КВ № 7972 від 09 жовтня 2003 р.

Журнал входить до переліку наукових фахових видань України
Категорія: Б. Науки: фізико-математичні. Спеціальності: 104 – Фізика та астрономія, 105 – Прикладна фізика та наноматеріали
(наказ Міністерства освіти і науки України від 11 липня 2019 р. № 975)

Журнал представлено у міжнародних наукометричних базах даних, репозитаріях та пошукових системах: Google Scholar, BASE, НБУ ім. В. І. Вернадського, Crossref, Scopus, OpenAIRE, WorldCat

Науковий вісник Ужгородського університету. Серія «Фізика» : наук. журн. / [редкол.: В. М. Різак (голов. ред.) та ін.]. – Ужгород : ДВНЗ «УжНУ», 2023. – Вип. 53. – 65 с.

Адреса редакції:
ДВНЗ «Ужгородський національний університет»
88000, вул. Волошина, 54, м. Ужгород
Закарпатська область, Україна
тел/факс: (03122) 3-20-24
E-mail: info@physics.uz.ua
www: https://physics.uz.ua/uk

MINISTRY OF EDUCATION AND SCIENCE
OF UKRAINE UZHHOROD NATIONAL UNIVERSITY

SCIENTIFIC HERALD
OF UZHHOROD UNIVERSITY

SERIES
“PHYSICS”

Scientific Journal

Issue 53
2023

UZHHOROD
2023

ISSN 2415-8038

The journal Scientific Herald of Uzhhorod University. Series “Physics” is founded
by Faculty of Physics, Uzhhorod National University
and Transcarpathian Physical Society

Recommended for printing and distribution
via the Internet by the Academic Council
of Uzhhorod National University
(Minutes No. 7 of June 20, 2023)

Certificate of state registration
of the print media
Series KV No. 7972 of October 09, 2003

The journal is included in the list of scientific professional publications of Ukraine
Category: B. Branch of Sciences: Physics and Mathematics. Specialties: 104 – Physics
and Astronomy, 105 – Applied Physics and Nanomaterials
(order of the Ministry of Education and Science of Ukraine of July 11, 2019 No. 975)

The journal is presented international scientometric databases, repositories
and scientific systems: Google Scholar, BASE, VNLU, Crossref, Scopus, OpenAIRE, WorldCat

Rizak V.M., et al. Scientific Herald of Uzhhorod University. Series “Physics”. Issue 53. Uzhhorod: Uzhhorod National University; 2023. 65 p.

The address of editorial board:
Uzhhorod National University
88000, 54 Voloshyn Str., Uzhhorod
Transcarpathian region, Ukraine
Tel./fax: (03122) 3-20-24
E-mail: info@physics.uz.ua
www: https://physics.uz.ua/en

НАУКОВИЙ ВІСНИК УЖГОРОДСЬКОГО УНІВЕРСИТЕТУ. СЕРІЯ «ФІЗИКА»

ВИПУСК 53

Редакційна колегія

SCIENTIFIC HERALD OF UZHHOROD UNIVERSITY.
SERIES "PHYSICS"
ISSUE 53

Editorial Board

НАУКОВИЙ ВІСНИК УЖГОРОДСЬКОГО УНІВЕРСИТЕТУ.
СЕРІЯ «ФІЗИКА»
ВИПУСК 53

ЗМІСТ

SCIENTIFIC HERALD OF UZHHOROD UNIVERSITY.
SERIES “PHYSICS”
ISSUE 53

CONTENTS

Scientific Herald of Uzhhorod University
Series "Physics"

Journal homepage: https://physics.uz.ua/en
Issue 53, 9-18
Received: 03/02/2023. Revised: 05/01/2023. Accepted: 05/29/2023

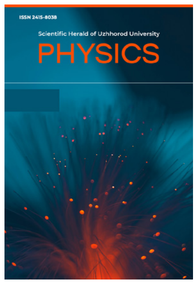

UDC 537.525, 621.793.02, 621.793.1
PACS 52.50.Dg, 52.77.Bn, 52.80.Vp, 68.37.Hk, 81.15.Ef, 81.15.Jj, 81.15.Rs, 81.65.Cf
DOI: 10.54919/physics/53.2023.09

Thermionic coating method with preliminary bombardment of the substrate surface with a stream of low energy ions

Yaroslav Hrechko*
PhD in Physical and Mathematical Sciences
V.N. Karazin Kharkiv National University
61022, 4 Svobody Sq., Kharkiv, Ukraine
https://orcid.org/0000-0001-9198-3660

Ihor Sereda
PhD in Physical and Mathematical Sciences, Associate Professor
V.N. Karazin Kharkiv National University
61022, 4 Svobody Sq., Kharkiv, Ukraine
https://orcid.org/0000-0002-9111-9853

Ievgeniia Babenko
PhD in Physical and Mathematical Sciences
V.N. Karazin Kharkiv National University
61022, 4 Svobody Sq., Kharkiv, Ukraine
https://orcid.org/0000-0001-9339-3365

Mykola Azarenkov
Doctor of Physical and Mathematical Sciences, Professor
V.N. Karazin Kharkiv National University
61022, 4 Svobody Sq., Kharkiv, Ukraine
https://orcid.org/0000-0002-4019-4933

Abstract

Relevance. Vacuum-plasma methods of applying functional coatings are widely used to increase the reliability and durability of machine and mechanism parts, cutting tools, and technological equipment, as well as in modern micro- and nanoelectronics for applying conductive and dielectric layers of various thicknesses. The study presents a method of thermionic coating that combines in one technological cycle the processes of surface cleaning by a stream of low-energy ions and plasma electron beam evaporation of a substance under conditions of thermionic plasma formation.

Aim. The research aims to determine the possibility of using the presented methodology to create and process functional coatings without radiation damage to the substrate surface.

Suggested Citation:
Hrechko Ya, Sereda I, Babenko Ie, Azarenkov M. Thermionic coating method with preliminary bombardment of the substrate surface with a stream of low energy ions. *Sci Herald Uzhhorod Univ Ser Phys.* 2023;(53):9-18. doi: 10.54919/physics/53.2023.09.

*Corresponding author

Methodology. The experimental studies were carried out in a plasma electron beam system with a primary plasma source based on an arc discharge with a filament cathode. The samples were diagnosed using a scanning electron microscope.

Results. The ion current density from the primary plasma was investigated to determine the efficiency of the surface cleaning mechanism by ion bombardment. The dependences of the ionic current density on the initial parameters of the experiment were determined. The results of the treatment of the (TiZr/TiSi) N sample surface with a plasma ion stream are presented. The obtained scanning electron microscope images showed that such treatment leads to the cleaning of the surface layer from various contaminants without damage and creates a substrate for further thermionic deposition of a coating with a high degree of adhesion. The mechanism of thermionic deposition of a titanium monolayer on a stainless-steel substrate previously cleaned by ion bombardment was studied. The revealed order of magnitude higher values of the ionic current to the substrate during the formation of thermionic plasma indicate a significant increase in the rate of the deposition process and contribute to the formation of a high-quality ion-plasma coating.

Conclusions. The scanning electron microscope images of the sample surface showed that the titanium coating during thermionic deposition was uniformly distributed over the substrate surface, without any droplet phase, which indicates the suitability of this technique for applying functional coatings without radiation damage to the substrate surface

Keywords: vacuum-plasma deposition methods; plasma electron beam evaporation; double electric layer; surface cleaning; functional coatings

Introduction

Among all the approaches currently available to solve problems of increasing the reliability and durability of machine and mechanism parts, cutting tools, and technological equipment, technological methods of surface hardening of structural materials play a key role [1-3]. According to the results of studies [4-6], the use of vacuum-plasma coating methods on structural materials makes it possible to obtain a wide range of functional coatings with predetermined properties. C. Cabral *et al.* noted that it is also important to use these methods in modern micro- and nanoelectronics to apply conductive and dielectric layers of different thicknesses [7].

Vacuum-plasma deposition methods are directly related to PVD methods [6; 8], which have many advantages [9]: coatings have improved physical and technological properties (high hardness, corrosion resistance, high temperature and impact strength, durability); the ability to use almost any type of inorganic materials for coating various groups of substrates and surfaces; low deposition temperatures (usually below 600°C); environmental friendliness. The disadvantages of these methods are the use of sophisticated equipment at a high cost; the velocity of coating is not high enough; the application technique is limited to substrates of complex geometry.

The electron beam method occupies a special place among the existing vacuum-plasma deposition methods. The studies [10; 11] noted that the essence of the method is that the kinetic energy of the electron beam used to evaporate the substance is converted into thermal energy in the treatment zone. In the classical method, the electron beam is formed by a remote electron gun, and the acceleration and focusing of the beam are achieved by electromagnetic lenses. When the electron beam is focused, this method allows for a high (up to 10^8 W/cm^2) power concentration on the target and high temperature, while ensuring a high rate of evaporation of even the most refractory materials. However, its main disadvantage is the danger of electrical breakdown arising from the transport of a powerful electron beam accelerated to 20 kV and the criticality of the accelerator system to pressure surges.

An alternative to the classical method is the plasma electron beam evaporation method proposed by the authors of [12]. In this method, the electron emitter is plasma, and the beam acceleration occurs in the near-surface layer of the space charge of the evaporated target. In this case, the heating power is controlled by both the relatively low voltage applied to the target (up to 1 kV) and the electron beam current, which depends on the plasma density. Moreover, the sample is heated uniformly from all sides, and the operational risks of electrical breakdown are not critical to pressure surges during evaporation.

An important factor in the coating process is also surface preparation, which includes, in addition to mechanical cleaning, the bombardment of the substrate surface with an intense stream of low-energy ions [13]. This method helps to heat the surface to the required temperature, removes not only all surface impurities but also ensures cleaning of the upper layer of the crystal lattice to a depth of approximately several nanometres without changing its structure. According to the results of V.A. Belous *et al.*, it can be argued that both of these effects provide a high degree of adhesion of coatings to the substrate surface and a reduction in the internal stress of the coating [14].

The research aims to investigate the possibility of using the presented methodology to create and process functional coatings without radiation damage to the substrate and improve the technological characteristics of materials. To achieve this goal, the following tasks had to be solved: to investigate the ion current density of the primary plasma at the floating potential of the object to be treated and the application of a negative bias potential to it; to study the surface of the sample bombarded with a stream of low-energy ions from the plasma; to investigate the mechanism of thermionic deposition of a monolayer on a substrate previously cleaned by ion bombardment.

Materials and Methods

Experimental studies on thermionic coating were carried out in a plasma electron beam system with a primary plasma source based on an arc discharge with a filament cathode. Figure 1 shows the general scheme of the experiment and the qualitative distribution of the potential in the system.

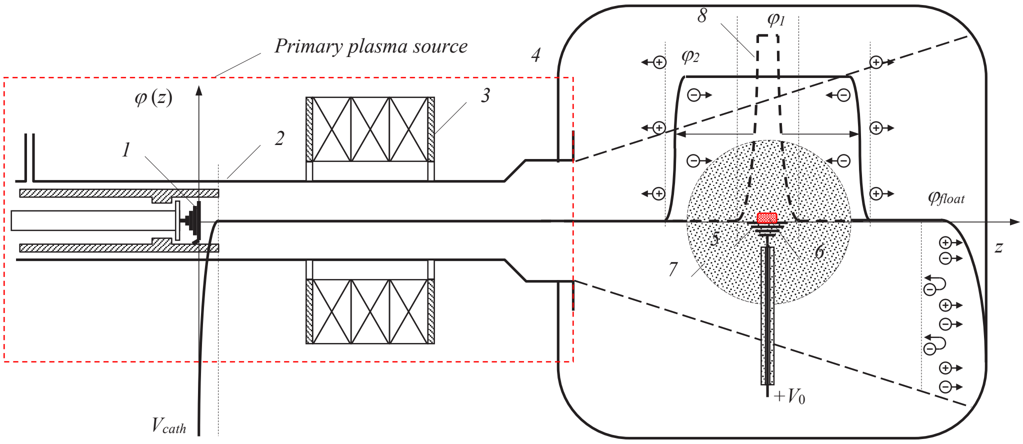

Figure 1. Scheme of a plasma electron beam system with a primary plasma source based on an arc discharge with a thermocathode and qualitative distribution of potential in the system

Note: 1 – thermocathode of the plasma source; 2 – discharge tube of the plasma source; 3 – magnetic field coils; 4 – vacuum chamber; 5 – crucible; 6 – evaporating substance; 7 – thermionic plasma; 8 – distribution of potential at the crucible, V_{cath} – potential drop near the thermocathode; V_0 – the potential supplied to the crucible; ϕ_1 – potential distribution in the bulk charge layer near the crucible; ϕ_2 – potential distribution in a double layer of space charge near the crucible; ϕ_{float} – floating potential

Source: compiled by the authors

The primary plasma source had the following design. A 2 cm diameter wire spiral tungsten direct filament cathode 1 (thermocathode) was attached to the end of a stainless-steel discharge tube 2 with an inner diameter of 4 cm and a length of 27 cm employing a vacuum electrical input. To prevent the vacuum electric input and the discharge tube from heating up under the influence of the discharge, these elements were cooled by running water passing through an outer casing. At the opposite end, the discharge tube was connected to vacuum chamber 4 employing a flange.

The discharge tube acted as an anode and was grounded, and the thermocathode was supplied with a negative potential of V_{cath}=0-400 V. The axial configuration of the anode was used to allow the charged particles to freely escape from the ionisation zone. To prevent plasma electrons from directly hitting the wall of the discharge tube, the discharge gap was in a longitudinal magnetic field. The configuration of the magnetic field was chosen to form a plasma cord that would not touch the wall of the discharge tube, and the field strength would be sufficient to maintain the plasma. As a result of the calculations, the magnetic field generated by the magnetic coil system 3 had a bell-shaped configuration with a maximum intensity of up to 600 E.

To avoid a powerful parasitic discharge between the thermocathode and the wall of the discharge chamber (under conditions of crossed electric and magnetic fields), the thermocathode was covered from the side with a copper guard, which protruded 1 cm beyond the end of the cathode. The guard spigot was connected to the external terminal of the vacuum electrical input, which provided thermal and electrical contact.

Argon was used as an operating gas. Since the operating pressure of the arc discharge with a thermocathode is more than 10^{-3} mmHg, it was necessary to inject gas into the thermocathode region to reduce the operating pressure in the vacuum chamber to 10^{-4} mmHg. The pressure gradient was formed due to the vacuum resistance of the discharge tube so that the pressure in the vacuum chamber was an order of magnitude lower than in the thermocathode area. At a pressure of 3×10^{-4} mmHg in the vacuum chamber, the plasma source formed a divergent primary plasma flux with a density near the outlet of $\sim10^{11}$ cm^{-3} at an electron temperature of $T_e\approx2$ eV.

A wire tungsten crucible 5 in the form of a spiral basket with a diameter of 1 cm, with a substance to be evaporated, 6 were located in the middle of the vacuum chamber on the same axis with the plasma source at a distance of ~20 cm from its outlet. The crucible was attached to a high-voltage vacuum input cooled by water. To reduce the surface that collects current from the plasma, the crucible leg and the entire surface of the vacuum input were covered with ceramic insulators.

The mode of electron beam evaporation with a plasma emitter of electrons was realised after applying a positive potential V_0=0-1000 V to the crucible relative to the grounded chamber. A layer of space charge with a potential drop φ_1 was formed near the crucible, in which the electrons of the primary plasma were accelerated, and an electron flux was formed, which heated the crucible. As the crucible heated up, a stream of neutral atoms of the evaporating substance was formed, some of which were ionised by electron impact. The generated ions were accelerated by the electric field of the layer towards the electrons. Under conditions when the rate of ion generation near the crucible surface reached such a value that the number of born particles exceeded the number of particles passing through the layer, a dense (up to 10^{14} cm^{-3}) thermionic plasma was formed between the layer of space charge and the crucible surface [15]. The initial layer of negative space charge φ_1 was transformed into a double electric layer φ_2 at the front of the thermionic plasma. The double layer is an effective mechanism for accelerating charged particles because it concentrates all the voltage applied to the crucible [16]. Due to the gas kinetic pressure, the thermionic plasma expanded, causing the double layer to be squeezed away from the crucible surface, increasing its surface and, accordingly, increasing the current through the layer. This expansion occurred until the conditions for the existence of the double layer were violated [17; 18]. With the disappearance of the layer, the electron beam disappeared, and the crucible heating and the formation of thermionic plasma stopped. After the collapse of the thermionic plasma, a layer of space charge was formed near the crucible again with a drop in the potential φ_1 and the whole process was repeated.

The samples to be coated were placed on a sample holder, which was a circular copper table with a diameter of 10 cm. The sample holder was located at a distance of 10 cm from the surface of the crucible. The holder was either electrically isolated from the conductive elements of the chamber and received a floating potential φ_{float}, or a negative bias potential φ_{bias}=0-1000 V was applied to it from a high-voltage power supply. A Linnik microinterferometer was used to determine the thickness of the obtained coatings. The surface microstructure of the samples was studied using a Tescan Vega 3 LMH scanning electron microscope.

Results and Discussion

The study of the mechanism of near-surface formation of an intense low-energy ion flux for preliminary surface cleaning before coating requires the study of the ion current density from the plasma created by a source based on an arc discharge with a filament cathode. The paper [19] presents the main results of this study and describes in detail the process of ion bombardment of the surface for its cleaning. Figure 2 shows the dependence of the ionic current density j_+ supplied to the sample holder on the negative bias potential of the holder φ_{bias} for different values of the discharge current of the primary plasma source i_d. The dependence was obtained at a vacuum chamber operating pressure of $p_c\sim4\times10^{-4}$ mmHg. The ion current densities at the floating potential of the holder φ_{float} ~150 V are marked with separate points on the graph. The Figure 2 shows that the application of an additional negative bias potential to the holder can significantly increase the ion current density of the primary plasma compared to the ion current density at the floating holder potential. The dependence demonstrates a linear increase in the ion current density with an increase in the negative bias potential. The ion current density also increases with an increase in the discharge current of the primary plasma source, which indicates that the current balance in the system is maintained. However, this increase is not significant at the floating potential of the holder.

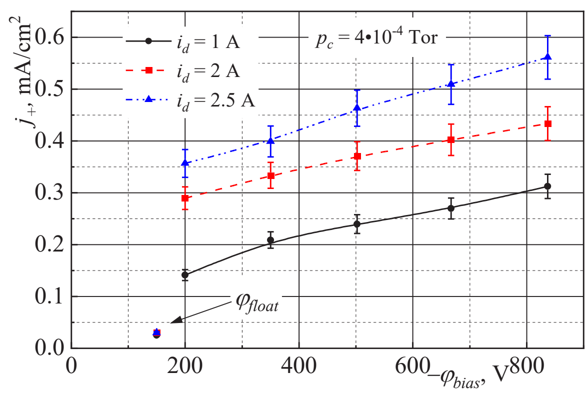

Figure 2. Dependence of the ion current density j_+ supplied to the sample holder on the negative bias potential of the holder φ_{bias} for different values of the discharge current of the primary plasma source i_d

Note: j_+ – ionic current density supplied to the sample holder; φ_{bias} – negative bias potential applied to the sample holder; i_d – discharge current of the primary plasma source; p_c – operating pressure in the vacuum chamber; φ_{float} – floating potential

Source: [19]

The operating pressure in the vacuum chamber is an important parameter in vacuum plasma coating, therefore, the effect of changing the operating pressure on the ion current density from the primary plasma was additionally studied. Figure 3 shows the dependence of the ion current density j_+ supplied to the sample holder on the negative bias potential of the holder φ_{bias} for different values of the vacuum chamber operating pressure p_c. Figure 3a corresponds to the case when the sample holder was centrally located on the same axis as the plasma source, Figure 3b – the sample holder was located at a distance of ~10 cm from the centre. It can be seen from the figures that a decrease in the working pressure in the vacuum chamber leads to a decrease in the ion current density going to the holder. The ion current density also decreases significantly with distance from the discharge axis of the plasma source. For example, when the holder is moved by 10 cm, the ion current density flowing to the holder decreases by an average factor of 4 at an operating pressure of p_c~4×10^{-4} mmHg. This indicates that when cleaning the surface of the substrate with an ion flux from the primary plasma, the sample should be located as close as possible to the discharge axis of the plasma source to obtain the highest ion current density on its surface.

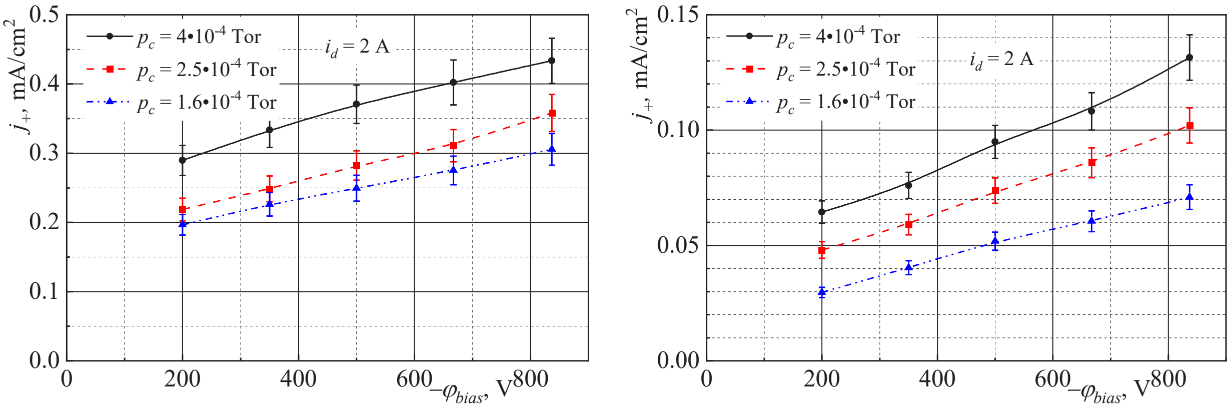

a) b)

Figure 3. Dependence of the ion current density j_+ supplied to the sample holder on the negative bias potential of the holder φ_{bias} for different values of the operating pressure in the vacuum chamber p_c

Note: a – The sample holder, located centrally on the same axis as the plasma source; b – The sample holder, placed at a distance of ~10 cm from the centre; j_+ – ionic current density supplied to the sample holder; φ_{bias} – negative bias potential applied to the sample holder; p_c – operating pressure in the vacuum chamber; i_d – discharge current of the primary plasma source

Source: compiled by the authors

In the system under consideration, to implement a technique that combines the ionic cleaning process and the subsequent thermionic coating in one technological cycle, the crucible with the substance must be located on the same axis as the plasma source so that the power of the electron beam is sufficient to create a thermionic plasma. It should also be noted that during thermionic deposition, the substrate should be at a certain optimal distance from the crucible surface so that the substrate surface does not overheat, and the resulting coating is uniformly distributed over the substrate surface with a given thickness. One of the technical solutions to effectively combine the process of substrate cleaning and subsequent coating is to use a movable holder, which, when cleaning the surface, takes a position closer to the axis of the plasma source, and when applying the coating, returns to the determined optimal distance.

Figure 4 shows scanning electron microscope (SEM) images of the surface of the (TiZr/TiSi) N sample before (*a*) and after (*b*) surface treatment with a stream of ions from the primary plasma. For more efficient surface treatment, the sample was placed on a holder located on the same axis as the plasma source. A negative bias potential of φ_{bias}=800 V was applied to the holder. The processing time was ~5 minutes. The images obtained show that the surface treatment with a stream of ions from the primary plasma leads to the cleaning of the surface layer of the sample from various impurities and contaminants without damaging its structure and can be used for further coating of the sample.

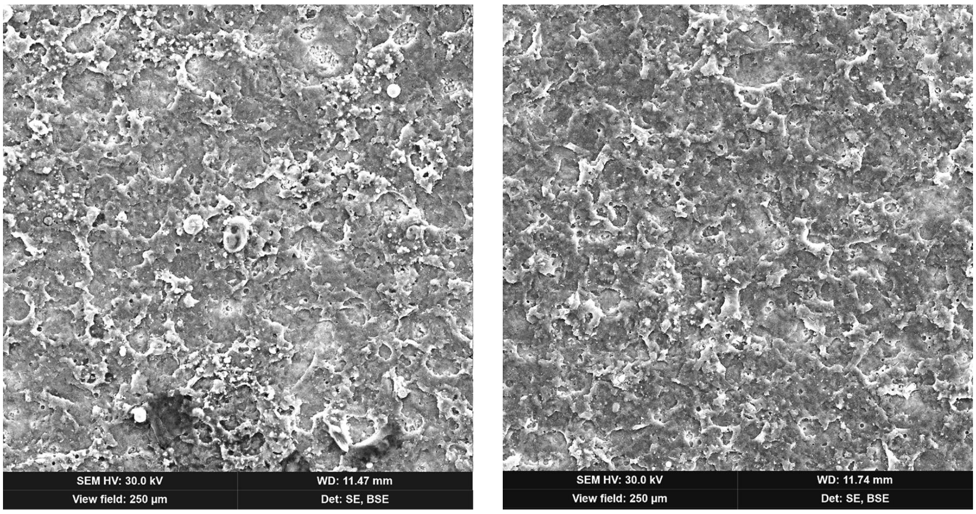

a) b)

Figure 4. SEM image of the (TiZr/TiSi) N sample surface

Note a – before surface cleaning; b – after surface cleaning by ion bombardment

Source: [19]

The next step was to study the mechanism of thermionic deposition of the monolayer on a substrate previously cleaned by ion bombardment in one technological cycle. Titanium was chosen as the evaporated material, which was deposited on a stainless-steel substrate. For this purpose, the sample was placed on a holder at a distance of 10 cm from the discharge axis of the plasma source. Pretreatment was performed by applying a negative bias potential of φ_{bias}=800 V to the holder. The processing time was ~5 minutes. After cleaning by ion bombardment, the negative bias potential was stopped and the process of thermionic deposition of the titanium monolayer began. The volume of titanium evaporated was 10 mm^3. Figure 5 shows SEM images of the surface of the stainless-steel substrate pretreated by ion bombardment (Fig. 5a) and the titanium monolayer deposited by the thermionic method (Fig. 5b). The thickness of the titanium monolayer is ~270 nm, which was determined by the interferometric method. From the images obtained, it can be seen that the titanium coating during thermionic deposition is evenly distributed over the surface of the substrate, without any droplet phase, which indicates the possibility of using this technique for the application of functional coatings with predetermined properties.

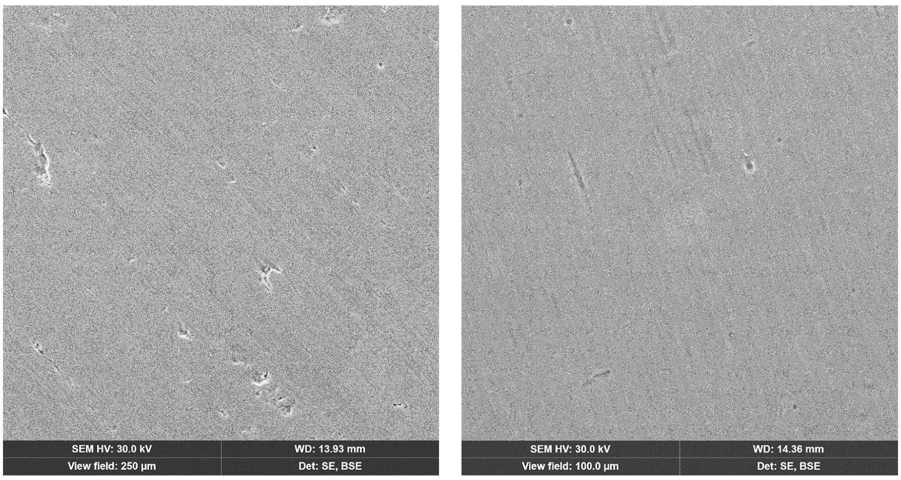

a b

Figure 5. SEM image of the surface of stainless-steel substrate and Ti monolayer deposited by a thermionic method

Note: a – surface of the substrate, pre-cleaned by ion bombardment; b – Ti monolayer deposited by the thermionic method

Source: compiled by the authors

The studies revealed an order of magnitude higher ionic current to the substrate during the formation of thermionic plasma, which indicates a significant increase in the rate of the deposition process. Figure 6 shows an oscillogram of the ionic current flowing to the sample holder. The red colour of the curve corresponds to the ionic current without thermionic plasma generation, and the black colour corresponds to the ionic current under thermionic plasma generation. The oscillogram was obtained at the discharge current of the primary plasma source i_d=2 A, the working pressure in the vacuum chamber p_c~2.5×10^{-4} mmHg. Figure 6 shows that the level of ion current flowing to the holder in the case of thermionic plasma generation is an order of magnitude higher than the ion current without thermionic plasma generation. This is since in the case of thermionic plasma generation, a double layer of space charge is formed in a self-consistent manner at the edge of the primary and thermionic plasma with different concentrations and provides an effective transfer of energy from the external electric field to the kinetic energy of the bipolar motion of charged particles [18]. The created ions are accelerated in the electric field of the double layer from the crucible surface to the vacuum chamber wall, creating an additional ion beam to the substrate surface.

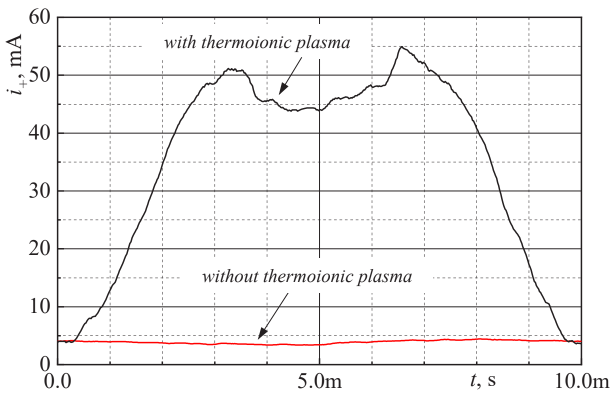

Figure 6. Oscillogram of the ionic current i_+ flowing to the sample holder at the moment of thermionic plasma generation
Source: compiled by the authors

In addition, the presence of an additional ion beam on the substrate surface confirms previous studies in this direction [12], namely, the presence of an additional mechanism for generating ions throughout the chamber volume under the conditions of development of a non-self-sustained glow discharge. The fact is that during the generation of thermionic plasma, the current to the crucible with the evaporating substance can be several times (3-6 times) higher than the discharge current of the primary plasma source. When the current to the crucible is less than the discharge current of the primary plasma source, ions are generated by the primary plasma source. This case corresponds to the red curve in Figure 6. When the current to the crucible is comparable to the discharge current of the primary plasma source, ions are generated near the crucible (formation of thermionic plasma). With a further increase in the current to the crucible, a third mechanism appears – the generation of ions in the entire volume of the chamber under the conditions of the development of a non-self-sustaining glow discharge (black curve in Fig. 6). The cathode is the wall of the vacuum chamber with a cathode potential drop sufficient to increase the generation of ions, and the anode is the crucible with the evaporating substance.

The appearance of an additional ion beam on the surface of the substrate during thermal ion deposition plays a positive role. First, as noted above, it contributes to an increase in the rate of the deposition process. Secondly, the authors of [20; 21] argue that additional ion bombardment during the coating process significantly contributes to the formation of a high-quality ion-plasma coating and significantly affects the physical and chemical properties of the sample surface. This is determined by the bombardment of the target with an additional flux of ions leads to the appearance of point defects, which subsequently become active adsorption centres [20]. The studies reported in [22; 23] were carried out in a vacuum arc evaporation system, one of the advantages of which is the high degree of plasma ionisation and the possibility of the ionised plasma affecting the surface of the samples. This ensures that the processes of cleaning, heating and formation of a metal sublayer to ensure adhesion before the subsequent plasma deposition of the coating are carried out in one technological cycle. However, the main disadvantage of this method is the presence of a droplet phase during surface treatment and coating, which is visible in the SEM images of sample surfaces presented in [22; 23]. By analogy with the vacuum-arc method, the thermionic method presented in this paper provides the creation of a dense plasma with a high degree of ionisation and the generation of an additional ion flux to the surface of the substrate. However, unlike the vacuum-arc method, the thermionic deposition does not have a droplet phase in the coatings, since this approach ensures uniform heating of the sample by electrons of the primary plasma accelerated in the near-surface layer of space charge. The obtained SEM images of the sample surface confirm this well.

Conclusions

This study presents a thermionic coating technique that combines the processes of substrate surface cleaning with a stream of low-energy ions and plasma electron beam evaporation in one technological cycle.

A characteristic feature of this technique is that the formation and acceleration of charged particle flows occur in both cases in the space charge layer.

The dependences of the ion current density from the plasma at the floating potential of the holder and the application of a negative bias potential to it are determined. It is determined that the application of an additional negative bias potential to the sample holder can significantly increase the ion current density of the primary plasma compared to the ion current density at the floating potential of the holder. It is shown that the ion current density increases linearly with the negative bias potential and also increases with the discharge current of the primary plasma source. The obtained microscopic images of the sample surface after ion bombardment demonstrate that this treatment leads to the cleaning of the surface layer of the sample from various impurities and contaminants without damaging its structure, and can be used for further coating of the sample.

The mechanism of thermionic deposition of a monolayer on a substrate previously cleaned by ion bombardment in one technological cycle has been studied. It was found that when forming a thermionic plasma, the value of the ionic current on the substrate is significantly (by an order of magnitude) higher than without a thermionic plasma, which indicates a significant increase in the rate of the deposition process. The reason for this is the formation of a double electric layer of space charge at the front of the thermionic plasma, and the emergence of an additional mechanism for generating ions throughout the chamber under the conditions of the development of a non-self-sustaining glow discharge, which was found in previous studies. The microscopic images of the sample surface showed that the titanium coating during thermionic deposition was uniformly distributed over the substrate surface, without any droplet phase. This indicates the suitability of this technique for applying functional coatings without radiation damage to the substrate surface, which will further improve the technological characteristics of structural materials.

Further research in this area involves determining the possibility of deposition of multicomponent coatings, including those with a multilayer structure, by the thermionic method on a substrate surface previously cleaned by ion bombardment. In addition, it is planned to carry out comprehensive diagnostics of the obtained coatings, namely, the study of the surface structure and cross-section, elemental composition, structural and phase state, mechanical properties and tribotechnical characteristics of the coatings.

Conflict of Interest

The authors declare no conflict of interest.

Acknowledgements

The study was carried out within the framework of the grant support project of the National Research Foundation of Ukraine “Modification of the surface of a solid under the influence of plasma and charged particle beams” (project registration number 2020.02/0234).

References

[1] Hasiy OB. The development of technology of vacuum ion-plasma evaporation and the ways of its improvement. *Sci Bull UNFU*. 2018;28(10):85-91. doi: 10.15421/40281018.

[2] Fotovvati B, Namdari N, Dehghanghadikolaei A. On coating techniques for surface protection: A review. *J Manuf Mater Process*. 2019;3(1):28. doi: 10.3390/jmmp3010028.

[3] Deng Y, Chen W, Li B, Wang C, Kuang T, Li Y. Physical vapor deposition technology for coated cutting tools: A review. *Ceram Int*. 2020;46(1):18373-90. doi: 10.1016/j.ceramint.2020.04.168.

[4] Sagalovich OV, Sagalovich VV, Popov VV, Dudnik SF. Vacuum-plasma protective coating for turbines blades. *Mech Adv Technol*. 2020;1(88):124-34. doi: 10.20535/2521-1943.2020.88.204675.

[5] Tejero-Martin D, Rezvani Rad M, McDonald A, Hussain T. Beyond traditional coatings: A review on thermal-sprayed functional and smart coatings. *J Therm Spray Tech*. 2019;28:598-644. doi: 10.1007/s11666-019-00857-1.

[6] Shahidi S, Moazzenchi B, Ghoranneviss M. A review-application of physical vapor deposition (PVD) and related methods in the textile industry. *Eur Phys J Appl Phys*. 2015;71(3):31302. doi: 10.1051/epjap/2015140439.

[7] Cabral C, Lavoie C, Murray C, Pyzyna A, Rodbell K. Thin film deposition research and its impact on microelectronics scaling. *J Vac Sci Technol A*. 2020;38(4):040803. doi: 10.1116/6.0000230.

[8] Liu MJ, Zhang G, Lu YH, Han JQ, Li GR, Li CX, *et al.* Plasma spray – physical vapor deposition toward advanced thermal barrier coatings: A review. *Rare Metals*. 2020;39:479-97. doi: 10.1007/s12598-019-01351-x.

[9] Baptista A, Silva F, Porteiro J, Míguez J, Pinto G. Sputtering physical vapour deposition (PVD) coatings: A critical review on process improvement and market trend demands. *Coatings*. 2018;8(11):402. doi: 10.3390/coatings8110402.

[10] Wang Z, Zhang Z. Electron beam evaporation deposition. In: Advanced nano deposition methods. Beijing: Chemical Industry Press; 2016:33-58. doi: 10.1002/9783527696406.ch2.
[11] Ali N, Teixeira JA, Addali A, Saeed M, Al-Zubi F, Sedaghat A, *et al.* Deposition of stainless steel thin films: An electron beam physical vapour deposition approach. *Materials*. 2019;12(4):571. doi: 10.3390/ma12040571.
[12] Mysiura IN, Girka IA, Azarenkov NA, Borgun IeV, Hrechko YaO, Hryhorenko AV, *et al.* Features of electron beam evaporation under surface electron beam formation. *Probl At Sci Technol.* 2014;6(94):149-52.
[13] Razek N, Otte K, Chassè T, Hirsch D, Schindler A, Frost F, *et al.* GaAs surface cleaning by low energy hydrogen ion beam treatment. *J Vac Sci Technol A*. 2002;20(4):1492-97. doi: 10.1116/1.1488949.
[14] Belous VA, Zadneprovskiy Y, Lomino M, Domnich I, & Bevs TI. Influence of ionic bombardment on the processes of nitriding during complex modification of steel surface. *East Eur J Phys*. 2018;4:98-102. doi: 10.26565/2312-4334-2018-4-12.
[15] Borgun IV, Zinov'ev DV, Ryabchikov DL, Sereda IN, Tseluyko AF. Dynamical accelerating structures of thermoionic plasma. *Probl At Sci Technol*. 2013;4(86):61-3.
[16] Baalrud SD, Scheiner B, Yee BT, Hopkins MM, Barnat E. Interaction of biased electrodes and plasmas: sheaths, double layers, and fireballs. *Plasma Sources Sci Technol*. 2020;29(5):053001. doi: 10.48550/arXiv.1911.06424.
[17] Yuan Z, Dong Y, Huang S, Xue Z, Yu X. Direct observation of acceleration and thermalization of beam electrons caused by double layers in the Earth's plasma sheet. *Geophys Res Lett*. 2022;49(13):e2022GL099483. doi: 10.1029/2022GL099483.
[18] Block LP. A double layer review. *Astrophys Space Sci*. 1978;55:59-83. doi: 10.1007/BF00642580.
[19] Hrechko Y, Babenko I, Sereda I, Azarenkov N. Bombardment of the surface by a low-energy ion flow accelerated in the near-surface layer of the space charge. *Probl At Sci Technol*. 2023;1(143):47-50.
[20] Shekhtman SR, Sukhova NA. Study of the influence of ion bombardment on the quality of coatings obtained by the vacuum arc deposition. In: Proceedings of the 7th International Conference on Industrial Engineering (ICIE 2021). Cham: Springer International Publishing; 2022. P. 40-6. doi: 10.1007/978-3-030-85230-6_6.
[21] Kuleshov AK, Uglov VV, Rusalsky DP. Hard and wear-resistant niobium, molybdenum carbide layered coatings on WC-Co tools produced by ion bombardment and cathodic vacuum arc deposition. *Surf Coat Technol.* 2020;395:125920. doi: 10.1016/j.surfcoat.2020.125920.
[22] Ovcharenko VD, Kuprin AS, Tolmachova GN, Kolodiy IV, Gilewicz A, Lupicka O, *et al.* Deposition of chromium nitride coatings using vacuum arc plasma in increased negative substrate bias voltage. *Vacuum*. 2015;117:27-34. doi: 10.1016/j.vacuum.2015.04.008.
[23] Zhang GP, Gao GJ, Wang XQ, Lv GH, Zhou L, Chen H, *et al.* (2012). Influence of pulsed substrate bias on the structure and properties of Ti-Al-N films deposited by cathodic vacuum arc. *Appl Surf Sci.* 2012;258(19):7274-79. doi: 10.1016/j.apsusc.2012.03.100.

Методика термоіонного нанесення покриттів з попереднім бомбардуванням поверхні підкладки потоком низькоенергетичних іонів

Ярослав Олегович Гречко

Кандидат фізико-математичних наук
Харківський національний університет імені В.Н. Каразіна
61022, майдан Свободи, 4, м. Харків, Україна
https://orcid.org/0000-0001-9198-3660

Ігор Миколайович Середа

Кандидат фізико-математичних наук, доцент
Харківський національний університет імені В.Н. Каразіна
61022, майдан Свободи, 4, м. Харків, Україна
https://orcid.org/0000-0002-9111-9853

Євгенія Віталіївна Бабенко

Кандидат фізико-математичних наук
Харківський національний університет імені В.Н. Каразіна
61022, майдан Свободи, 4, м. Харків, Україна
https://orcid.org/0000-0001-9339-3365

Микола Олексійович Азарєнков

Доктор фізико-математичних наук, професор
Харківський національний університет імені В.Н. Каразіна
61022, майдан Свободи, 4, м. Харків, Україна
https://orcid.org/0000-0002-4019-4933

Анотація

Актуальність. Вакуумно-плазмові методи нанесення функціональних покриттів широко використовуються для підвищення надійності та довговічності деталей машин і механізмів, різального інструменту, технологічного оснащення, а також в сучасній мікро- та наноелектрониці для нанесення струмопровідних та діелектричних шарів різної товщини. В роботі представлена методика термоіонного нанесення покриттів, яка поєднує в одному технологічному циклі процеси очищення поверхні потоком низькоенергетичних іонів та плазмового електронно-променевого випаровування речовини в умовах формування термоіонної плазми.

Мета. Метою дослідження було визначення можливості використання представленої методики для створення та обробки функціональних покриттів без радіаційних пошкоджень поверхні підкладки.

Методологія. Експериментальні дослідження проводилися у плазмовій електронно-променевій системі з джерелом первинної плазми на основі дугового розряду з катодом розжарення. Діагностика зразків проводилась за допомогою скануючого електронного мікроскопа.

Результати. Була досліджена густина іонного струму з первинної плазми з метою визначення ефективності механізму очищення поверхні іонним бомбардуванням. Визначені залежності густини іонного струму від початкових параметрів експерименту. Наведені результати обробки поверхні зразка (TiZr/TiSi) N потоком іонів із плазми. Отримані зображення зі скануючого електронного мікроскопа показали, що така обробка призводить до очищення поверхневого шару від різних забруднень без пошкоджень і створює підкладку для подальшого термоіонного осадження покриття з високим ступенем адгезії. Проведені дослідження механізму термоіонного осадження моношару титану на попередньо очищену іонним бомбардуванням підкладку з нержавіючої сталі. Виявлені на порядок вищі значення іонного струму на підкладку при формування термоіонної плазми свідчать про суттєве підвищення швидкості процесу нанесення та сприяють формуванню якісного іонно-плазмового покриття.

Висновки. Отримані зображення поверхні зразка зі скануючого електронного мікроскопа показали, що покриття титану при термоіонному нанесенні рівномірно розподілене по поверхні підкладки, без наявної крапельної фази, що свідчить про придатність даної методики для нанесення функціональних покриттів без радіаційних пошкоджень поверхні підкладки

Ключові слова: вакуумно-плазмові методи нанесення; плазмове електронно-променеве випаровування; подвійний електричний шар; очищення поверхні; функціональні покриття

Scientific Herald of Uzhhorod University
Series “Physics”

Journal homepage: https://physics.uz.ua/en
Issue 53, 19-30
Received: 02/20/2023. Revised: 04/30/2023. Accepted: 05/15/2023

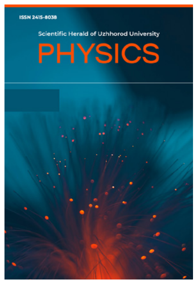

UDC 535.41
PACS 42.25.Hz
DOI: 10.54919/physics/53.2023.19

The scientific process of two interferometers (optical) development and the mitigation of external influence

Vitaliy Panov*

Senior Researcher
Dnipropetrovsk Department of the All-Union Research Institute of Mining and Rescue
49000, Heroiv Maidanu Sq., Dnipro, Ukraine
https://orcid.org/0000-0002-2672-7748

Abstract

Relevance. The research relevance is predefined by the fact that the presented object of analysis, namely the interferometer, plays an important role in modern science in obtaining accurate measurements and their results, which sets the requirements for improving interferometers and eliminating external influences.

Purpose. The research aims to analyze the progress of the development process of two interferometers, which are used in many scientific spheres, especially in optics, and play an important role in accurate measurement results of research, as well as finding new and effective technologies to eliminate external influences.

Methods. Among the methods used are an analytical method, logical analysis method, functional method, statistical method, synthesis method, and others.

Results. Throughout the study, two compensators and the differences between them were noted, and the features of these compensators’ operation and their reliability were also analyzed. The negative factors that prevent more accurate measurements by interferometer were identified, and the most damaged elements in interferometers and their causes of damage were also identified. It is important to analyze the functioning of interferometers and compensators, and their operating conditions to assess the degree of efficiency, relevance, and progress in optics. The issues of evaluation of the development and problems of two schemes of interferometers with trapezoidal and square beamsplitters were also considered, and recommendations were proposed that would contribute to a more effective mechanism for regulating this issue.

Conclusions. It was determined that the process of developing new generation interferometers and eliminating external influences on them plays a crucial role in the development of optics, significantly affecting the progress in this area. The practical value lies in the application of the identified results, solving the problems of the process of developing interferometers and their progress in operation, taking into account various external influences, which will help to change the scheme of approach to the development of this mechanism and increase resistance to negative external influences

Keywords: compensators; measurements; negative factors; schemes; beam entry

Suggested Citation:
Panov V. The scientific process of two interferometers (optical) development and the mitigation of external influence. *Sci Herald Uzhhorod Univ Ser Phys.* 2023;(53):19-30. doi: 10.54919/physics/53.2023.19

*Corresponding author

Introduction

In modern science and technology, the requirements for accurate measurements by interference methods are rapidly growing and require the improvement and development of new innovative interferometers. To solve certain measurement problems it is possible to use only these methods and the interferometer. The problems of the interferometer development process and the elimination of external influences are associated with insufficient attention to engineering issues and their theory at the design and development stage, poor research of the causes that reduce the efficiency of this device, expensive materials of elements that are components of the interferometer. Following Yu.V. Kolomiytsov [1], the field of interference devices has significantly expanded due to the creation of new light sources (lasers) and the development of electronics. It is important to precisely control the thickness of nanoscale films of transparent materials during their application to the substrate during the development and manufacturing technology of various optoelectronics devices and optical nanosensors. For example, laboratory research in the chemical and pharmaceutical industries and ecology, in particular for air quality monitoring, uses highly sensitive devices based on the phenomenon of surface plasmon resonance and gas analysis.

As pointed out by Z. Chen *et al.* [2], interferometers are devices that are widely used for quantitative phase analysis to record small differences in optical arm lengths and control them with an accuracy of fractions of wavelengths of light radiation. The high sensitivity of the devices also has negative aspects. Thus, random changes in air pressure and temperature can cause changes in the indicators, and even very small fluctuations in temperature, air movement, and mechanical vibrations of the structure can lead to shifts that introduce noticeable random and systematic errors in the measurement results. Following B. Chen *et al.* [3], interferometers allow size measurements by comparing them with a natural constant, the wavelength of a frequency-stabilized laser, the laser radiation is a very close approximation to an ideal monochromatic wave. The accuracy of measuring the length of this fundamental physical quantity depends on the level of development of science and has a significant impact on progress in industrial technologies.

M. Hu *et al.* [4] note that the device for measuring interference lengths consists of two elements, an interferometer and an electronic system for calculating interference bands and processing measurement results. The analysis of laser interferometer interference circuits shows that in the practice of length measurements, a two-beam Michelson-type interferometer, the moving element of which is firmly connected with the object to be measured, is actively used. To eliminate the errors that are directed to the parameters of the interference field, the moving mirror is provided in the form of an angular reflector. Following H. Zhang *et al.* [5], some features and capabilities of interferometers used in optics are calculated by the Jones method, this method is mainly used to calculate many properties, but most often polarization. To calculate the polarization properties in the scheme, it is necessary to have the polarization azimuth that can be found from the matrix values. This method is used in many devices, but most of all in ballistic gravimeters.

The purpose of the research is to perform an objective analysis to identify problems in the process of developing interferometers and eliminate external influences at the present stage of optics development. This goal will provide an opportunity to develop effective interference methods to improve the accuracy of measurements and calculations in scientific research.

Material and Methods

Research in the field of studying the problems of the scientific process of developing two interferometers and eliminating external influences on these objects was performed by applying methods that reveal the theoretical and practical significance of the object of study. The method of logical analysis helped to identify the problems of the development process of interferometers in optics considering external influences. The statistical method was applied to consider the main indicators, which in turn help to analyze the prospects of interferometers development, the implementation of this process and the improvement of the quality of materials of parts that make up the interferometers, the importance of innovative interferometers in various fields, especially in optics, thanks to which the process of efficiency of the development of this mechanism and its prospects were determined. Using the functional method, the role and essence of interferometers in optics and other areas, their advantages, and disadvantages, as well as the impact and contribution of the device in the development of modern scientific research for more accurate measurements were analyzed. One of the empirical methods, namely the method of modular inspection, was used, the negative factors that prevent more accurate measurements by interferometer were identified, the most damaged elements in interferometers and the process of efficiency of the development of this mechanism and its prospects were also identified, the issues of evaluating the development and problems of two schemes of interferometers with trapezoidal and square beamsplitters were also considered, drawings of interferometers according to the new scheme were proposed and provided.

The structural-functional method helped in the analysis of trends, factors, and models of interferometer elements, which determined that solving problems with the development process of interferometers, with the improvement of measurement results in scientific research using interference methods, with the reduction of external influences and the definition and optimization of interferometer performance at the design, modeling and development stages in the field of optics, will require an increase in funding, a new approach to the system of manufacturing and a new approach to the production of interferometers. The method of deduction helped in the disclosure of the concept of“interferometer” through the prism of highlighting the characteristic features for a full analysis of the work and problems of this mechanism. Applying the method of synthesis, the obtained results of theoretical and practical nature are summarized to provide recommendations that contribute to solving problems and improving the efficiency and prospects in the design and development of interferometers and their parts, especially in optics and other fields in which interferometers are used for measurement.

As such, the research will be divided into several stages. The first stage was to reveal the theoretical aspect of the work, namely, to define the concept of “interferometers”, and to analyze the characteristics and principles of this mechanism; especially in optics. In the second stage, the study of the mechanism and problems of the approach to the scientific process of developing interferometers and components, their advantages and disadvantages, the functioning of this mechanism in various fields, and the analysis of the activity of this object in optics and its importance in accurate measurements was carried out; an important step of this stage was to analyze the process of designing and developing interferometers in optics, the implementation of the development of new approaches and technologies to the design of innovative models of interferometers, the means of eliminating external influences or its partial decrease. The third stage, based on the identified results of theoretical and practical content, identified problems and recommendations for the development of this mechanism and its components, which will contribute to the solution of issues and development in many areas for more accurate measurements.

Results

To ensure accurate measurement results in modern scientific research, it is necessary to develop scientific processes of development of all devices, including interferometers, with the help of which measurements are carried out in all areas. The general scheme of the interferometer structure is shown in Figure 1.

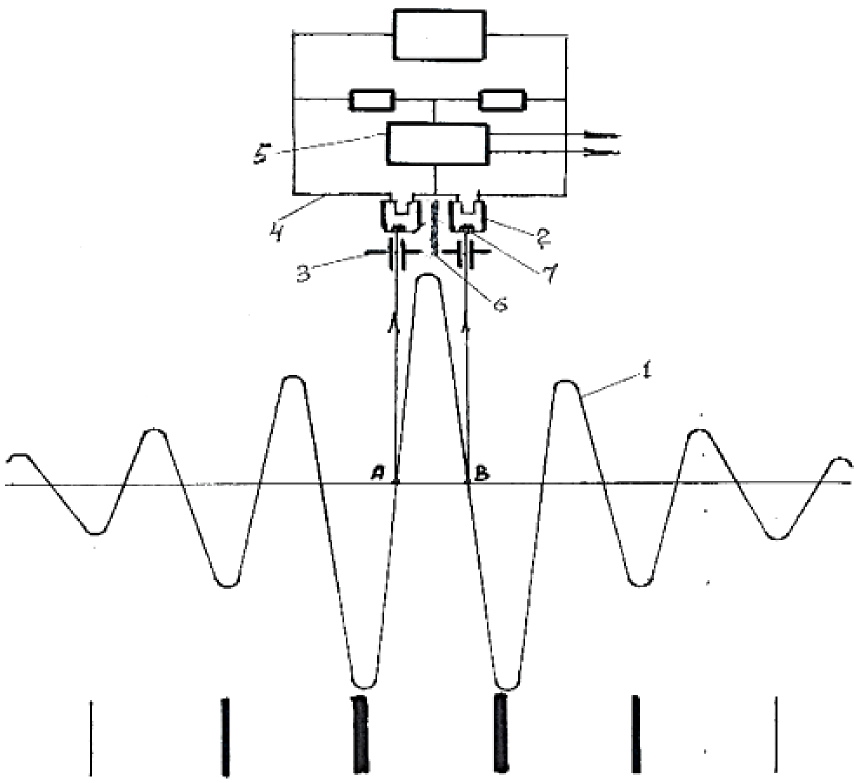

Figure 1. Interferometer with a light characteristic of the interference pattern

The interferometer consists of 1 – camera, 2 – isosceles pentaprism with an angle of 90° at the base and top, 3 – BR prism – 180°, 4 – triangular prism, 5 – parallelogram prism, 6 – light source, and 7 – lens. Mirrors are applied at the ends of a thin transparent plane-parallel plate, the middle part connected to the square faces, towards the camera, parallelogram, and through prisms. On the base of the beam splitter from the center, in opposite directions, with the front faces in the same plane, the bases are installed in the direction of the prisms: isosceles pentaprism, parallelogram – triangular prism. This connection of prisms is a light-emitting unit.

Interferometers have various applications, including length measurement, control of the shape and micro geometry of surfaces, research of optical systems and aerodynamic flows, measurement of refractive indices of substances, spectral studies, and tension measurement. This highlights the range of interferometers being broad, so the process of developing this object is an important issue to be solved. Interferometers are designed according to a new blueprint. The blueprint consist of two compensators, one compensator, HIBRID, in the presence of an interference pattern with horizontal stripes, uses plates from different compensators: the Jeumann compensator works in the vertical plane, and the Panov compensator in the horizontal plane. The second compensator – Panov – shifts the beams in the horizontal plane from the center, in opposite directions. Both compensators create an interference pattern in the horizontal plane relative to the base with vertical stripes that reduce the external influence. The development of scientific methods for solving the problems of designing and modeling interferometers in scientific research is carried out by scientists and engineers from many countries of research and design organizations. For the development of various optoelectronics devices and optical nanosensors, it is important to have control of the film thickness, which is carried out by the photometric method based on the interference of waves in the film without absorption, the film thickness is proportional to the wavelength. An automatic interferometer for cutting off the explosive concentration of methane, tuned to ¼ of the achromatic band of the interference pattern [6], contains the following positive qualities monotonicity of illumination in the entire range, two working photodetectors, the absence of negative phenomena of “pass” and “shift” of the color of the bands, high sensitivity, linearity of the scale, manometric method of graduation by water column and small chamber length: the upper limit is 100 vol% length of 1 mm, 4 vol% – 12 mm for methane with double passage of the rays.

The disadvantages of this interferometer are low brightness and contrast of the interference pattern and sensitivity to external influences. The interferometer used a beam splitter in the form of a rectangular prism mounted at an angle of 45° to the rays of the light source with a translucent layer. In this beamsplitter, large light losses due to multiple reflections and the ends of the strips are highlighted by “glare”, which in turn reduces the contrast and increases the use of diaphragms.

The issue of improving the process of development and elimination of external influences of interferometers, to reduce their shortcomings in the work and their problems of application in scientific research are becoming increasingly relevant and of practical value. The analysis of this mechanism at the design and modeling stages depends especially on careful observation of the operating personnel to avoid errors and to consider external influences that may further cause defects. There are two types of beamsplitters: a trapezoidal one consisting of two prisms, a parallelogram, and a triangular passing one, connected through a translucent layer, and a square beamsplitter consisting of two equal triangular prisms connected through a translucent layer, this beamsplitter is used in Michelson interferometer [7]. The beamsplitters have a common point of separation and assembly of paired interfering beams, which can reduce the size into an interference pattern that is twice as bright and contrasty as the rectangular one.

In this complex process, the revision of the modeling and development problems of beamsplitters and interferometers in general and their solution is of particular importance, since the development of innovative devices and technologies for high-quality scientific research in various fields in the country is one of the urgent problems of our time. Passive stabilization of the Michelson interferometer, which is designed to work as part of a laser emitter of ultrashort pulses, can increase the stability of a laser resonator with a controlled Michelson interferometer by using original interferometer circuits containing refractive and mirror optical elements.

As a whole, the problem of optimization of effective and qualitative elimination of external influences is not completely solved in modern interferometer developments. Laser interferometry is a technology for ultra-precision processing, integrated circuit manufacturing, precision metrology, and many other scientific research. In laser interferometry, the phase demodulation technology largely determines the performance of displacement measurement, and this technology is also widely used in optical interferometers due to its high sensitivity, wide dynamic range, and tight protection against external factors that negatively affect it.

Two interferometer schemes were developed: with a trapezoidal beam splitter [8] and with a square beam splitter [9]. The trapezoidal interferometer is shown in Figure 2.

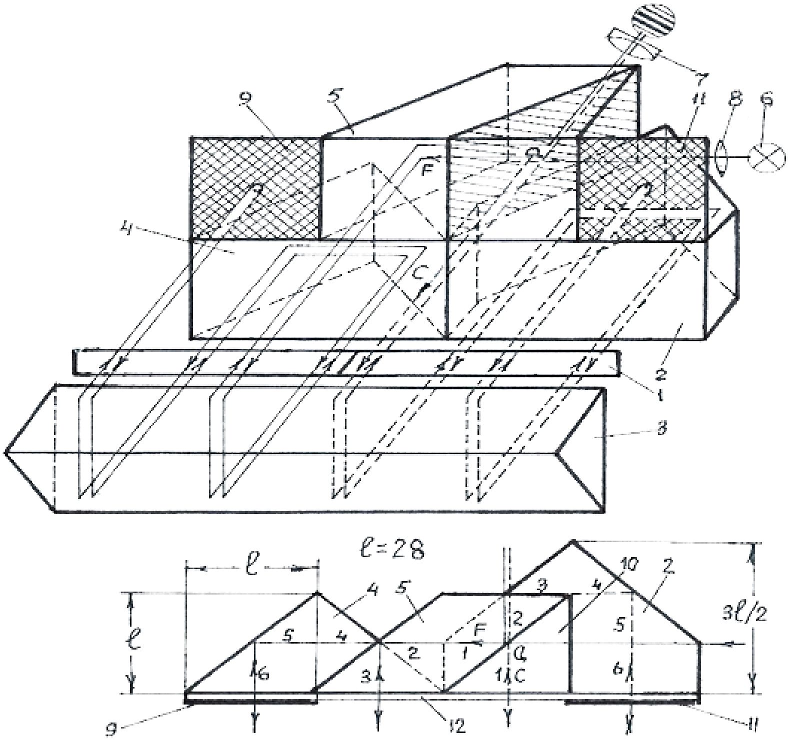

Figure 2. Trapezoidal interferometer with interference beam path

Number 1 – camera, 3 – BR prism – 180°, 4 – triangular prism, 6 – light source, 7 – lens, 8 – condenser, 9 – beam mirrors I, 10 – triangular passing prism, 11 – beam mirror II. Mirrors are applied at the ends of thin, transparent plane-parallel plates, the other ends of the plates are connected with square faces, towards the cameras, 14, 10 – equal triangular prisms. On the base of the beam splitter from the center, on opposite sides, there are two equal triangular prisms – 4, 13, with hypotenuse faces in the same plane and towards the chambers, with heights equal to the length of the sides of the square. Triangular prisms – 4, 13 are interconnected by mirror catenary faces, mirror towards the chambers.

Since the projections of the block have four squares on all sides, the unit of measurement is a square, it can be assumed that the length of the side of the square is l. So, a square beam splitter with sides l, hypotenuse face: length – 2l, height – l, prism heights – 4, 13 – l, between the rays – l, 9, 11 mirrors l by l. Substituting the length of the sides of the square l=25 mm (Fig. 3), it can be found the dimensions of the light unit and the entire interferometer.

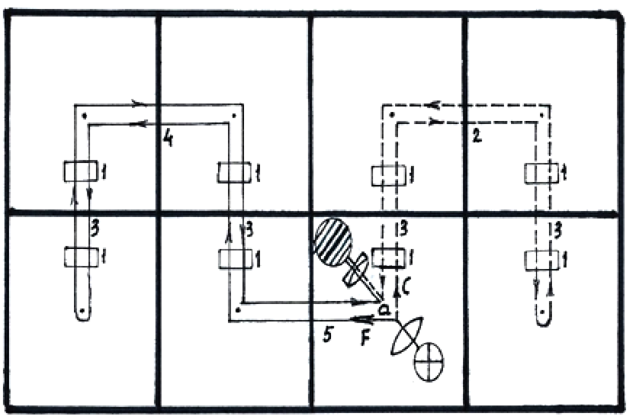

Figure 3. Projection of the light unit of the Panov interferometer with the course of the central rays

The production of interferometers and the application of interferometric methods has a long practice of being used both in international and Ukrainian experiments than the production and application of devices and methods with similar properties of work. For example, seismic interferometry can significantly reduce the influence of the source due to interference between seismic signals. This method can be used to process high-speed seismic signals and image the subsurface structure. Interferometers are susceptible to damage due to external influences, most often due to the base, which is made of invar, a metal alloy that is insensitive to external influences. When measurements are carried out by an interferometer, the wave displacement of the measured value converges to the value of the external influence with which it coincides in direction.

Currently, in many areas of scientific research, interferometry methods are the most widely used and developed [10]. In modern scientific research, interferometers are used, the radiation of which occurs with the help of two sources with a large difference in wavelengths, they are distributed in one way, and these waves can be represented by two types.

For the error signal to occur in the channel with short-wave radiation, the feedback method is used, the phase advance in the plasma is very small, and the systems in the interferometer, where the phase advance in the plasma deviates from the phase advance, caused by a change in the size of the interferometer measuring base due to the mathematical processing of signals registered in the measuring channels. Interference lines formed from pairs of equal optical length interference beams passing through the same interferometer device are identical, their zero lines are at the same point of the interference pattern and represent the same strip width. As a result, it is possible to obtain an increase in the brightness of the picture without reducing the diversity. A general interference pattern is obtained.

The prerequisite for the reliable functioning of the interferometer is to ensure stable operation and quality design of both some elements and the device as a whole. In the Michelson-type interferometer, the optical decoupling of the laser resonator and the interferometer is performed by standard polarizing elements or by separating the place of separation and recombination of the interfering beams.

For the comparative evaluation of two interferometers according to this scheme, an interferometer with a square beamsplitting prism was developed (Fig. 4). The length of the sides of the square is l=25 mm.

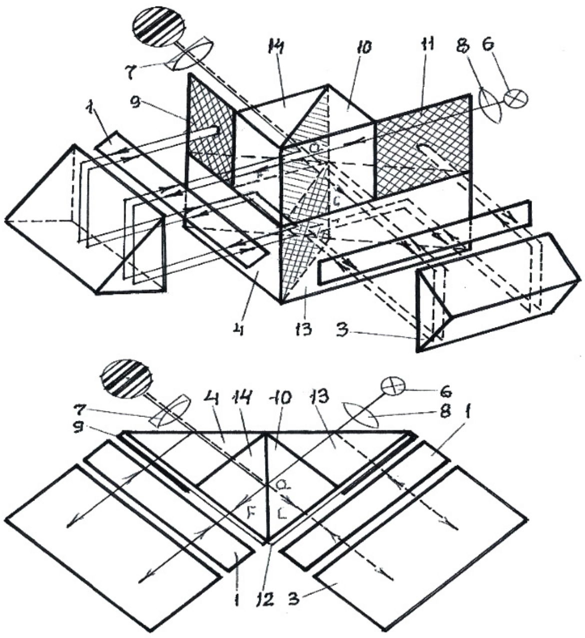

Figure 4. Square interferometer with the interference beam path

Solving the issues of developing an innovative and multifunctional interferometer requires the introduction of effective tools for modeling and designing quality elements of this mechanism. The methods that are still used to calculate the properties of interferometers are outdated and irrelevant, as innovative devices require more accurate calculations, without improving methods or introducing new ones, the operation of these interferometers will not be effective and accurate.

The interference pattern with horizontal or vertical stripes is arranged and rotated 90° in the vertical focal plane. The picture with horizontal stripes is located vertically along the length of the plane. Therefore, during measurements, the direction of displacement of the measured value of the horizontal stripes 15 is directed (the stripes are displaced along the picture) perpendicular to the base, parallel to external influences 16. perpendicular to the base. When measured, both values are added.

With the rotation of the interference beams of the horizontal strips by 90° through the compensator plates, the HIBRID rotates, and the interference pattern by 90°, which is horizontal along the length in the focal plane, and the strips are vertical relative to the substrate. The displacement of the strips from the measured value is constant along the base, it is added to the magnitude of the external influence directed along the base. This influence is small. The external influence of perpendicular pressure on the base does not return with the rotation of the rays by 90°. During measurement, the external influence slightly moves the vertical bars on the scale. The displacement of the bars does not affect the measured value. The width of the achromatic line of horizontal and vertical stripes is equal. To have vertical stripes in the presence of an interference pattern with horizontal stripes (Fig. 5), the HIBRID compensator is used, plates (thickness 0.2÷1.0 mm) of different compensators: Jeumann compensator – works in the vertical plane and Panov compensator – works in the horizontal plane. The rays (t. F, C) are shifted utilizing the compensator plates. For example, the beam t. F goes down – F1 (Joumain), and the beam of t. C is shifted to the right – C1 (Panov) until the width of the achromatic bands is equal. The interference pattern (t. F1 C1) with vertical stripes is obtained. The direction of displacement of the measured value 15 was rotated by 90°, and the direction of perpendicular influence on the base (external influences) – 16 – did not change [11; 12].

The interferometer (Fig. 5) with the help of the prism BR – 180° angle ß was tuned to horizontal bands with a given width of the achromatic band. The HIBRID compensator was used to obtain vertical bands.

The HIBRID compensator acquired vertical stripes. “0” was set at horizontal and vertical bands. At constant mechanical impact on the interferometer body with vertical stripes, there was no “0” offset. Without removing the mechanical impact, the compensator is removed. With horizontal stripes “0” shifted by 0.25 scale. From the measuring gas chamber, the displacement of the vertical and horizontal bands was equal. The difference between the variants of vertical strips from each other is that the wave displacement of the measured value is directed along the scale to the right or left along the base, and the displacement from external influences is directed perpendicular to the scale and the base. The displacement of horizontal stripes from both influences is directed along the scale, perpendicular to the base [13].

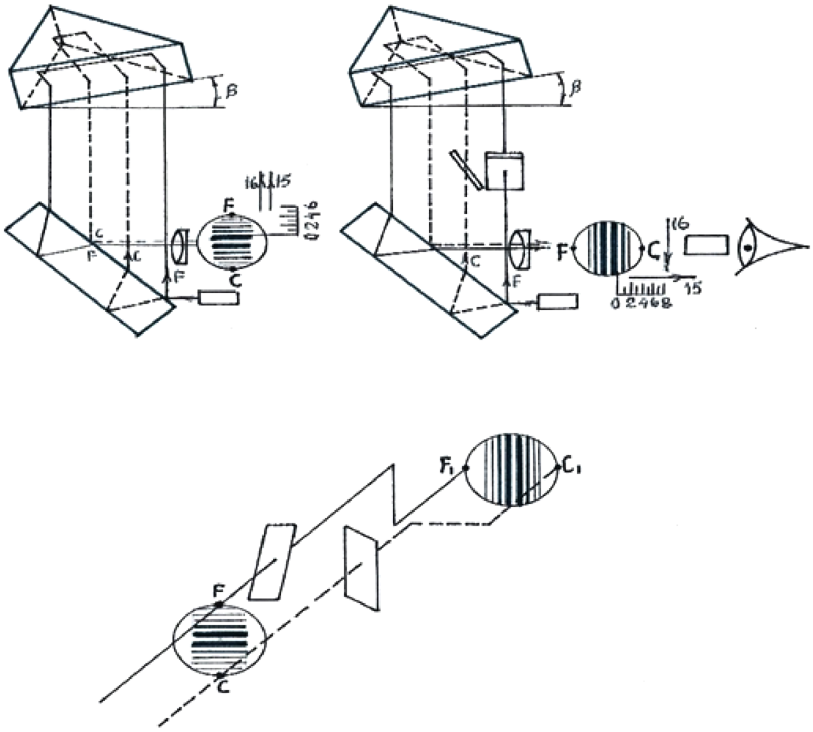

Figure 5. Obtaining vertical stripes with horizontal stripes

Item 17 in the figure – transparent plates with a thickness of 0.2÷1.0 mm, 18 – the base, ɣ – the angle of the width of the vertical stripes, ß – the angle of difference of the interference beams. Each plate is rotated in opposite directions in the horizontal plane relative to the center by an angle ɣ. The angle ɣ is set so that the width of the achromatic band is equal to the calculated one. For the latest modifications of interferometers of the AI type, the angle is equal to – 12° at a plate thickness of 1 mm [14]. In the second method of obtaining vertical stripes without an interference pattern, the Panov compensator (Fig. 6) [8; 9] is used.

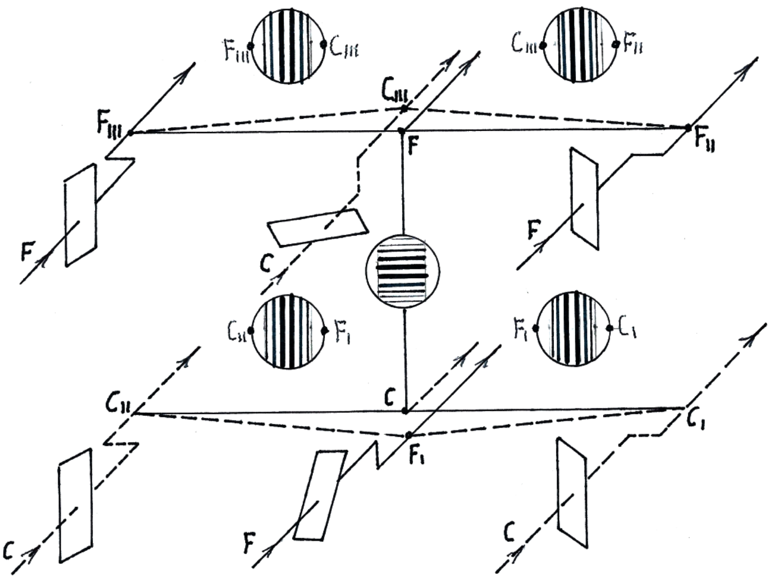

Figure 6. Panov compensator
Source: [8; 9]

Turning the plates symmetrically relative to the center on opposite sides, the width of the achromatic band is set. Between the rays of the horizontal plane, an interference pattern with vertical stripes with the above properties is formed. The compensator plates are in a vertical position, touching each other with the ends (center) and planes perpendicular to the interference rays and the center between the rays.

The development and modeling of affordable and multifunctional interferometers in real-time will allow us to bring the process of solving these problems to a new level in terms of the speed of the solution and the quality of the results obtained.

Discussion

The quality of measurements with the help of an interferometer depends on the correct production and its efficiency is one of the most urgent issues of modern science in many countries, and some problems require an immediate solution. The development of many modern spheres of science and technology requires improvement of ways to eliminate external influences of some devices and their elements and error-free diagnostics of these mechanisms. In the presence of interference patterns, vertical or horizontal stripes can be obtained. The difference between the variants of vertical bands from each other is that the wave displacement of the measured value is directed along the scale to the right or left along the base, and the displacement from external influences is directed perpendicular to the scale and the base. The displacement of horizontal stripes from both influences is directed along the scale, perpendicular to the base.

Studies carried out in recent years of the operation of interferometers and the most damaged elements of these devices allowed a better assessment of the impact of the environment on this mechanism and identify their main causes and damage to the elements that make up the object. Based on the results of recent studies by B. McKinley *et al.* [15], frequency reproducibility is an important characteristic, but for linear measurements, it is necessary to have an absolute value of the wavelength of emission, or as it is also called the absolute frequency of optical emission. The radio frequency bridges are used to measure the absolute optical frequencies, they are used to measure the frequency of lasers in the optical range. But the use of this experimental equipment is very expensive. This demonstrates that the design, modeling, and development of innovative interferometers and methods can provide more opportunities in various fields of research, it is necessary to increase financial support for the use of high-quality experimental facilities.

In different points of the interference field in which the interference pattern is observed, the phase difference sometimes has different values. To obtain interference, it is necessary that the phase difference of the oscillations, which are formed, remains the same during the time of observation or research.

It is worth noting that following modern international scientists and experts in the development of design and modeling of interferometers, Ukraine has made a major step forward over the past few years, and the demand for this device has also increased. Referring to the definition of Y. Pu & S.A. Cummer [16], heterodyne interferometry (HDI) based on three-wavelength photomixing, the HDI method can help to critically increase the sensitivity to small amplitudes of laser Doppler vibrometers and increase their noise immunity, in interference refractometers, as the investigated parameter is the phase of optical radiation, so the developments of HDI can be applied in refractometric measurements. The whole mechanism of the heterodyne interferometry method was analyzed, and as a result, it was decided that the disadvantage of this method is a large percentage of nonlinearity, which limits the measurement range, but it can be compensated, it is also necessary to monitor the stability of the chosen amplitude ratio, and to reduce the negative external influence, to have wave propagation in close conditions.

It is necessary to focus on the state of the devices used for this method and to determine the reason for the percentage of nonlinearity, it will help to highlight the problem and find an effective solution. The scientific process of developing interferometers in real time generates more and more new technical solutions for the implementation of the tasks, until recently, a large number of measurement results of scientific research in many areas were not available, since the existing devices were quite bulky and expensive.

It is important to note that the development of the next generation of interferometers will not be able to eliminate negative external influences or predict new ones. Researchers R.X Adhikari *et al.* [17] determined that some studies have provided the current characteristics, development rate, and development form of interferometers through observation and analyzed the process of self-sustained development of this device, but the research on the evolution of the initial stage to self-sustained development is still very limited. Furthermore, although the interferometer can accurately observe the initial stage of lightning at close range, the current location method has some errors in determining the location of the close-range discharge breakdown, which needs further improvement. The method of calibrating the positioning error of the interferometer for a specific close-range radiation source can be applied to avoid inaccuracies and some errors in measurements. It is very important to consider the importance of the proper study of these errors and their causes for further prospective development of interferometers. There is an assumption that the distance from the emission source to the interferometer is much larger than the reference length. If the emission source is near the interferometer, the assumption of a plane wave will bring some errors.

During the calculations in the development of interferometers and their elements in production facilities, considering external influences, models of this mechanism should adequately describe the process and be simple and realizable. K. Patel *et al.* [18] determined that the intensity distribution in the spot of the output emission was close to Gaussian, the output power level in the classical Michelson interferometer when tuned to the maximum intensity of the zero field was usually 0.2-0.3 W, which was about half the power level using the original Michelson interferometer, the long-term stability of the original Michelson interferometer was high and did not require its placement in an additional housing. This interferometer was analyzed and studied more precisely, and a comparison of the original and classical Michelson interferometer was made, it was found that such results of the classical interferometer could be due to an increase in the active losses of the resonator due to an increase in the number of reflections from the constituent optical coatings, or because during this study some decrease in efficiency was noted compared to the original interferometer.

A big role in the feasibility and usefulness of this device for customers is its small size, the development of a device with greater capabilities and new properties, low cost, and the elimination of some external influences, at the moment there are very few interferometers developed that meet such criteria due to insufficient attention to these mechanisms, so it is necessary to intensify the development of interferometers and bring it to a new level. W. Kim *et al.* [19] showed by his works that the increased stability of the refractive interferometer has the following advantages over the traditional one simplicity and reliability of adjustment, no need for angular adjustment of the elements, the possibility of precise alignment without a piezo transducer, which is an element sensitive to random acoustic noise, reduced sensitivity to microscopic translational movements of the elements and vibrations of the surrounding air, since the beam trajectories in both arms are the same, testing the interferometer in the passive mode allows us to expect reproducible and stable results in the controlled mode as a component mirror of a solid-state laser resonator emitting ultrashort pulses. It was determined that this interferometer allows the solution of many issues that could not be solved with the help of old-generation interferometers, and will also be able to popularize this mechanism in many areas for high-quality measurements due to its stability and multi-functionality.

Professional development of the personnel who design and create models of interferometers is a priority in the training of specialists, which contributes to the professional development of employees in this direction and activates their regulatory framework for the qualitative and promising development of these mechanisms. As noted by R. Apsari *et al.* [20], a multi-beam three-mirror interferometer allows the analysis of gas environments by analyzing the adsorbed from the gas to the hypotenuse surface of a monomolecular layer of matter. Each beam of light flux is reflected from the surface with a full internal reflection repeatedly. After analyzing this mechanism and its properties, it can be said that the multi-beam three-mirror interferometer can be used in optics in the creation of interference devices for various purposes for spectroscopy, as well as in the processing of optical information as sensors of various sensors and analyzers [21; 22].

It is necessary to increase funding for scientific processes of interferometer development and improve the quality of materials from which they are produced, to start introducing new technologies to improve the design and modeling of this mechanism.

Conclusions

Summarizing the results of this research, the following conclusions can be made. The main problems of the scientific process of developing two interferometers in every area, especially in optics, are insufficient funding, problems of proper modeling, design, and development of interferometers and their elements, failure to address the influence of many external factors in the design, these problems are and will be relevant and require further research. In this research, the goal was fulfilled, namely, the presentation of two interferometers designed following a new scheme and two ways to eliminate external influences in interferometers with two compensators, the analysis of the development process of two interferometers used in optics, as well as effective tools for eliminating external influences. It was possible to fulfill all the tasks of the research, namely, to highlight the problems of the operation of two interferometers and to analyze them more accurately, and methods for solving these issues were found and proposed for more efficient operation of this mechanism. The principle considered in the research is the development of models of two interferometers considering the influence of the external environment and possible assumptions, allows to obtain a comprehensive and more accurate assessment of the prospects of interferometers developed according to the new scheme, which is operated under different external influences.

The results of measurements made using the interferometer should be determined considering the specific operating conditions of this object. The presented schemes of interferometers in different variations can be used to optimize the development, a more accurate understanding of this mechanism will help in further simplifying the design and modeling. The analyzed modern approaches to the problems of Ukrainian development of interferometers will try to respond to the modern needs of users of these devices. Further research will be aimed at identifying problems and prospects for the development of new technologies for innovative compensators and beamsplitters, as well as expanding the range of applications of interferometers and increasing the capabilities of this mechanism.

Conflict of Interest

The author declares no conflict of interest.

Acknowledgements

None.

References

[1] Kolomiytsov YV. Interferometers: Fundamentals of engineering theory. Application. Engineering. leningrad: Mashinostroyeniye; 1976. 296 p.

[2] Chen Z, Zhang Y, Fan Y, Wang J, Lyu W, Zheng D, *et al*. Close observation of the evolution process during initial stage of triggered lightning based on continuous interferometer. *Remote Sens*. 2022;14(4):863. doi: 10.3390/RS14040863.

[3] Chen B, Jiang J, Lou Y, Yan L. Active linearized PGC demodulation with fusion of PGC-Arctan and PGC-DCM schemes for nonlinear error elimination in SPM interferometer. *Opt Express*. 2022;30(13):22999-23010. doi: 10.1364/OE.463593.

[4] Hu M, Yao C, Ventura A, Hayashi JG, Poletti F, Ren W. A comparative study of mid-infrared photothermal spectroscopy with different fiber interferometers. In: Optics and photonics for sensing the environment. Washington: Optica Publishing Group; 2022:3717-3721. doi: 10.1364/es.2022.etu4h.2.

[5] Zhang H, Wang B, Ning J, Li Y. Interferometry imaging using high-speed-train induced seismic waves. *Chin J Geophys*. 2019;62(6):2321-2327. doi: 10.6038/cjg2019M0676.

[6] Lendiel V, Stepakhno I, Yarovoi L. Application of three-wave heterodine interferometry for nanorized layers thickness measurement in the process of their deposition. *Bull Kyiv Polytech Inst Ser Instrum Mak*. 2022;63(1):39-45. doi: 10.20535/1970.63(1).2022.260636.

[7] Gryaznov NA, Goryachkin DA, Kuprenyuk VI, Sosnov EN, Alekseev VL. Passive stabilisation Michelson interferometer. *Sci Instrum*. 2020;30(4):67-74.

[8] Panov VV, inventor; Ukrainian Institute of Intellectual Property, assignee. Panov interferomete. Ukraine patent 149469. 2021 Feb 08. Available from: https://sis.nipo.gov.ua/uk/search/detail/1651693/.

[9] Panov VV, inventor; Ukrainian Institute of Intellectual Property, assignee. Interferometer. Ukraine patent 149105. 2021 Feb 12. Available from: https://sis.nipo.gov.ua/uk/search/detail/1632108/.

[10] Kabashin AV, Nikitin PI. Interferometer using surface plasmon resonance for sensor applications. *Quantum Electron*. 1997;24(7):671-672. doi: 10.1070/QE1997v027n07ABEH001013.

[11] Koronkevich VP, Lenkova GA. Laser interferometer for measuring length [Internet]. 1971 [cited 2022 Nov 30]. Available from: https://scholar.google.com.ua/scholar_host?q=info:8sp9_uci1Z8J:scholar.google.com/output=viewportpg=4hl=ukas_sdt=0,5.

[12] Ostapchuk AA. Research and calculation polarization properties of the interferometer using the method Jones. *J Zhytomyr State Technol Univ Eng*. 2015;2(73):154-158. doi: 10.26642/tn-2015-2(73)-154-158.

[13] Vrancken P, Herbst J. Aeronautics application of direct-detection Doppler wind lidar: an adapted design based on a fringe-imaging Michelson interferometer as spectral analyzer. *Remote Sens*. 2022;14(14):3356. doi: 10.3390/rs14143356.

[14] Thaisongkroh P, Pullteap S, Seat HC. Low-pressure measurement using an extrinsic fiber-based Fabry-Perot interferometer for industrial applications. *Eng J*. 2021;25(2):317-325. doi: 10.4186/ej.2021.25.2.317.

[15] McKinley B, Trott CM, Sokolowski M, Wayth RB, Sutinjo A, Patra N, *et al*. The All-Sky SignAl Short-Spacing INterferometer (ASSASSIN)-I. Global-sky measurements with the Engineering Development Array-2. *Mon Not R Astron Soc*. 2020;499(1):52-67. doi: 10.1093/mnras/staa2804.

[16] Pu Y, Cummer SA. Needles and lightning leader dynamics imaged with 100-200 MHz broadband VHF interferometry. *Geophys Res Lett*. 2019;46(22):13556-63. doi: 10.1029/2019GL085635.

[17] Adhikari RX, Arai K, Brooks AF, Wipf C, Aguiar O, Altin P, *et al*. A cryogenic silicon interferometer for gravitational-wave detection. *Class Quantum Gravity*. 2020;37(16):165003. doi: 10.1088/1361-6382/ab9143.

[18] Patel K, Nagora U, Joshi HC, Pathak S, Jadeja KA, Patel K, *et al*. LabVIEW-FPGA-based real-time data acquisition system for ADITYA-U heterodyne interferometry. *IEEE Trans Plasma Sci*. 2021;49(6):1891-1897. doi: 10.1109/TPS.2021.3082159.

[19] Kim W, Jung J, Kim J, Shin I, Kim N, Lee M. A new approach in optical metrology with multi-angle information through self-interferometric ellipsometry. In: Applied optical metrology IV. Washington: SPIE; 2021. p. 26-33. doi: 10.1117/12.2593375.

[20] Apsari R, Syadyyah H, Ningsih K, Yhuwana YGY. The development of the real-time Michelson interferometer for the measurement of thermal expansion coefficients of dental composites nanofiller. *J Phys: Conf Ser*. 2022;2274(1):012009. doi: 10.1088/1742-6596/2274/1/012009.

[21] Lopez B, Lagarde S, Petrov RG, Jaffe W, Antonelli P, Allouche F, *et al*. MATISSE, the VLTI mid-infrared imaging spectro-interferometer. Astron Astrophys. 2022;659:192. doi: 10.1051/0004-6361/202141785.

[22] Flores-Bravo JA, Illarramendi MA, Zubia J, Villatoro J. Optical fiber interferometer for temperature-independent refractive index measuring over a broad range. *Opt Laser Technol*. 2021;139:106977. doi: 10.1016/j.optlastec.2021.106977.

Науковий процес розробки двох інтерферометрів (оптичних) та пом’якшення зовнішнього впливу

Віталій Васильович Панов
Старший науковий співробітник
Дніпропетровське відділення Всесоюзного науково-дослідного гірничо-рятувального інституту
49000, пл. Героїв Майдану, м. Дніпро, Україна
https://orcid.org/0000-0002-2672-7748

Анотація

Актуальність. Актуальність дослідження зумовлена тим, що представлений об’єкт аналізу, а саме інтерферометр, відіграє важливу роль у сучасній науці в отриманні точних вимірювань та їх результатів, що ставить вимоги до вдосконалення інтерферометрів та усунення зовнішніх впливів.

Мета. Метою дослідження є аналіз процесу розвитку двох інтерферометрів, які використовуються в багатьох наукових сферах, особливо в оптиці, і відіграють важливу роль в отриманні точних результатів вимірювань при проведенні досліджень, а також пошук нових ефективних технологій для усунення зовнішніх впливів.

Методологія. Серед використаних методів – аналітичний метод, метод логічного аналізу, функціональний метод, статистичний метод, метод синтезу та інші.

Результати. В ході дослідження було розглянуто два компенсатори та відмінності між ними, а також проаналізовано особливості роботи цих компенсаторів та їх надійність. Виявлено негативні фактори, які перешкоджають більш точним вимірюванням за допомогою інтерферометра, а також визначено найбільш пошкоджені елементи в інтерферометрах та причини їх пошкодження. Аналіз функціонування інтерферометрів і компенсаторів та умов їх експлуатації є важливим для оцінки ступеня ефективності, актуальності та прогресу в оптиці. Також розглянуто питання оцінки розвитку та проблем двох схем інтерферометрів з трапецієподібним та квадратним променерозсіювачами та запропоновано рекомендації, які сприятимуть більш ефективному механізму регулювання цього питання.

Висновки. Визначено, що процес розробки інтерферометрів нового покоління та усунення зовнішніх впливів на них відіграє вирішальну роль у розвитку оптики, суттєво впливаючи на прогрес у цій галузі. Практична цінність полягає у застосуванні виявлених результатів, вирішенні проблем процесу розробки інтерферометрів та їх прогресу в експлуатації з урахуванням різноманітних зовнішніх впливів, що сприятиме зміні схеми підходу до розробки цього механізму та підвищенню стійкості до негативних зовнішніх впливів

Ключові слова: компенсатори; вимірювання; негативні фактори; схеми; введення променя

Scientific Herald of Uzhhorod University
Series “Physics”

Journal homepage: https://physics.uz.ua/en
Issue 53, 31-41
Received: 02/27/2023. Revised: 04/28/2023. Accepted: 05/30/2023

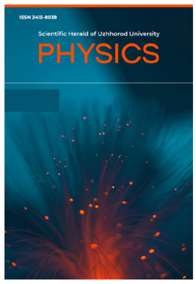

UDC 681.2.08: 621.311.25:621.039
PACS: 28.52.Fa, 28.52.Lf, 87.52.g
DOI: 10.54919/physics/53.2023.31

Cobalt application in repair tools for maintenance and modernisation of NPP equipment

Vitalii Levchenko

Metrology Engineer of the 1st Category, Head of the Mechanical and Geometric Measurements Group
Separate Subdivision “Zaporizhzhia NPP”
71500, 133 Promyslova Str., Energodar, Ukraine
https://orcid.org/0000-0002-0391-9907

Oleksii Pogosov*

Doctor of Technical Sciences, Professor
Odesa Polytechnic National University
65044, 1 Shevchenko Ave., Odesa, Ukraine
https://orcid.org/0000-0002-1942-2612

Volodymyr Kravchenko

Doctor of Technical Sciences, Professor
Odesa Polytechnic National University
65044, 1 Shevchenko Ave., Odesa, Ukraine
https://orcid.org/0000-0002-7557-3327

Abstract

Relevance. The research discusses the actual risks that can arise from the formation of the radioisotope cobalt ^{60}Co from the stable isotope ^{59}Co during radiation neutron capture, which is specific to repair work at a nuclear power plant, but these risks are poorly understood.

Aim. The research aims to analyse the possibility of additional exposure to ionising radiation for the repair personnel of a nuclear power plant due to the use of a repair tool that may contain cobalt.

Methodology. The physical-theoretical and analytical approaches are used in the study.

Results. A certain risk has been identified as a result of the use of drills or other tools for cutting metal containing cobalt among the repair tools. The calculation (analysis) of the activation of a cobalt-containing drill bit showed that a drill bit weighing 500 g containing 8% of ^{59}Co in the tool steel acquires a partial activity (i.e., only cobalt activity) of 5.397×10^{-8} Ci, which leads to gamma radiation with an exposure dose rate of 0.024 mSv/year. The

Suggested Citation:
Levchenko V, Pogosov O, Kravchenko V. Cobalt application in repair tools for maintenance and modernisation of NPP equipment. *Sci Herald Uzhhorod Univ Ser Phys.* 2023;(53):31-41. doi: 10.54919/physics/53.2023.31

*Corresponding author

calculations of dose rates did not consider gamma radiation from the nuclear isomeric transition $^{60m}Co \rightarrow ^{60}Co$, which could only worsen the radiation risk picture (when considering other examples).

Conclusions. The use of a drill bit with the cobalt content specified in the calculations (or the location of the drill bit in the vicinity of the personnel), one way or another, contributes to the personnel exposure. It is proved that the calculation was not conservative, but rather liberal, because gamma radiation from the ^{60m}Co isomer was not considered, otherwise, the obtained numerical values would have been higher. A practical recommendation to prohibit or reduce the use of tools containing cobalt during repairs on nuclear power plant equipment was made, theoretically, given that the analytically justified need to study the issue of radiation safety is relevant and vital for the-safety of NPP maintenance personnel

Keywords: radiation safety; ionising radiation; collective dose; exposure dose rate; gamma photons; drills; neutron energy

Introduction

When installing new equipment at a nuclear power plant (NPP), for example, installing new measuring instruments (including sensors) or additional process equipment (during modernisation), it is inevitable that a locksmith tool is required, and it is the choice of this tool that not everyone currently pays attention to.

At the same time, it is known that the bulk of the collective effective dose of ionising radiation is received by NPP personnel during scheduled and unscheduled outages. Therefore, radiation safety measures to reduce radiation doses should cover the organisation of work during scheduled outages (hereinafter referred to as SOC) (this applies to planning, preparation, execution and control) [1].

To this end, before the start of the outage, dose quotas for personnel involved in repair activities are established for each Ukrainian NPP unit [2; 3]. Preliminary forecasts of collective doses are developed based on the analysis of the radiation state of equipment of a particular nuclear reactor unit during previous outages, with future labour costs for outages to be considered.

Scientists and engineers in practical nuclear power plant operations around the world are finding cobalt in reactor room equipment and trying to reduce its impact on personnel. H. Ocken [4] discusses the feasibility of reducing the cobalt content in the metal of NPP equipment. This issue is also the subject of a joint study conducted by the Nuclear Energy Institute, Electric Power Research Institute and Nuclear Reactor Operations Institute (all US institutions), which resulted in recommendations and a strategy to reduce cobalt content in NPP equipment [5]. The team of authors of the Scientific and Technical Complex "Nuclear Fuel Cycle" of the National Science Centre of the Kharkiv Institute of Physics and Technology (KIPT) [6] proposes to use the Zn additive in the composition of the VVER-1000 primary coolant to reduce corrosion and delay diffusion of cobalt through the oxide film, reduce its release into the coolant medium, and thus reduce the level of radiation in the primary circuit and premises serviced during NPP operation, which demonstrates the urgency of the problem. Castiella Villacampa also considers the process of degradation of cobalt alloys in NPP equipment [7]. In its study, the Electric Power Research Institute (USA) also aimed to reduce radiation exposure to NPP personnel and identified cobalt in the first circuit equipment as one of the main sources of personnel exposure [8]. A team of Egyptian scientists generally suggests the use of cobalt-free steel [9]. However, it should be noted that almost all authors of publications in their studies do not pay attention to the issue of cobalt appearance due to the use of locksmith tools containing cobalt.

It should be noted that to date, there is no complete understanding of the processes of cobalt isotope ^{60}Co occurrence at the sites of repair work on the first circuit equipment, which is found among metal cutting waste since cobalt is not a component of alloys used in the flow part of the reactor equipment.

Based on the Law of Ukraine "On the Use of Nuclear Energy and Radiation Safety", radiation protection during the use of nuclear energy is based on the principle that the magnitude of individual doses, the number of people exposed and the probability of exposure to any type of ionising radiation should be the lowest that can be practically achieved, considering economic and social factors and based on the basic principle of state policy in the field of nuclear energy use and radiation protection: the priority of protection of people and the environment [10]. These two principles confirm the importance of this study.

In other words, a hypothesis was proposed that metal cutting tools with a significant cobalt content could lead to additional exposure of personnel during repair.

The research aims to investigate the possibility of additional (partial) risks of gamma photon exposure from the radioisotope ^{60}Co during repair at NPPs using metal cutting tools containing cobalt.

To achieve this goal, the following tasks were set and solved: analyse the ways of formation of the radioisotope ^{60}Co in the metal of the first circuit equipment; investigate the possibility of formation of the radioisotope ^{60}Co in metal cutting tools during repair work; quantify the possible additional radiation risk arising from repair work when using metal cutting tools containing cobalt.

Materials and Methods

The research object is a variety of metalworking tools (containing cobalt) used during scheduled maintenance of equipment in the reactor compartment of a nuclear power unit.

The study used publicly available data on the neutron-physical characteristics of the cobalt isotope ^{59}Co and public technical information on its content in some modern high-speed alloys.

To solve the tasks set and achieve the above goal, the physical and theoretical approach and analytical and computational methods of information processing were used.

The calculation was performed using the formulas listed below in the following order.

1. Concentration of cobalt atomic nuclei at the initial (zero) moment of ^{59}Co transformation into ^{60}Co according to the formula:

$$N_{59}^{\langle 0\rangle} = \frac{N_A}{A_{59}}, \quad (1)$$

where N_A – Avogadro number, $\frac{1}{\text{mol}}$; A_{59} – molar mass ^{59}Co, $\frac{g}{\text{mol}}$.

2. The number of cobalt nuclides in the cutting tool by the formula:

$$N_x = m \times N_{59}^{\langle 0\rangle}, \quad (2)$$

where m – bore mass, g.

3. The rate of formation of ^{60}Co in the tool is calculated by the formula:

$$I = N_x \times \sigma \times \Phi\,, \quad (3)$$

where σ – microscopic cross-section of activation of a stable cobalt isotope, barn; Φ – neutron flux density, which irradiates the contact element of the tool (drill bit), $\frac{neutr}{cm^2 \cdot s}$.

4. The number of cores formed during working hours according to the formula:

$$N_1 = t \times I\,, \quad (4)$$

where t – time during which the acquired activity of the cutting tool is exponentially reduced due to the decay of ^{60}Co accumulated during the contact of the tool with the equipment, s.

5. Activity of ^{60}Co at decay by the formula:

$$\mathrm{A} = \lambda_p \times N_1\,, \quad (5)$$

where λ_p – constant isotope decay ^{60}Co.

$$\lambda_p = \frac{\ln 2}{T_{1/2}}, \quad (6)$$

where $T_{1/2}$ – half-life, sec.

6. Exposure dose rate from gamma radiation by the formula:

$$P_\gamma = \frac{K_\gamma \times A}{R^2}, \quad (7)$$

where K_γ – ionisation gamma-ray constant. For ^{60}Co $K_\gamma = 2.5 \cdot 10^{-18} \frac{Cl \cdot m^2}{kg \cdot s \cdot Bq}$ or $12.9 \frac{\text{P} \cdot cm^2}{year \cdot mCi}$; A – activity, Ci; R – the distance of a person to the gamma-ray emitter source (worker – to the drill), (arm's length) is R=50 cm. Formal and logical methods of cognition, modelling methods, and methods of formal and logical interpretation of the content of scientific and regulatory categories and concepts were used to formulate conclusions. The potential risks of using locksmith tools at NPPs were identified using formal logistic methods and should be considered whenever it is possible to change the tools (negation and transition from quantity to quality – according to Hegel, general logistics). In this case, theoretically known variables were used, according to the above formulas, following professional knowledge in the field of nuclear energy.

Results and Discussion

At all stages of preparing and conducting the emergency response, dosimetric monitoring and radiation surveys are carried out on radiation-hazardous equipment following the recommendations[11].

Radiation exposure to maintenance personnel includes:

– radiation contamination;

– ionising radiation.

Radiation contamination can be both external and internal. It is the internal contamination of personnel that requires special attention, as it is the most dangerous for human health. When radioactive material enters the human body, it can be transferred to different areas (for example, to the bone marrow), where it continues to emit radiation. And even a small number of radionuclides inside the body exposes an employee to danger. One of these hazardous materials is the cobalt isotope ^{60}Co [12-14].

To further investigate the problem, it is necessary to assume that the radioisotope ^{60}Co is formed as a result of nuclear transformations in both the equipment of the first circuit and the metal cutting tool used in repairs at NPPs.

The contribution of radiation exposure of individual groups of the main equipment to the total collective dose received by personnel during NPP unit outages, for example, during outage 2020, on average at the State Enterprise "National Nuclear Energy Company (SE NNEGC) "Energoatom" was (approximately) 23% from the reactor unit, 6% from the main circulation pipeline, 4% from the main circulation pump, 17% from the steam generator, 1% from the pressure compensator, 11% from the cooling system, 6% from auxiliary systems of the reactor compartment, 4% from the SSC-1.2, and 2% from nuclear fuel (during overload) [15]. It is not difficult to calculate that the contribution of exposure from the main equipment during an outage is approximately 74%. The question arises as to what causes the remaining 26% of the collective dose.

The theoretical analysis, for the first time, unlike other scientific sources, confirmed that a component of radiation hazard is the risk associated with the radioactive cobalt isotope ^{60}Co, which can be formed by irradiation of the stable isotope ^{59}Co, which in turn occurs in the materials of the first circuit equipment as a result of nuclear transformations of iron and nickel, which are part of the 08(10)X18H10T steel:

– ^{58}Ni(n,p)^{58}Co; ^{58}Co(n,g)^{59}Co;
– ^{58}Fe(n,g)^{59}Fe, ^{59}Fe (β-decay $T_{1/2}$=47 days)→ ^{59}Co.

This explains the appearance of the stable isotope ^{59}Co in the first circuit.

Due to the erosive wear of metal in the flowing part of the first circuit equipment, the coolant carries cobalt through the equipment and leads to its accumulation on the surfaces.

Neutron activation of ^{59}Co leads to the formation of ^{60m}Co and ^{60}Co isomers: ^{59}Co(n,g)^{60m}Co→^{60}Co.

The physics and quantitative indicators of these nuclear transformations can be considered in detail. To date, two independent estimates are available: the estimates of the Smith and Desassières group (ENDF/B-VII) and the Watanabe estimate (JENDL-3.3). For example, Figure 1 shows the neutron-physical characteristics of radiative neutron capture by stable cobalt with its conversion into an unstable radioisotope [16; 17].

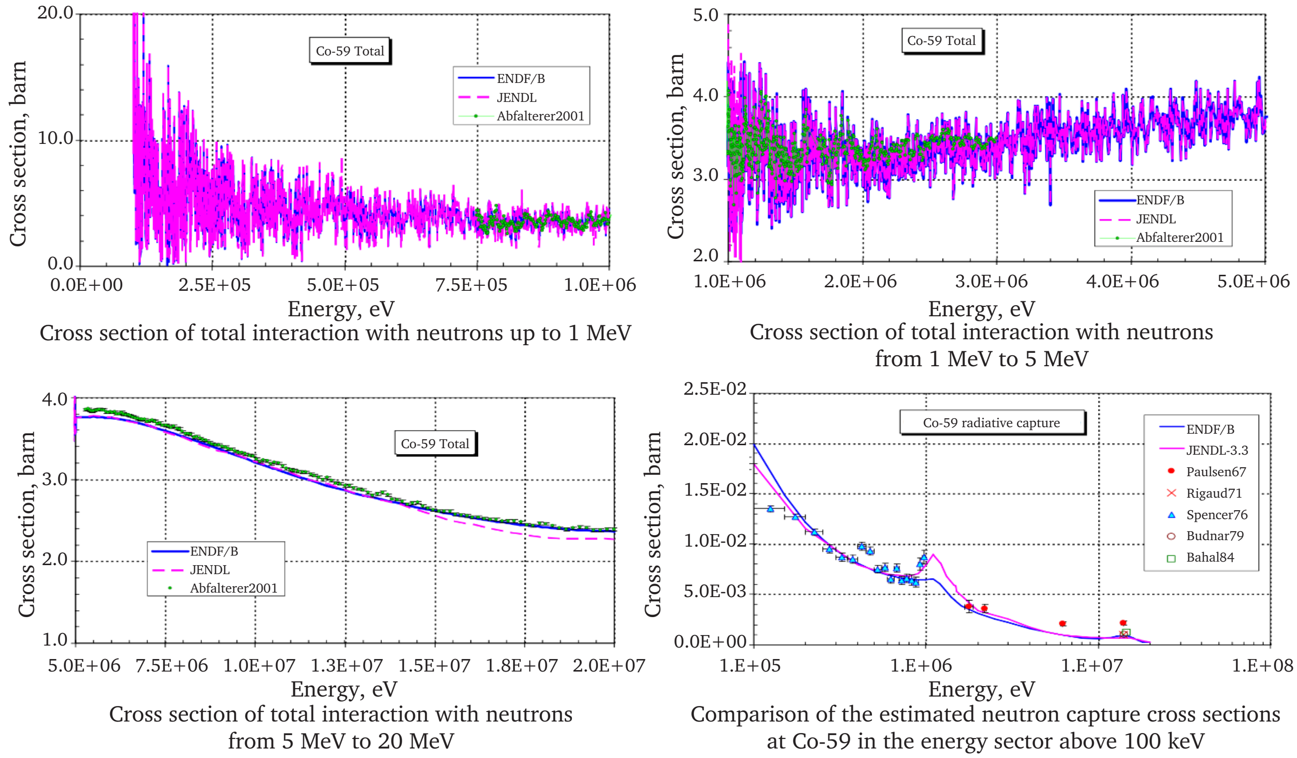

Cross section of total interaction with neutrons up to 1 MeV

Cross section of total interaction with neutrons from 1 MeV to 5 MeV

Cross section of total interaction with neutrons from 5 MeV to 20 MeV

Comparison of the estimated neutron capture cross sections at Co-59 in the energy sector above 100 keV

Figure 1. Neutron-physical characteristics of cobalt isotope ^{59}Co
Source: compiled by the authors based on [16; 17]

The neutron-physical characteristics indicate a significant microscopic cross-section of the activation reaction for low-energy neutrons [18].

The processes of activation of stable cobalt by neutrons occur both in the reactor (to a greater extent, due to the high fission neutron flux density) and in off-reactor equipment (to a lesser extent, due to the relatively low neutron flux density from radioactive contamination of the surfaces of the flowing part of the equipment). However, for fast and thermal (slow) neutrons, the reaction cross section is smaller than for thermal neutrons.

^{60}Co in the process of β-decay (half-life of 5.27 years) with transformation into ^{60}Ni is characterised by powerful non-monochromatic gamma radiation. Moreover, the ^{60}Co isomer is also a gamma emitter (its nuclear half-life is about 10 minutes).

These processes of ^{60}Co formation should be known in the practice of NPP operation, as they pose certain radiation risks, but no clear description of them could be found in the NPP literature. However, the study of the design and principle of operation of the so-called cobalt bomb [19] has led to what seems to be a more complete understanding of the formation of the ^{60}Co isotope. In other words, ^{60}Co in the first circuit, even after the reactor unit is shut down for a time-out, makes a significant contribution to the gamma background around the equipment being repaired. This is unavoidable, but radiation protection equipment for personnel performing repairs helps to reduce the collective dose.

At the same time, the study revealed that high-speed electromechanical tools are used to mechanise and accelerate repair operations with radioactive equipment at NPPs. The use of such tools is regulated, but the analysis did not reveal any prohibitions or restrictions on the use of replaceable (consumable) elements of high-speed tools (drills, mills, cutters, etc.) at NPPs.

The scientific and technical developments of new modifications of tool high-speed steels that have emerged in recent years strongly recommend increasing the cobalt content in steel, where it was not previously present in previous years' designs [20-22].

Modern developments in metal cutting tools indicate that the cutting ability of martensitic steels is proportional to their cobalt content [23; 24]. Modern industry has mastered the production of appropriate tools in an attempt to improve the mechanical characteristics of tool steels, but the change in the neutron-physical properties of these steels was not considered.

It is known that at the end of the 20th century, drills were produced from high-speed steels of grades (e.g., P9; P18) (the number after the letter "P" determined the percentage of tungsten), while the amount of cobalt in those alloys was very small [25]. Such drills, which were designed to work with materials at nuclear power plants according to the projects of that time (due to the neutron-physical properties of the tool alloy), are almost impossible to find on sale today. Table 1 shows the content of some modern high-speed alloys.

Table 1. The content of some modern high-speed alloys, %

Steel grade / Contents	P9	P18	10X12K4V2DMFBR	10X9V2MFBR (P92)	P0M1F3	P6M5	P6M5F2K8	P9K5
C	0.85-0.95	0.73-0.83	0.1	0.07-0.1	1.10-1.25	0.82-0.90	0.95-1.05	0.9-1.0
Si	-	-	≤0.05	0.3-0.6	-	-	-	<0.5
Mn	-	-	≤0.05	0.54	-	-	-	<0.5
Cr	3.8-4.4	3.8-4.4	11.9	8.5-9.5	3.8-4.6	3.8-4.6	3.8-4.4	3.8-4.4
Co	-	<0.5	4.0	-	-	<0.5	7.5-8.5	5.0-6.0
Mo	<1.0	<1.0	0.59	0.51	2.3-2.9	4.8-5.3	4.6-5.2	<1.0
W	8.5-10.0	17.0-18.5	2.2	1.5-2.5	-	5.5-6.5	5.5-6.6	9.0-10.0
V	2.0-2.6	1.0-1.4	0.22	0.15-0.23	2.6-3.3	1.7-2.1	1.8-2.4	2.3-2.7
Nb	-	-	0.05	0.03-0.07	-	-	-	-
B	-	-	0.012	0.001-0.006	-	-	-	-
N	-	-	0.012	0.04	-	-	-	-
Al	-	-	≤0.05	≤0.013	-	-	-	-
Ni	-	-	0.065	0.21	-	-	-	<0.4

Source: compiled by the authors based on [25]

The data in Table 1 show that Ukrainian nuclear power generation companies are currently actively offering metalworking tools that contain cobalt in much higher amounts than traditional tools made of steel (e.g., P9; P18), which were intended for use in NPP repairs according to the design. Here is just one example of the actual situation regarding the possible use of a tool with significant cobalt content that may come into contact with equipment during NPP repairs.

For example, Ukrnichrome LLC lists Energoatom among its customer-consumers [26]. The product catalogue of this supplier of nuclear power plants includes products made of P9K5 tool steel, which contains an increased proportion of cobalt [27]. Sometimes, the grade of tool steel is unspecific or unclear, for example, foreign manufacturers mark drills with the abbreviation HSS (High-Speed Steel) and only the added letter “E” indicates that the steel contains cobalt [28; 29] or other markings, such as M42 [30]. In Ukraine, the technical specifications for tool steels harmonised with the European Union are in force and should be used as a basis for choosing a steel grade for industry [31]. Figure 2, for example, shows an image of drills made of HSS and HSS-E tool steel grades.

Figure 2. The appearance of modern drill bits with cobalt content markings. The letter “E” indicates that the steel contains cobalt

Source: [28]

For further computational analysis, derived data on the cross-section of the ^{59}Co radiative neutron capture reaction obtained mathematically from the Japanese Atomic Energy Agency, namely the above-mentioned JENDL-3, were selected and are selectively presented in Table 2.

Table 2. Cross section of the (n,γ)-reaction of ^{59}Co interaction with low-energy neutrons

Neutron energy, eV	$1.0\cdot10^{-5}$	$1.31\cdot10^{-5}$	$1.71\cdot10^{-5}$	$2.24\cdot10^{-5}$	$2.92\cdot10^{-5}$
intersection (n,γ) absorption, barn	1872.53	1634.54	1432.48	1250.41	1095.84

Source: compiled by the authors based on [17]

These calculated data complement the officially accepted graphical dependences shown in Figure 1 and show that for neutrons, the values of the microscopic activation cross-section of the stable cobalt isotope are large. An increase in neutron energy determines a relatively rapid decrease in the microscopic cross-section of the reaction. This situation is reflected in the calculated (extrapolated) graphical dependence shown in Figure 3.

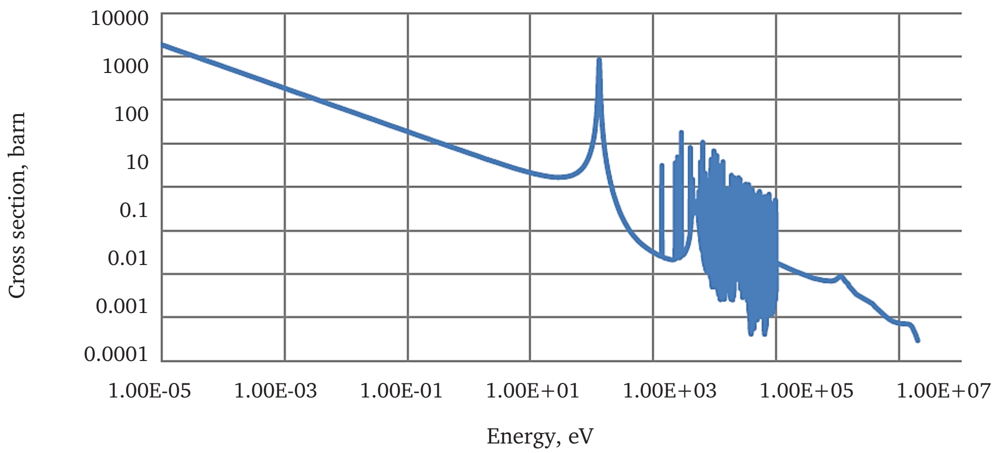

Figure 3. Dependence of the microscopic cross-section of neutron capture by isotope ^{59}Co from neutron energy

Source: compiled by the authors based on [17]

Thus, it can be considered appropriate to accept the value σ=1872 barn in further calculations. It should be noted that it would be desirable to accept the value based not on theoretical considerations but on field studies with empirical determination of the energy spectrum of neutrons coming from activated equipment under repair at NPPs.

The amount of stable isotope ^{59}Co nuclides in the volume of the drill bit element exposed to neutron irradiation with subsequent conversion to ^{60}Co was then determined. For this purpose, first, the mass of cobalt contained in a drill bit similar to those considered was approximately determined. We assume that the ^{59}Co content is 8%. If the mass of the drill is 500 g, then the mass of cobalt in such a drill is m=40 g.

The calculation was performed using formulas 1-7.

The concentration of cobalt atomic nuclei at the initial (zero) moment of ^{59}Co transformation into ^{60}Co is:

$$N_{59}^{\langle 0 \rangle} = \frac{6{,}022\times10^{23}}{58.993} = 1{,}021\times10^{22}\cdot 1/\text{gram}$$

Therefore, the cutting tool contains the following number of cobalt nuclides:

$$N_x = 40\times1{,}021\times10^{22} = 4{,}084\times10^{23}\cdot\text{nuclei}$$

Let us consider a hypothetical case of neutron irradiation of stable cobalt. In a shutdown reactor, the neutron flux density is estimated to be 10^{-9} of the nominal value. The average neutron flux density in the core is $5.8\times10^{13}\frac{neutr}{cm^2\cdot s}$ [32]. Therefore, for further calculations, $F=5.8\times10^{4}\frac{neutr}{cm^2\cdot s}$ is assumed. The refinement can be made by direct measurement. In this case, the rate of ^{60}Co formation in the tool will be:

$$\mathrm{I} = 4{,}084\times10^{23}\times1872\times10^{-24}\times5.8\cdot10^{4} = 4{,}434\times10^{7}\ \frac{nuclei}{s}$$

For example, we calculated the activity that will be acquired during the use of the drill for 3 hours of working time. Thus, if the irradiation time of the drill is 3 hours (10800 s), then multiplying by the rate of nucleation of ^{60}Co, we will get the number of nuclei formed during 3 hours of working time:

$$N_1 = 10800\times4{,}434\times10^{7} = 4{,}789\times10^{11}\ \text{nuclei}$$

This number of nuclei corresponds to the decay activity of ^{60}Co:

$$\lambda_{\mathrm{p}} = \frac{ln\,2}{1{,}663\times10^{8}} = 4{,}169\times10^{-9}\ \cdot c^{-1}$$

Thus, the activity of the drill, after substituting numerical values into formula (5):

$$A = 4{,}169\times10^{-9}\times4{,}789\times10^{11} = 1{,}997\times10^{3}Bq = 5{,}397\ \times10^{-8}\,Ci$$

The obtained numerical estimate is an approximate value of the activity, which characterises the amount of ^{60}Co isotope accumulated in the instrument during 3 hours of repairs using it.

Next, let's estimate the exposure dose rate from gamma radiation, considering the ionisation gamma constant of ^{60}Co, based on the definition of the gamma constant and its physical meaning:

$$P_\gamma = 12.9\times\frac{1000\times5{,}397\times10^{-8}}{50^2} = 2{,}785\times10^{-7}\ \frac{\mathrm{P}}{year} = 0.024\frac{mSv}{year}$$

The calculation of the activation of a cobalt-containing drill bit showed that a 500 g drill bit containing 8% ^{59}Co in the tool steel acquires partial activity (i.e., only cobalt activity) Ci, which leads to gamma radiation with an exposure dose rate of 0.024 mSv/year (with a limit of 20 mSv/year for category A personnel, according to NRBU-97/2000 [33]).

Receiving this dose may not seem significant but using a drill with the cobalt content specified in the calculations (or having the drill near personnel) also contributes to personnel exposure.

The calculation was not conservative; gamma radiation from the ^{60m}Co isomer was not considered, otherwise the values obtained would have been higher.

Nevertheless, the results obtained, although they should be considered approximate and preliminary, indicate the existence of a real (greater or lesser) risk due to the use of cobalt-containing drills among the tools. The results obtained can only be clarified by conducting full-scale experimental studies on NPP equipment. However, it is already possible to express concern and provide recommendations regarding the NPP repair work regulations – it is necessary to prohibit the use of drills, cutters, mills, etc. with cobalt in the steel in the tooling.

The issue of additional cobalt formation in NPP equipment is currently poorly understood, so the authors cannot rely on facts and studies on this problematic issue, but the assumption was made by NPP engineers during an oral discussion at the seminar of the NPP Department, National University "Odesa Polytechnic": that cobalt, which is a gamma-ray emitter and is present in cutting sawdust during repairs, is formed in the steel materials of circuit 1 equipment.

The emitter described in this study is formed as a result of neutron activation of iron (as well as cobalt and nickel) in steel structures.

Ukrainian physicist, expert in the field of radiation physics and nuclear safety, Doctor of Physical and Mathematical Sciences, Corresponding Member of the National Academy of Sciences of Ukraine V.M. Voevodin paid much attention to the study of radiation damage to structural materials in his studies [34; 35].

Analysing the studies of R. Rumbu and F. Crundwell, the results obtained in the study are consistent [36; 37]. The study [36] states that Cobalt is a hard, ductile, shiny bluish-grey metal, that belongs to heavy metals. Cobalt is an element of the side subgroup of the eighth group of the fourth period of the periodic table of chemical elements of D.I. Mendeleev, atomic number 27. It is denoted by the symbol Co (Latin cobalt). The name of the chemical element cobalt comes from it. Kobold means a housekeeper, a gnome. The burning of cobalt minerals containing arsenic releases volatile, poisonous arsenic oxide. The ore containing these minerals was named Kobold by miners as the mountain spirit. In 1735, Swedish mineralogist Georg Brand managed to isolate a previously unknown metal from this mineral, which he named cobalt. Cobalt has only one stable isotope, Co-59.

The study [37] proved that the "stellite" alloy, which is now used as a traditional metalworking tool alloy containing 35% cobalt, the same amount of chromium, 15% tungsten, 13% iron and 2% carbon, which has a high hardness, is used to make cutter tips, drills, bits, etc. Superhard alloys ("pobedit", etc.) containing 78% to 88% tungsten, 5% to 6% carbon and 6% to 15% cobalt, which is cobalt-cemented tungsten carbide, which retains its hardness even at temperatures up to 1000°C.

A study [35] shows that cobalt alloys were developed in the early 1990s by Elwood Haynes in the United States in search of a material that was resistant to aggressive environments and had sufficient strength and hardness at high temperatures. The study also found that alloying P911 steel with cobalt significantly increases creep resistance. The time to fracture increases by 4 times at a test temperature of 650°C and applied stresses from 100 MPa to 200 MPa.

At the same time, the analyses presented in the study revealed that there are certain risks relevant to NPP maintenance activities when using tools containing cobalt. Further discussion of the published materials in the article will be useful for understanding the technological processes and physics of material behaviour to improve the safety of repair work at Ukrainian NPPs.

Conclusions

Based on the analysis and numerical results obtained, the possibility of additional (partial) risks of gamma photon exposure from the radioisotope ^{60}Co during repair work at NPPs was confirmed. The hypothesis put forward at the beginning of the study was confirmed analytically.

It is necessary to consider that, firstly, there is a likely risk associated with the radioactive cobalt isotope ^{60}Co, the formation of which is associated with the activation of materials of primary circuit equipment, and decay is associated with the formation of powerful cascade non-monochromatic gamma radiation from process equipment, in the steel of which this isotope can be formed. Secondly, in addition to primary circuit equipment, this isotope may be formed in metal cutting tools that may come into contact with activated primary circuit equipment during repairs of NPP equipment. Such tools include drills, cutters, milling cutters, etc., which may contain cobalt ^{59}Co, which, when activated in the process of contact with the equipment, is converted into radioactive ^{60}Co.

Based on the results of the study, recommendations can be made to ban the use of drills, cutters, milling cutters, etc. with cobalt in the steel alloy during repairs on the equipment of the first circuit NPP. At the very least, this should be understood as a wake-up call to the scientific community.

The obtained scientific results are the first step of the research and can be clarified and supplemented by the scientific community through further experimental studies.

Conflict of Interest

The authors declare no conflict of interest.

Acknowledgement

None.

References

[1] Nefedov O, Tonkikh V, Urbansky V, Usacheva E. Analysis of repair documentation at NPPs of Ukraine. *Nucl Radiat Saf*. 2008;11(4):41-5.

[2] Pogosov OY, Sliusenko MY. About some problems of metrology in dosimetry and radiology. *Nucl Radiat Saf*. 2002;5(2):76-80.

[3] Pogosov OYu, Derevianko O. Physics of ionizing radiation and dosimetric control. Odesa: Science and technology; 2017. 128 p.

[4] Ocken H. Cobalt reduction in nuclear plants. *EPRI J.* 1991;16(6):5420314.

[5] Electric Power Research Institute. Cobalt reduction sourcebook. Technical Report. [Internet]. 2010. Available from: https://www.epri.com/research/products/1021103.

[6] Krasnorutskyy VS, Petelguzov IA, Grytsyna VM, Zuyok VA, Tretyakov MV, Rud RO, *et al*. Influence on corrosion of stainless steels and zirconium alloys of zinc injection into primary coolant of WWER-1000 reactors. *J. Probl. At. Sci. Technol.* 2014;2(90):53-61.

[7] Empresarios Agrupados [Internet]. Available from: https://www.empresariosagrupados.es/en/home/management-team/.

[8] Electric Power Research Institute. BWR source term reduction – estimating cobalt transport to the reactor. Technical Report [Internet]. 2008 [cited 2022 Dec. 24]. Available from: https://www.epri.com/research/products/000000000001018371.

[9] Mourad MM, Saudi HA, Eissa MM, Hassaan MY, Abdel-Latif MA. Mechanical properties and durability of cobalt free steel alloy as a developed radioactive waste capsule. *Appl Radiat Isot.* 2023;191:37-43. doi: 10.1016/j.apradiso.2023.110724.
[10] Verkhovna Rada of Ukraine. Law of Ukraine "On Use of Nuclear Power and Radiation Safety" (Fabruary 8, 1995) [Internet]. Available from: https://zakon.rada.gov.ua/rada/show/39/95-%D0%B2%D1%80?lang=en#Text. No. 39/95-BP.
[11] Methodological recommendations for the analysis of collective doses of exposure to personnel during repair work and maintenance of nuclear power plant equipment. Kyiv: SE "NNEGC "Energoatom"; 2007. 37 p.
[12] Bushberg JT. Radiation exposure and contamination [Internet]. 2022 November [cited 2022 December 14]. Available from: https://www.msdmanuals.com/professional/injuries-poisoning/radiation-exposure-and-contamination/radiation-exposure-and-contamination#v50219094.
[13] Adam C, Garnier-Laplace J, Roussel-Debet S. Cobalt-60 and the environment. Radionuclide fact sheet. Lyon: Institut de Radioprotection et de Sûreté Nucléaire (IRSN); 2010. 22 p.
[14] Arustamian OM, Tkachyshin VS, Arustamian YuA, Aleksiichuk OYu, Dumka IV. Features of cobalt and its compounds intoxication. *Bogomol Nat Med Univ.* 2022;18(1):6-11.
[15] Analytical annual report on the state of radiation safety and radiation protection at the NPP of SE "NAEK "Energoatom" in 2020. Kyiv: SE "NNEGC "Energoatom"; 2021. p 59.
[16] Chadwick MB, Oblozinsky P, Herman M, Greene NM, McKnight RD, Smith DL, *et al*. ENDF/B-VII.0: Next generation evaluated nuclear data library for nuclear science and technology. *Nucl Data Sheets.* 2006;107(12):2931-3060. doi: 10.1016/j.nds.2006.11.001.
[17] Japan Atomic Energy Agency. The JENDL-3.3 fission-product yield data library [Internet]. 2018 [cited 2022 Dec. 21]. Available from: https://wwwndc.jaea.go.jp/jendl/j33/j33.html.
[18] Brown DA, Chadwick MB, Capote R, Kahler AC, Trkov A, Herman MW. ENDF/B-VIII.0: The 8th major release of the nuclear reaction data library with CIELO-project cross sections, new standards and thermal scattering data. *Nucl Data Sheets.* 2018;148:1-142. doi: 10.1016/j.nds.2018.02.001.
[19] Pogosov OYu, Dubkovsky VA. Ionization radiation. Radioecology, physics, technology, protection. Odesa: Science and technology; 2012. 808 p.
[20] Gogaev KO. Tool steels. Encyclopedia of Modern Ukraine. [Internet]. Kyiv: Institute of Encyclopedic Research of the National Academy of Sciences of Ukraine; 2011 [cited 2022 December 21]. Available from: https://esu.com.ua/article-12375.
[21] Michalcová A, Pečinka V, Kačenka Z, Šerák J, Kubásek J, Novák P, *et al*. Microstructure, mechanical properties, and thermal stability of carbon-free high speed tool steel strengthened by intermetallics compared to vanadis 60 steel strengthened by carbides. *Met.* 2021;11(12):1901. doi: 10.3390/met11121901.
[22] Hillier EMK, Robinson MJ. Hydrogen embrittlement of high strength steel electroplated with zinc-cobalt alloys. *Corros Sci.* 2004;46(3):715-727. doi: 10.1016/S0010-938X(03)00180-X.
[23] William D, Callister JR. Materials science and engineering. Hoboken: Wiley; 2018. 975 p.
[24] Dobrzański LA, Kasprzak W. The influence of 5% cobalt addition on structure and working properties of the 9-2-2-5, 11-2-2-5 and 11-0-2-5 high-speed steels. *J Mater Process Technol*. 2001;109(1-2):52-64. doi: 10.1016/S0924-0136(00)00775-5.
[25] Standards Interstate. Bars and strips made of high-speed steel. Specifications. [Internet]. 1997 [cited 2022 Dec. 21]. Available from: https://dnaop.com/html/74144/doc-%D0%93%D0%9E%D0%A1%D0%A2_19265-73.
[26] Official website Ukrnihrom [Internet]. 2020 [cited 2022 Dec. 21]. Available from: http://ukrnichrom.com.ua/o-kompanii/nashi-klienty.
[27] Kutsova VZ, Kovzel MA, Nosko OA. Alloy steels and alloys with special properties. Dnipro: NMetAU; 2008. 348 p.
[28] GSR Gustav Stursberg GmbH. [Internet]. 2022 [cited 2022 December 14]. Available from: https://threadingtoolsguide.com/en/blog/hss-vs-hsse-is-hss-e-better-than-hss.
[29] Guhring Ltd. HSS-E material taps [Internet]. 2022 [cited 2022 Dec. 14]. Available from: https://www.guhring.com/BrowseProducts/Products/hss-e-material-taps.
[30] A Griggs Steel Company. M42 High Speed Steel [Internet]. 2022 [cited 2022 Dec. 14]. Available from: https://www.griggssteel.com/high-speed-steel/m42-steel.
[31] Standards Ukraine. Tool steels. Technical specifications. DSTU EN ISO 4957:2007 (EN ISO 4957:1999, IDT) [Internet]. 2007 [cited 2022 Dec. 21];. Available from: https://dnaop.com/html/61635_13.html.
[32] Verkhivker HP, Kravchenko VP. Fundamentals of calculation and design of nuclear power reactors. Odesa: TES; 2009. 409 p.

[33] Standards Ukraine. Radiation safety standards of Ukraine; supplement: Radiation protection from sources of potential exposure НРБУ-97/Д-2000 [Internet]. 2000 [cited 2022 Dec. 21]. Available from: https://zakon.rada.gov.ua/rada/show/v0116488-00#text.
[34] Neklyudov IM, Voyevodin VN, Laptev IN, Parkhomenko OO. Influence of an irradiation on elastic modules of metal materials. *Probl At Sci Technol, Ser: Plasma Phys.* 2014;2(90):21-28.
[35] Neklyudov IM, Borodin OV, Bryk VV, Voyevodin VN. Problem of radiation resistance of structural materials of nuclear power. In: Begun V, Jenkovszky LL, Polański A, editors. Progress in High-Energy physics and nuclear safety. Dordrecht: Springer; 2009. p. 259-77. doi: 10.1007/978-90-481-2287-5_25.
[36] Rumbu R. Extractive metallurgy of cobalt. Berlin: 2RA; 2018. 228 p.
[37] Crundwell F, Moats M, Ramachandran V, Robinson T, Davenport WG. Extractive metallurgy of nickel, cobalt and platinum group metals. Amsterdam: Elsevier; 2011. 622 p.

Використання кобальту в ремонтному інструменті при забезпеченні роботи та модернізації обладнання АЕС

Віталій Вікторович Левченко

Інженер з метрології 1 кат., керівник групи механічних та геометричних вимірювань
Відокремлений підрозділ «Запорізька атомна електрична станція»
71500, вул. Промислова, 133, м. Енергодар, Україна
https://orcid.org/0000-0002-0391-9907

Олексій Юрійович Погосов

Доктор технічних наук, професор
Національний університет «Одеська політехніка»
65044, пр. Шевченка, 1, м. Одеса, Україна
https://orcid.org/0000-0002-1942-2612

Володимир Петрович Кравченко

Доктор технічних наук, професор
Національний університет «Одеська політехніка»
65044, пр. Шевченка, 1, м. Одеса, Україна
https://orcid.org/0000-0002-7557-3327

Анотація

Актуальність. У статті розглянуті актуальні ризики, що ймовірно виникають внаслідок утворення радіоізотопу кобальт ^{60}Co із стабільного ізотопу ^{59}Co при радіаційному захоплені нейтронів, що є специфічним під час ремонтних робіт на атомній електростанції, проте ці ризики є мало вивченими.

Мета. Метою проведеного дослідження був аналіз можливості додаткового впливу іонізуючої радіації на ремонтний персонал атомної електричної станції, внаслідок використання слюсарного інструменту, який в своєму складі ремонтного інструментарію, може містити інструментальний кобальт.

Методологія. У статті використаний фізико-теоретичний та аналітичний підхід для проведення дослідження з'ясованої проблеми.

Результати. Визначено наявність певного ризику внаслідок використання серед ремонтного інструментарію свердл чи іншого інструменту для різання металу із вмістом кобальту. Проведений розрахунок (аналіз) щодо активації свердла зі вмістом кобальту показав, що свердло масою 500 г, яке містить в інструментальній сталі ^{59}Co в кількості 8 % по масі, набуває парціальну активність (тобто лише активність кобальту) $5{,}397\times10^{-8}$ Ки, що призводить до гама-випромінювання, потужність експозиційної дози якого досягає 0,024 мЗв/рік. В проведених розрахунках дозових показників не враховувалося гама-випромінювання

при ядерному ізомерному переході $^{60m}Co \rightarrow ^{60}Co$, що могло б тільки погіршити картину радіаційного ризику (при розгляді інших прикладів).

Висновки. Було зазначено, що використання свердла зі зазначеним (в розрахунках) вмістом кобальту (чи знаходження свердла неподалік від персоналу), так чи інше, робить додатковий внесок в опромінення персоналу. Доведено, що проведений розрахунок був не консервативним, а скоріше ліберальним, бо гама-випромінювання від ізомеру ^{60m}Co не враховувалася, інакше отриманні числові значення розрахунків були б більшими. Була надана практична рекомендація щодо заборони чи зменшення використання при проведені ремонтних робіт на обладнанні атомної електростанції інструментів, у складі яких міститься кобальт, теоретично зважаючи на те, що аналітично обґрунтована необхідність вивчення питання радіаційної безпеки є актуальною і життєвоважливою для безпеки-ремонтного персоналу АЕС

Ключові слова: радіаційна безпека; іонізаційне випромінювання; колективна доза опромінення; потужність експозиційної дози; гама-фотони; свердла; енергія нейтронів

Scientific Herald of Uzhhorod University
Series "Physics"
Journal homepage: https://physics.uz.ua/en
Issue 53, 42-52
Received: 02/17/2023. Revised: 05/07/2023. Accepted: 05/19/2023

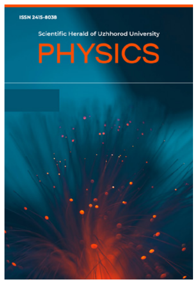

539.1.539.6
PACS: 88.20.fn.82.30.Rs
DOI: 10.54919/physics/53.2023.42

Diffusion flames and a semi-empirical method for estimating the distribution of hydrogen molecules in propane flames

Garnik Sargsyan*
PhD in Physical and Mathematical Sciences, Senior Researcher
A.B. Nalbandyan Institute of Chemical Physics of the National Academy of Sciences of the Republic of Armenia
0014, 5/2 Paruyr Sevak Str., Yerevan, Republic of Armenia
https://orcid.org/0000-0002-4832-0623

Petros Gukasyan
Doctor of Chemistry, Senior Researcher
ECOATOM LLC
0082, 1 Adana Str., Yerevan, Republic of Armenia
https://orcid.org/0009-0003-5569-0360

Hrachya Sargsyan
PhD in Physical and Mathematical Sciences, Senior Researcher
A.B. Nalbandyan Institute of Chemical Physics of the National Academy of Sciences of the Republic of Armenia
0014, 5/2 Paruyr Sevak Str., Yerevan, Republic of Armenia
https://orcid.org/0009-0006-4188-158X

Ruslan Poveda
PhD in Physical and Mathematical Sciences, Assistant Professor
Kamianets-Podilskyi Ivan Ohiienko National University
32300, 61 Ohiienko Str., Kamianets-Podilskyi, Ukraine
https://orcid.org/0000-0002-0067-6153

Abstract

Relevance. The greatest effectiveness in determining the main characteristics in gas burning was shown by optical methods due to their high speed and accuracy. Despite all the advantages of these methods, their main disadvantage is the price and folding of implementation. Therefore, today it is necessary to improve approaches to solve this problem.

Suggested Citation:
Sargsyan G, Gukasyan P, Sargsyan H, Poveda R. Diffusion flames and a semi-empirical method for estimating the distribution of hydrogen molecules in propane flames. *Sci Herald Uzhhorod Univ Ser Phys.* 2023;(53):42-52. doi: 10.54919/physics/53.2023.42

*Corresponding author

Purpose. The research is devoted to the study of diffusion flame by a semi-empirical method.

Methods. The data of the experimental study of the diffusion flame of hydrocarbons on the example of propane are presented. To visualize the invisible part of the structure of this flame, namely, the afterburning zone of hydrogen molecules formed in the flames in nonequilibrium quantities and, due to the large value of the diffusion coefficient, leaving the flame zone and creating a new combustion zone, molecules containing atoms of alkali metals (NaCl and Na_2CO_3) are vaporized in the flame zone.

Results. The method of delivery of molecules of alkali metal salts from outside was applied for the first time, which allowed the investigation of this phenomenon more thoroughly. Based on the research results, a method for determining the concentration of hydrogen atoms and the relative distribution of the concentration of hydrogen molecules along the axis of propagation of the flame after the burning zone was proposed. The research method combines experiments with mathematical modeling. The application of the method described in the article makes it possible to determine the distribution of hydrogen molecules over the glow zone of the main fuel.

Conclusions. The results obtained will help to better understand the phenomena of hydrocarbon combustion under diffusion flame conditions, as well as to search for new ways of obtaining hydrogen fuel from domestic waste treatment

Keywords: atom; fuel; sensors; physical effects; gas

Introduction

The rapid growth of the industry in the modern world and the climate changes caused by it make the tasks of controlling the concentration of harmful gases in production and at home topical. It is also important to determine the parameters of gases in various industrial processes [1-3]. In practice, when it is necessary to determine the concentrations of certain gases, it is necessary to choose the method which best meets the requirements and can solve the task. Optical methods showed the greatest efficiency in determining the main characteristics of the combustion of gases because of their high speed and accuracy. Despite all the advantages of these methods, their main disadvantage is the price and folding of implementation [4-6]. Therefore, today it is necessary to improve approaches to solve this issue. It is known that in diffusion flames of organic compounds in the gas phase hydrocarbon fuels form a nonequilibrium large concentration of intermediate H_2 products, which create a second (invisible) flame zone in the neighborhood of the luminous flame zone.

Theoretical simulations of hydrocarbon combustion under diffusion flame conditions show that the flame has a complex structure; it consists of clearly defined zones that differ from each other in character [7; 8]. Namely, the zone of contact and mutual diffusion of the combustible and oxidizer can be divided into a zone of combustible flow, followed by a new zone of radical formation [9]. In the same work, the profiles of concentrations of radicals and H_2, CO, H_2O, and O_2 were obtained in the case when the stoichiometric ratio between methane and oxygen is achieved. The afterburning zone of H_2 and CO after the complete consumption of methane is visible. The data of Zh. Wang *et al*. [10] also show that the structure of the diffusion methane flame includes a thin zone of reaction of CH_4 with OH, H, and O and a fairly wide zone of weak combustion of H_2 and CO. To explain the asymptotic structure of the methane flame in [11-13], it can be found an example of a discussion of the three-stage mechanism commonly used to explain the reaction process in the steady state approximation and partial equilibrium for intermediate products. For the oxidation of methane (1):

$$\begin{array}{c} 1.\, CH_4 + O_2 \rightarrow CO + H_2 + H_2O \\ 2.\, CO + H_2O \rightarrow CO_2 + H_2 \\ 3a.\, O_2 + 2H_2 \rightarrow 2H_2O \\ 3b.\, O_2 + 3H_2 \rightarrow 2H + 2H_2O \end{array} . \tag{1}$$

In dimensionless coordinates, the flame structure is calculated, and several zones are highlighted, namely, a thin zone of methane flow and a fairly wide zone of weak hydrogen flame, the length of which is determined by the reaction $H+O_2+M \rightarrow HO_2+M$ from the list of reactions (2):

$$\begin{array}{c} 1.\, H + O_2 + M \rightarrow HO_2 + M \\ 2.\, H + HO_2 \rightarrow H_2 + O_2 \\ 3.\, HO_2 + HO_2 \rightarrow H_2O_2 \\ 4.\, H_2O_2 + H \rightarrow H_2 + HO_2 \end{array} . \tag{2}$$

In the work of A. Hamins and K. Seshadri [14] determined the dependence of concentrations of H_2, CO, methanol, and heptane on the distance behind the luminous flame zone under countercurrent conditions. For hydrogen molecules in all experimental cases, the width of the zone of their penetration in the direction of oxygen due to diffusion is about 1-2 millimeters. It is reasonable to describe the contribution of the diffusive transfer of constituents in a complex four-component system within the framework of the nonlinear multicomponent diffusion formalism developed by the authors of the following works [15-17]. Due to the experimental difficulties of forming and maintaining diffusion flames for a long time, the use of visual (photographic) methods in their study is very effective for establishing the concentration distribution of intermediate products in this flare [18]. Methods of photographic imaging capture an instantaneous picture of a continuously fluctuating process and make it possible to determine the concentration distribution of the flame participants. It is also possible to continuously monitor the progression of the process [19].

It is known that NaCl vapor in a mixture of combustible gases, such as H_2, hydrocarbons, and various organic compounds, causes flame coloring caused by excited sodium atoms [1]. To explain the mechanism of the formation of excited sodium atoms, the authors of many studies propose different mechanisms [20; 21]. Since sodium atoms have low electronic levels, only a portion of the recombination heat released by the reaction is sufficient to excite them, and the presence of low-lying ionic terms increases the probability of energy transfer between them. Several are known to explain the coloring of hydrogen-burning flames by the addition of sodium atoms and the addition of sodium to the stream of hydrogen atoms coming out of the electric discharge tube [20-22]. Two elementary acts leading to the manifestation of excited sodium atoms are considered:

$$H + OH + Na \rightarrow H_2O + Na\ (2P), \qquad (3)$$

$$H + H + Na \rightarrow H_2 + Na\ (2P). \qquad (4)$$

Kinetic analysis of the results for reactions (3) and (4) showed satisfactory agreement with experimental data and the rate constants of these reactions 2·1010 and 8·109 l^2/mol^2s, respectively, were obtained [21]. At present, the absorption spectroscopy method based on the phenomenon of selective absorption of radiation by gases is widely used [23; 24]. Selective absorption can be achieved if the radiation frequency is resonant for the molecules of a given gas.

The phenomenon of flame coloration is mainly used to determine the flame temperature, and therefore, in all works, salt molecules, as usual, were fed into the flame together with the flow of oxidizer or combustible gas [1]. But until now, due to the complexity of calculation, the distribution of the concentration of intermediate products depending on the flow rate cannot be obtained accurately. In this paper, authors propose a method for determining the concentration of atoms and the concentration distribution of hydrogen molecules behind the glow zone of the main combustible by feeding sodium-containing salt vapor into the flame from the outside.

The main goal of the study was to conduct an experiment that would confirm the effectiveness of using the semi-empirical method in the study of diffuse flames.

Materials and Methods

The diffusion flame of propane (used in domestic conditions) is obtained by feeding the combustible through a capillary 1 cm long and 0.5 mm in diameter into the atmosphere. To study the invisible combustion zone of hydrogen formed in nonequilibrium quantities during the combustion of hydrocarbons, in this work authors use molecules of NaCl and drinking soda $NaHCO_3$ (transformed into Na_2HCO_3 by the reaction $2NaHCO_3 \rightarrow Na_2CO_3 + CO_2 + H_2O$). The method of delivery of the molecules of these substances to the flame was carried out as follows. A schematic of the experimental setup is shown in Figure 1.

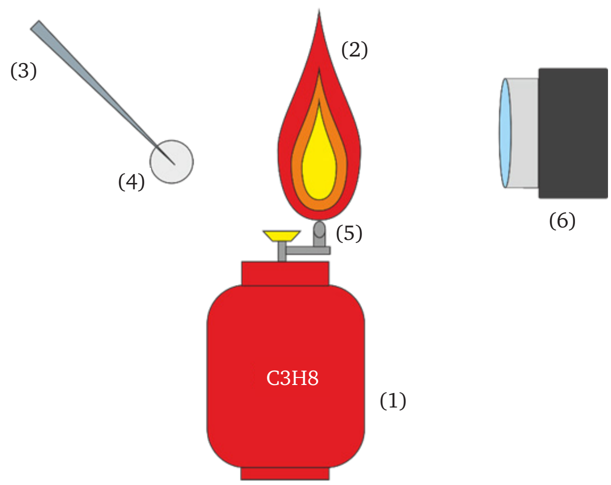

Figure 1. Schematic of the experimental setup
Note: 1 – propane cylinder; 2 – propane diffusion flame; 3 – steel needle; 4 – sodium salt crystals; 5 – fuel capillary; 6 – photo camera
Source: [24]

The edge of the steel needle was pre-wet with water, after which NaCl or $NaHCO_3$ crystals were collected on it. Then this part of the needle was preheated until a liquid drop of these substances appeared on it. After cooling, a plate or a ball of the above-mentioned substances was formed at the end of the needle. Before the probing process, this part of the needle was preheated to intensify the evaporation rate.

The needle was then fixed at different distances from the propane flame. The NaCl or $NaHCO_3$ molecules from the surface of the steel needle evaporated into the combustion zone. Due to the recombination of H and OH radicals on sodium atoms, which are the products of the reaction of NaCl and $NaHCO_3$ with the flame H_2, $CO+O_2$, which sodium atoms are formed in electronically excited states, carrying away with their part of the recombination energy. Some of these molecules are stabilized by collisions with atmospheric gas, while others emit light quanta in the wavelength range λ=5889-5899 A. In this case, a luminous zone is formed around the hydrocarbon flame, making it possible to visually observe the magnitude of hydrogen combustion.

Results

The diffusion propane flame was photographed using a digital camera. The results are shown in Figures 2. At the bottom of the figures, the conditions of the experiment are shown. In Figure 2a, the case of NaCl molecules evaporating over the luminescent flame zone of propane. There is an image of a fragment of the hydrogen afterburning zone as a yellow luminescent zone. Figure 2b gives an image of the propane flame in the case where the salt molecules evaporate into the flame from the side, outside the luminescent zone. A legible image is drawn of the invisible part of the flame structure as a second flame surrounding the luminous zone. It can be seen that the width of the hydrogen afterburning zone is about 2 millimeters on the side. At the top of the flame, the hydrogen afterburning zone extends to about 6 millimeters.

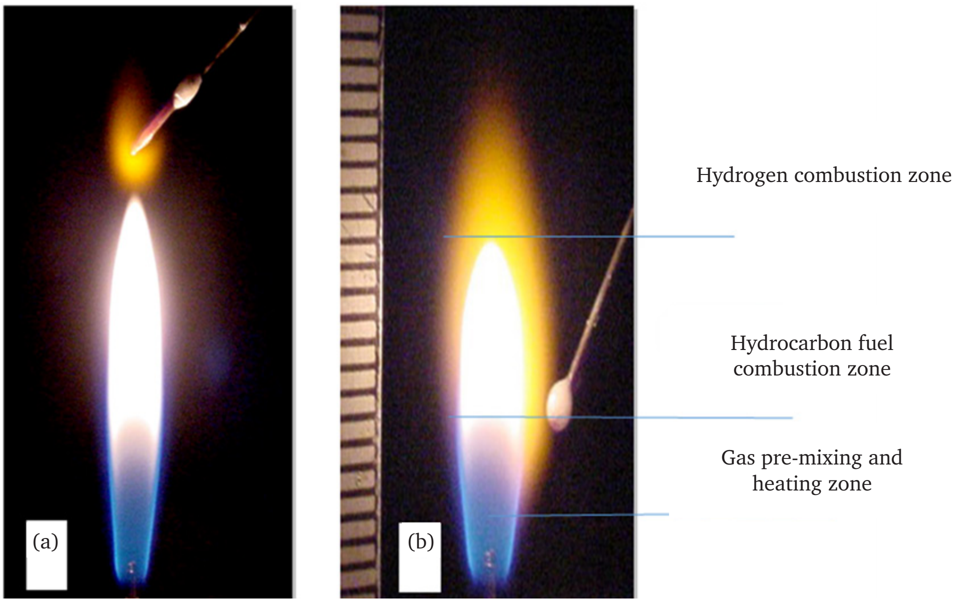

Figure 2. Visualization of the H_2 flame fragment during evaporation of NaCl molecules in a diffusion propane flame (a); visualization of a fragment of flame H_2 by evaporation of NaCl molecules in a diffusion propane flame from the side of the flame (b)

Note: a – flow velocity from tube v=4.6 m/s, tube diameter d=0.5 mm, and the volumetric flow rate in the evaporation zone of the flow from tube Q=0.9 cm^3/s; b – flow velocity from the tube v=4.6 m/s, tube diameter d=0.5 mm, the temperature in the zone of evaporation of salt molecules T=906K, the volume flow rate from the tube Q=0.9 cm^3/s

Source: developed by the authors

When the salt vapor is supplied from the side by the width of the hydrogen afterburning zone, the main contribution is given by diffusion, and from the side of flow propagation it is supplemented by the contribution due to the flow velocity, which is dominant. The expansion of the hydrogen after the burning zone following the flow direction of the gas mixture is related to this. The effect of the dependence on the flow velocity is particularly clear when comparing the pictures in Figure 3-4.

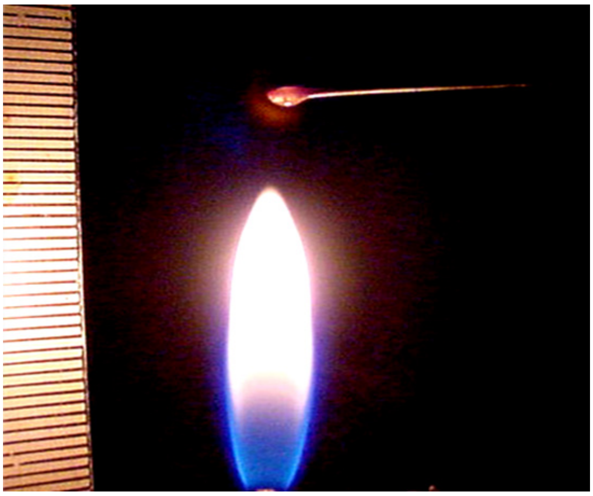

Figure 3. Visualization of the H_2 flame fragment by evaporation of NaCl molecules in a diffusion propane flame from the upper side of the flame

Note: Flow velocity from the tube v=6.07 m/s, tube diameter d=0.5 mm, the temperature in the zone of evaporation of salt molecules T=1406K, the volume flow rate from the tube Q=1.15 cm^3/s

Source: developed by the authors

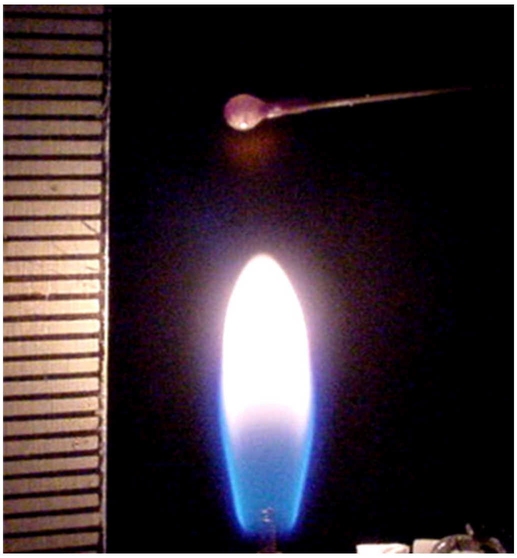

Figure 4. Visualization of the H_2 flame fragment by the evaporation of NaCl molecules in a diffusion propane flame from the side of the flame

Note: flow velocity from the tube v=4.6 m/s, tube diameter d=0.5 mm, the temperature in the zone of evaporation of salt molecules T=906K, the volume flow rate from the tube Q=0.9 cm^3/s

Source: developed by the authors

In Figure 3, when the volumetric flow rate Q=1.1 cm^3/s and the flow rate from the capillary v=6 m/s the hydrogen flame expands conditionally to 8 mm, and in the case of Figure 4, when the volumetric flow rate Q=0.9 cm^3/s and the flow rate from the capillary v=4.6 m/s the hydrogen flame spreads by only 6 mm. From this, it is easy to estimate the contribution of the flow velocity to the distribution of hydrogen concentration in its combustion zone.

The problem of the distribution of the concentration of hydrogen molecules over the distance behind the combustion zone of the main hydrocarbon fuel is of great interest. The proposed method of probing diffusion hydrocarbon flames and the experimental data obtained in this work allows us to develop a new method for studying the visible and invisible hydrogen afterburning zones in these flames. The balance equations for describing the kinetic regularities of the reaction medium development and describing the length of the second zone caused by the processes of substance transfer due to diffusion, convection, and kinetics of the combustion process, can be obtained by solving the corresponding diffusion-kinetic equations. Following the notations of Zh. Wang *et al.* [10], this equation can be represented in the following form (5):

$$\rho \frac{\partial Y_i}{\partial_t} + \rho V_x \frac{\partial Y_i}{\partial_x} + \frac{\partial}{\partial x}\left(\frac{J_{i,x}}{M_i}\right) + \sum_{k=1}^{r} \lambda_{ik} W_k \,, \qquad (5)$$

where: Y_i – species mass fraction, M_i – its molecular mass, ρ – density, t – time coordinate, v_i – speed in the x direction, $J_{i,x}$ – diffusion flux, λ_{ik} – stoichiometric coefficient of i-th reaction participant k, W_k – speed of this reaction.

When the values of all characteristic parameters are known, this equation allows us to obtain the structure of the flame. The method is based on the following considerations: if the concentration of sodium atoms in the reaction zone is known, the density of excited sodium atoms in the reaction zone, due to the processes $H+H(OH)+Na \rightarrow H_2O(H_2)+Na$ can be determined and with a known minimum value of the concentration of excited sodium atoms, whose glow can be registered visually, it can be estimated the concentration of hydrogen molecules in the zone where the glow comes to end. After that, from equation (5) it is possible to determine the distribution of hydrogen molecule concentration from the far along the course of H_2 flame propagation.

As shown in the works of Y. Chen *et al.* [9], and A.E. Long [12], using the generally accepted scheme of hydrocarbon oxidation, at atmospheric pressures above, when the length of the combustion zone of hydrogen molecules determines the reaction $H+O_2+M \rightarrow NO_2+M$, there is one rate describing the process, namely the reaction rate (6), in the right part of the equation (5), which describes the concentration distribution of H_2 at steady-state conditions:

$$W_{III} = k_6[O_2][M][H]. \qquad (6)$$

And in the combustion zone of intermediates, when the main fuel will be completely consumed, there is a relation of the type (7) [9; 10] for the value of hydrogen atom concentration where β is a proportionality factor:

$$[H] = \beta\, [O_2]^{1/2}[H_2]^{3/2}/[H_2O], \tag{7}$$

In the general case, when the mutual diffusion process of H_2 and O_2 is dominant, the concentrations of O_2 and H_2O will depend on the distance of hydrogen flame propagation. However, if the flow velocity dominates over the longitudinal diffusion, then at some distance from the zone of full consumption of the main fuel, when the diffusion penetration of oxygen and the delivery of H_2O by the jet into the H_2 flame zone dominates over the process of its flow rate, it can be assumed that the O_2 and H_2O flow in this zone can be neglected.

Under conditions of the predominance of mass flow over diffusive one, the main contribution to the distribution of H_2 concentration in equation (1) will be given by fluidity, hence, this equation can be represented in the form (8) within the framework of the above approximations:

$$\frac{d[H_2]}{dx} = -\alpha \cdot [H_2]\frac{3}{2}, \tag{8}$$

where: α is the proportionality constant.

If all salt molecules entering the flame are converted into sodium atoms, the value of α can be determined. With the known value of sensitivity of the camera to the emission of Na* quanta, it can be determined the value of excited atoms of Na* quantities formed per unit volume per unit time in the extreme zone of flame H_2. From reactions (5) and (6) it turns out:

$$[H]^2[Na]\, k = W_{Na*}, \tag{9}$$

where: ($k = 8109\ l^2/mol^2s$), WNa* is the reaction rate (1) or, in other words, it can be said the amount of Na* formed per unit time per unit volume.

The channels of consumption of the formed excited sodium atoms are the emission stabilization channel, the stabilization channel due to impact with atmospheric gas, and various probable reaction channels. Hence, it can be written (10) for the number of quanta released from a unit volume per unit of time:

$$N_{hv} = \frac{k_{r.s.} \cdot W_{Na*}}{K_{eff.} + k_{r.s.}}, \tag{10}$$

where: $k_{r.s.}$ is the rate constant of the radiation stabilization channel, $K_{eff.}$ – is the effective rate constant of Na* consumption through other channels (besides the channel of stabilization by radiation).

And therefore, for the rate of formation of excited sodium, it turns out (11):

$$W_{Na*} = \frac{N_{hv}(K_{eff.} + k_{r.s.})}{k_{r.s.}}. \tag{11}$$

As in the dominant flux conditions, the inflow of sodium-containing molecules from outside allows us to always choose the conditions under which the requirement of a single participation of sodium atoms in the act of three-frequency recombination with hydrogen atoms is established. And so, from (9) and (11), it can be written (12):

$$[H] = \sqrt{\frac{W_{Na*}}{[Na]\cdot k}} = \sqrt{\frac{N_{hv}(K_{eff.} + k_{r.s.})}{k_{r.s.}\cdot[Na]\cdot k}}. \tag{12}$$

And with the known sensitivity of the camera to the minimum number of photons from (7) it can be estimated the concentration of atoms H at the end of the luminous zone of the flame H_2. Since $k_{r.s} \gg K_{eff.}$ then the following is true (13):

$$[H] = \sqrt{\frac{N_{hv}}{[Na]\cdot k}}. \tag{13}$$

It is known that light radiation is observable if the number of photons in 1 cm^3 is about 4·1014. Then the number of photons in the area 6 mm from the luminous flame torch of Figure 2, it can be suggested that ~4·1014 photons/cm^3, k=8·109 l2/mol^2s, according to M. Kajita [25] the partial pressure of saturated vapors of food salt and baking soda at temperatures above 1000K is approximately equal to 7 torr which corresponds to (14):

$$[Na] = 2.45 \cdot 10^{17}\ \frac{particles}{cm^3}. \tag{14}$$

And accordingly obtained for the concentration of hydrogen atoms (15):

$$[H] \sim 4.28\ \cdot 10^{14}\frac{particles}{cm^3}. \tag{15}$$

It is also of interest to obtain the dependence of the concentration of hydrogen molecules on the distance after the zone of the luminous flame torch by the formula (8). From formula (7) it can be determined the concentration of hydrogen molecules in the extreme zone of the glow flame $H_{2(l)}$, where l is the length at which the sodium atoms glow ends. Integration of equation (8) within the range from an arbitrary point x to the edge of the visible hydrogen flame zone will give (16):

$$\frac{2}{\sqrt{[H_2]_1}} - \frac{2}{\sqrt{[H_2]_x}} = \alpha \cdot (1 - x), \tag{16}$$

where: $[H_2]_l$ and $[H_2]_x$ are concentrations of hydrogen molecules at points x and l, respectively.

When x<l, the relation $[H_2]_x \gg [H_2]_l$ (17) holds:

$$\alpha = \frac{2}{\sqrt{[H_2]_1}\cdot 1}. \tag{17}$$

And thus, a formula is obtained for estimating the parameter T at known distance visually from the hydrogen flame zone and their concentration in this zone. From here, using formula (8), it can be estimated the contribution of the blowout to the flame propagation values (Fig. 5).

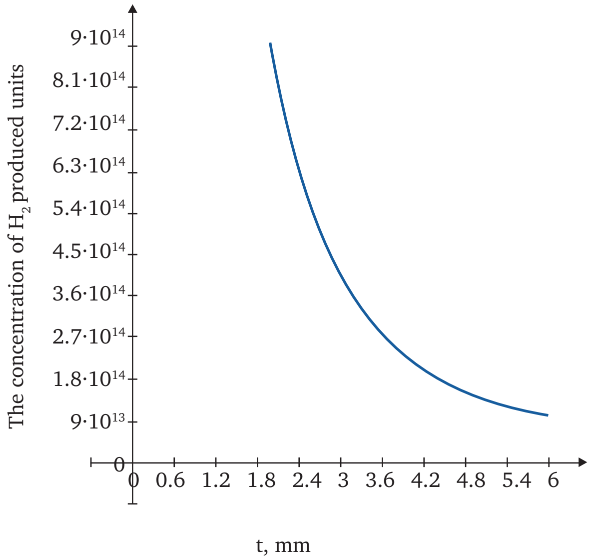

Figure 5. Distribution of the concentration of hydrogen molecules in the hydrogen afterburning zone in a diffusion propane flame in arbitrary units

Source: developed by the authors

Thus, visualization of the hydrogen flame by delivering alkali metal salts into the flame not only makes it possible to visualize this flame in the maximum possible size but also presents an opportunity to obtain a view of the distribution of the concentration of hydrogen molecules in this flame over its distribution distance and as a function of the flow rate and to estimate the growth rate of the hydrogen molecule concentration. As can be seen from Figure 4, the concentration of hydrogen molecules in the afterburning zone decreases 10 times in 6 mm.

Discussion

V. Mishra and S. Rashmi [26] considering methods for determining gas concentrations in general, argued that the use of methods related to optical absorption offers several advantages that alternative technologies cannot provide. Since measurements are based on a fundamental physical property of the molecule under study, there are ways to avoid some of the error mechanisms present in other technologies, including drift, lack of selectivity, and changes in sensitivity from experiment to experiment. Measuring the parameters of gases by optical means also opens several unique possibilities [27]. In particular, the adjustment of sensitivity, as well as the availability of feedback in the instrument, where one can monitor during operation whether they have failed (e.g., due to a faulty light source or failure to direct sufficient light to the photodetector). But the main advantage is the speed of signal transmission and the fact that measurements can be made in situ means that optical instruments can have a much higher response rate than alternative technologies.

The use of modern gas detection devices implies compliance with several requirements, such as high speed, minimum drift, and high gas selectivity, with zero sensitivity to other gases. Gas sensors with a carefully thought-out design using in their basis the phenomena of optical absorption can have time constants of less than 1 s, which provides them with high performance. Thus, the work by X. Liu and Y. Ma [28] shows an example of experimenting in real-time and situ without disturbing the gas sample, which is very important for process control. Such advantages of the approach are provided by the transduction method by directly measuring the physical absorption of the molecule at a certain wavelength. This leads to a reduction of drift in the system. In addition, it should be noted that the dependence on external factors drops significantly since it is possible to directly determine and control the intensity of the incident optical radiation. Considering all advantages, it can be stated that optical gas measurement is inherently very reliable, which allows it to take a place between inexpensive sensors with lower performance and high-quality laboratory equipment. The work by T. Strahl *et al.* [29] also shows a rather promising application of photoacoustic sensors for the calculation of gas concentrations. The described sensors differ in the approach used to detect absorbed light. Traditional sensors calculate the values of absorbed light to determine the transmittance, which can be obtained by comparing the light intensity at the photodetector with and without the presence of gas. Photoacoustic sensors, on the other hand, allow the absorbed light to be measured directly. Photoacoustic detection can be used in conjunction with the optical methods described above, including the method presented in this research.

In the quantitative study of gas concentrations, semiconductor gas sensors or electrochemical devices can compete with the traditionally dominant laboratory analytical equipment based on the effect of optical absorption by M. Kaloumenou *et al*. [30]. An example of such a device can be a pelistor, which, despite its relative cheapness, is a reliable device that responds to a change in gas concentration using a catalyst ball [31]. These devices have found widespread use in identifying flammable gases close to the lower explosive limit. The main disadvantage of pelistors compared to optical equipment is the zero drift at concentrations of fractions per million. In M.K. Nikolic's *et al*. [32] work, the efficiency and high sensitivity of other semiconductor gas sensors at low concentrations in the vicinity of ppm were shown. However, drift and low selectivity are present. In turn, electrochemical gas sensors can have high selectivity for individual gases at sensitivity in the region of particles per million or particles per billion [33], but they suffer from a limited lifetime as well as high humidity.

The mass spectrometric method described of C.P. Ruger's *et al*. [34], is based on the principle of separating ionized atoms and molecules according to the mass-to-charge ratio of the ion and the subsequent separate analysis. The amount of the desired component in the air is determined based on the proportional dependence of the spectral line intensity of each component on the partial pressure of the given component. It can provide a high sensitivity threshold of approximately 0.1 mg/m^3 and an error of up to 5%. However, the disadvantages of mass spectrometers compared to the presented solution are the high duration of analysis of the obtained data, the impossibility of creating compact devices, and the complexity of the ionization process [1; 2]. The biggest disadvantage of optical gas detection is its cost compared to material-based or electrochemical sensors. A second disadvantage is also reliability; in particular, the high degree of selectivity also means that several types of gas are difficult to detect simultaneously without a proportional increase in system complexity. Finally, using optical absorption, one must be guided by the information content available in the absorption spectrum. The second challenge is to be able to measure a wider range of gas compounds, particularly those composed of large molecules, including volatile organic compounds, which have a wider spectrum with less information content, requiring a wider wavelength coverage and greater accuracy and reliability of spectral fitting algorithms.

The use of the method of flame staining with sodium salts proposed in this work allowed us to significantly simplify the calculation of the concentration distribution of hydrogen molecules. In contrast to the absorption spectroscopy method widely used today [35], in method of this article the cost of operating the equipment is much lower. The sufficiently high accuracy and relative simplicity of the method make it promising for obtaining the hydrogen concentration distribution. In the future, the described approach can be applied to determine the concentrations of other gases in the combustion products, in particular, oxygen, methane, hydrogen sulfide, etc. The combination of experimental data and mathematical modeling makes it possible to visualize and qualitatively estimate the presence of hydrogen molecules along the entire combustion section. It should be noted that the calculations should take into account the sensitivity value of the charge-coupled device (CCD) matrix of the camera to the luminescence spectrum of alkali metal ions used for flame coloration. The use of sodium atoms in the experiment is explained by the fact that they have low electronic levels. This ensures their excitation with a small fraction of the heat released, which is another advantage of the method. The use of the semiempirical method to estimate the characteristics of gases is quite widely used today. Thus, in S. Muppala *et al*. [36], by applying an experimental and analytical model of two-component fuel mixtures of methane, propane, and hydrogen, the value of the turbulent flame combustion rate was obtained.

Ways of extending the capabilities of the method by using an additional hardware component are also considered. For example, the use of an infrared camera together with a conventional CCD camera is given in the article by B. Zhang *et al*. [24]. As a result of the proper selection of the temperature contour, it was possible to better determine the geometrical contour of the gas combustion flame. Such an approach can improve visibility and expand the possible applications of the method given in this work. When studying the properties of gases, the main parameters to be considered during the experiment are temperature and flow rate. The second parameter directly depends on the volumetric flow rate of the individual component of the gas flow, taking into account a set of chemical reactions and the effect of temperature. So, in O. Siryy [37], at a tube diameter of 75 mm the maximum combustion temperature of propane did not exceed 900K, and the reduction of the tube diameter to 0.5 mm resulted in a temperature increase in the molecular salt evaporation zone T>906K, which allowed a better evaluation of the flame coloration.

To summarize, despite the availability of several newer methods, the approach proposed in this work with the addition of alkali metal salts can be used to establish the concentration of hydrocarbon combustion products. The theoretical possibilities of extending the functionality may in the long term make its application effective at the level of modern optical methods for detecting gas molecules in the medium. The combination of a relatively simple setup with modern software solutions based on artificial intelligence will make it possible to build dependencies in real-time and conduct continuous data analysis.

Conclusions

From the theoretical data and results obtained in the course of the experiment in the presented work, the following conclusions can be drawn:

1. A semiempirical method for obtaining the distribution of hydrogen molecules in the flame during hydrocarbon combustion is presented. The experiment uses the delivery of alkali metal salt molecules, which can be used as an indication method for finding hydrogen ignition sources that cannot be visually detected.

2. As a result, a visualization of the hydrogen molecule concentration dependence over the entire combustion distance was obtained, which made it possible to obtain a view of the molecule distribution and estimate the rate of hydrogen concentration growth.

3. A series of studies on the shape, length, and experimental visualization of the structure of the diffuse hydrocarbon flame, carried out on the example of propane combustion, and the magnitude of the spread of the invisible flame combustion zone was established.

4. The intermediate product H_2, also allows to get the concentration of hydrogen atoms in the afterburning zone about 6 mm from the zone, the glowing flame of propane combustion.

5. The ways of future extending the functionality of the method based on modern approaches to detect and obtain gas concentrations are also analyzed. Namely, the use of photoacoustic methods or infrared cameras.

6. Based on the values of the parameters characterizing the experimental conditions, the value of hydrogen atoms at the end of the hydrogen-burning zone is calculated, which is also an important parameter of the diffusion flame and is the achievement of the method presented in the research.

In general, summarizing the results of the research, it can be stated that the combination of practical experiments with mathematical calculations has led to a new approach to determining the distribution of hydrogen molecules in the glow zone of the burning propane flame. Despite the relative simplicity of the proposed method, it was possible to determine the distribution of hydrogen concentration in the entire combustion zone very accurately. As a result, it is possible to talk about the prospects for developing new types of gas detectors or improving the capabilities of already known ones. The results obtained can be used in the laboratory for a better understanding of hydrocarbon combustion processes under diffuse flame conditions or in the industry for monitoring production processes under real-time conditions.

Conflict of Interest

The authors declare no conflict of interest.

Acknowledgement

None.

References

[1] Wang H, Liu Y, Sha Q. Influence of gas from long-flame coal spontaneous combustion on gas explosion limit. *Int J Chem Eng.* 2023;2023:5096109. doi: 10.1155/2023/5096109.

[2] Sengupta A, Gupta AK, Mirsh IM, Suresh S. One dimensional modeling of jet diffusion flame. *Int J Pure Appl Res Eng Technol*. 2018:16(4);320-33.

[3] Bosch C, Weterings R, Duijm N, Bakkum E, Mercx W, Berg A, *et al*. Methods for the calculation of physical effects. Vlinderweg: Publicatiereeks Gevaarlijke Stoffen; 2005. 870 p.

[4] Bradley D, Gaskell P, Gu X, Palacios A. Jet flame heights, lift-off distances, and mean flame surface density for extensive ranges of fuels and flow rates. *Combust Flame.* 2016;164:400-9. doi: 10.1016/j.combustflame.2015.09.009.

[5] Dadashzadeh M, Khan F, Hawboldt K, Amyotte P. An integrated approach for fire and explosion consequence modelling. *Fire Saf J.* 2013;61:324-37. doi: 10.1016/j.firesaf.2013.09.015.

[6] Mashhadimoslem H, Ghaemi A, Palacios A. A comparative study of radiation models on propane jet fires based on experimental and computational studies. *Heliyon*. 2021;7(6): e07261. doi: 10.1016/J.HELIYON.2021.E07261.

[7] Foroughi V, Palacios A, Mata C, Agueda A, Pastor E, Planas E, *et al*. An experimental study on geometrical features of horizontal sonic and subsonic jet fires. *Chem Eng Trans*. 2022;91:91-6. doi: 10.3303/CET2291016.

[8] Ba Q, Zhao M, Zhao Z, Huang T, Wang J, Li X, *et al*. Modeling of high pressure hydrogen jet fires. *J Tsinghua Univ*. 2022;62(2):303-311. doi: 10.16511/j.cnki.qhdxxb.2021.26.022.

[9] Chen Y, Wang J, Zhang X, Li C. The effects of CO_2 additional on flame characteristics in the $CH_4/N_2/O_2$ counterflow diffusion flame. *Molecules*. 2021;26(10):2905. doi: 10.3390/molecules26102905.

[10] Wang Zh, Sunderland PB, Axelbaum RL. Double blue zones in inverse and normal laminar jet diffusion flames. *Combust Flame*. 2020;211:253-259. doi: 10.1016/J.COMBUSTFLAME.2019.09.014.

[11] Wei Zh, Li M, Li S, Wang R, Wang C. Development of natural gas chemical kinetic mechanisms and application in engines: A review. *ACS Omega*. 2021;6(37):23643-53. doi: 10.1021/acsomega.1c03197.

[12] Long AE. A study of strained extinction for applications in natural gas combustion modeling. Cambridge: Massachusetts Institute of Technology; 2020. 20p.

[13] Tamadonfar P, Karimkashi Sh, Kaario O, Vuorinen V. Inner flame front structures and burning velocities of premixed turbulent planar ammonia/air and methane/air flames. *Flow, Turbul Combust.* 2022;109:477-513. doi: 10.1007/s10494-022-00341-x.
[14] Hamins A, Seshadri K. The structure of diffusion flames burning pure, binary, and ternary solutions of methanol, heptane, and toluene. *Combust Flame*. 1987;68(3):295-307. doi: 10.1016/0010-2180(87)90006-X.
[15] Celebi AT, Jamali SH, Bardow A, Vlugt TJH, Moultos OA. Finite-size effects of diffusion coefficients computed from molecular dynamics: A review of what we have learned so far. *Mol Simul.* 2021;47(10-11):831-45. doi: 10.1080/08927022.2020.1810685.
[16] Sargsyan HP. Using the Deductive – Inductive method to analyze diffusion mechanisms in complex systems. *Arm J Phys.* 2020;13(1):7-19.
[17] Sargsyan HP. On the value method of determining a dominant mechanism of nonlinear multicomponent diffusion. *J Contemp Phys*. 2020;55(4):550-558. doi: 10.3103/S1068337220040167.
[18] Sargsyan HP. Description of nonlinear diffusion in non-ideal multicomponent systems. *J Contemp Phys*. 2021;56(4):384-94. doi: 10.3103/S1068337221040149.
[19] Sargsyan HP. Conditions for consistency of equations of nonlinear diffusion in complex systems with thermodynamic constraints. *Arm J Phys.* 2021;14(3):154-64.
[20] Laider KJ. The chemical kinetics of excited states. Oxford: Oxford University Press; 1987. 531 p.
[21] Wróblewski T, Ushakou D. Stepwise excited-state double proton transfer and fluorescence decay analysis. *J Fluoresc.* 2023;33:103-111. doi: 10.1007/s10895-022-03042-w.
[22] Hecht ES, Chowdhury BR. Characteristic of cryogenic hydrogen flames from high-aspect ratio nozzles. *Int J Hydrogen Energy*. 2019;46(23):12320-8. doi: 10.1016/j.ijhydene.2020.08.265.
[23] Pio G, Carboni M, Mocellin P, Pilo F, Vianello C, Maschio G, *et al*. Jet fires of hydrogen-methane mixtures. *Chem Eng Trans*. 2022;9:28-94. doi: 10.3303/CET2291049.
[24] Zhang B, Liu Y, Laboureur D, Mannan M. Experimental study on propane jet fire hazards: Thermal radiation. *Ind Eng Chem Res.* 2015;54(37):9251-6. doi: 10.1021/acs.iecr.5b02064.
[25] Kajita M. Standards of physical quantities. In: Measuring Time: Frequency measurements and related developments in physics. Bristol: IOP Publishing Ltd; 2018. P. 1-7.
[26] Mishra V, Rashmi S. Optical gas sensors. In: Dhara S, Dutta G, editors. Metal-oxide gas sensors. London: IntechOpen; 2022. p. 116-164. doi: 10.5772/intechopen.108971.
[27] Pan Y, Zhao J, Lu P, Sima C, Zhang W, Fu L, *et al*. All-optical light-induced thermoacoustic spectroscopy for remote and non-contact gas sensing. *Photoacoustics*. 2022;27:100389. doi: 10.1016/j.pacs.2022.100389.
[28] Liu X, Ma Y. Tunable diode laser absorption spectroscopy based temperature measurement with a single diode laser near 1.4 μm. *Sens*. 2022;22(16):6095. doi: 10.3390/s22166095.
[29] Strahl T, Herbst J, Maier E, Rademacher S, Weber C, Pernau HF, *et al*. Comparison of laser-based photoacoustic and optical detection of methane. *J Sens and Sens Sys.* 2021;10:25-35. doi: 10.5194/jsss-10-25-2021.
[30] Kaloumenou M, Skotadis E, Lagopati N, Efstathopoulos E, Tsoukalas D. Breath analysis: A promising tool for disease diagnosis – The role of sensors. *Sens.* 2022;22(3):1238. doi: 10.3390/s22031238.
[31] Brauns E, Seemann T, Zollmer V. A miniaturized catalytic gas sensor for hydrogen detection containing a high porous catalytic layer formed by dry lift-off. *Procedia Eng.* 2012;47:1149-52. doi: 10.1016/j.proeng.2012.09.355.
[32] Nikolic MV, Milovanovic, Vasiljevic ZZ, Stamenkovic Z. Semiconductor gas sensors: Materials, technology, design, and application. *Sens.* 2020;20(22):6694. doi: 10.3390/s20226694.
[33] Huang X, Xhu Y, Kianfar E. Nano biosensors: Properties, applications and electrochemical techniques. *J Mater Res Technol.* 2021;12:1649-72. doi: 10.1016/j.jmrt.2021.03.048.
[34] Ruger CP, Tiemann O, Neumann A, Streibel T, Zimmermann R. Review on evolved gas analysis mass spectrometry with soft photoionization for the chemical description of petroleum, petroleum-derived materials, and alternative feedstocks. *Energy Fuels*, 2021;25(22):18308-32. doi: 10.1021/acs.energyfuels.1c02720.
[35] Banik GD, Maity A, Som S, Pal M, Pradhan M. An external-cavity quantum cascade laser operating near 5.2 μm combined with cavity ring-down spectroscopy for multi-component chemical sensing. *Laser Phys.* 2018;28:045701. doi: 10.1088/1555-6611/aaaa55.
[36] Muppala S, Manickam B, Dinkelacker F. A comparative study of different reaction models for turbulent methane/hydrogen/air combustion. *J Therm Eng.* 2015;1:367-80. doi: 10.18186/jte.60394.
[37] Siryy O. The influence of jet-niche system parameters on the working process of burner devices. Kyiv: National Technical University of Ukraine; 2016. 198 p.

Дифузійне полум’я та напівемпіричний метод оцінки розподілу молекул водню в полум’ї пропану

Гарник Саргсян
Кандидат фізико-математичних наук, старший науковий співробітник
Інститут хімічної фізики А.Б. Налбанд’яна Національної академії наук Республіки Вірменія
0014, вул. Паруїр Севак, 5/2, м. Єреван, Республіка Вірменія
https://orcid.org/0000-0002-4832-0623

Петрос Гукасян
Доктор хімічних наук, старший науковий співробітник
ТОВ «ЕКОАТОМ»
0082, вул. Адана, 1, м. Єреван, Республіка Вірменія
https://orcid.org/0009-0003-5569-0360

Грача Саргсян
Кандидат фізико-математичних наук, старший науковий співробітник
Інститут хімічної фізики А.Б. Налбанд’яна Національної академії наук Республіки Вірменія
0014, вул. Паруїр Севак, 5/2, м. Єреван, Республіка Вірменія
https://orcid.org/0009-0006-4188-158X

Руслан Анатолійович Поведа
Кандидат фізико-математичних наук, доцент
Кам’янець-Подільський Національний Університет імені Івана Огієнка
32301, вул. Огієнка, 61, м. Кам’янець-Подільський, Україна
https://orcid.org/0000-0002-0067-6153

Анотація

Актуальність. Найбільша ефективність у визначенні основних характеристик спалювання газу була показана оптичними методами завдяки їх високій швидкості та точності. Незважаючи на всі переваги цих методів, їх головним недоліком є ціна та складання реалізації. Тому сьогодні необхідно вдосконалити підходи до вирішення цієї проблеми.

Мета. Дослідження присвячено вивченню полум’я дифузії напівемпіричним методом.

Методи. Дані експериментального дослідження дифузійного полум’я вуглеводнів представлені на прикладі пропану. Для візуалізації невидимої частини структури цього полум’я, а саме зони догоряння молекул водню, що утворюються в полум’ї у нерівноважних кількостях, у зоні полум’я випаровуються молекули, що містять атоми лужних металів (NaCl та Na_2CO_3).

Результати. Вперше застосовувався метод доставки молекул солей лужних металів ззовні, що дозволило більш ретельно дослідити це явище. На основі результатів досліджень, метод визначення концентрації атомів водню та відносного розподілу концентрації молекул водню вздовж осі поширення полум’я після запропонованої зони спалювання. Метод дослідження поєднує експерименти з математичним моделюванням. Застосування методу, описаного у статті, дозволяє визначити розподіл молекул водню над зоною світіння основного палива.

Висновки. Отримані результати допоможуть краще зрозуміти явища горіння вуглеводнів в умовах дифузійного полум’я, а також пошук нових способів отримання палива водню від домашніх відходів

Ключові слова: атом; паливо; сенсори; фізичні ефекти; газ

Scientific Herald of Uzhhorod University
Series "Physics"
Journal homepage: https://physics.uz.ua/en
Issue 53, 53-63
Received: 04/12/2023. Revised: 05/14/2023. Accepted: 06/01/2023

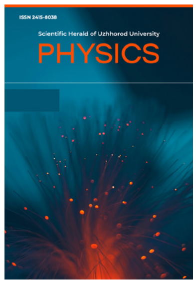

UDC 538.951
PACS 62.20.Dc, 62.20.Fe
DOI: 10.54919/physics/53.2023.53

Elastic-plastic properties of $Li_2B_4O_7$ determined by nanoindentation

Iryna Chobal
Assistant
Uzhhorod National University
88000, 3 Narodna Sq., Uzhhorod, Ukraine
https://orcid.org/0009-0002-5021-5184

Oleksandr Chobal*
PhD in Physical and Mathematical Sciences, Associate Professor
Uzhhorod National University
88000, 3 Narodna Sq., Uzhhorod, Ukraine
https://orcid.org/0000-0002-8042-8052

Yuliia Myslo
PhD in Physical and Mathematical Sciences, Associate Professor
Uzhhorod National University
88000, 3 Narodna Sq., Uzhhorod, Ukraine
https://orcid.org/0000-0001-6771-2844

Ivan Petryshynets
PhD in Technical Sciences, Senior Researcher
Institute of Materials Research of Slovak Academy of Sciences
04001, 47 Watsonova Str., Košice, Slovakia
https://orcid.org/0000-0001-8001-5349

Vasyl Rizak
Doctor of Physical and Mathematical Sciences, Professor
Uzhhorod National University
88000, 3 Narodna Sq., Uzhhorod, Ukraine
https://orcid.org/0000-0002-9177-0662

Suggested Citation:
Chobal I, Chobal O, Myslo Yu, Petryshynets I, Rizak V. Elastic-plastic properties of $Li_2B_4O_7$ determined by nanoindentation. *Sci Herald Uzhhorod Univ Ser Phys.* 2023;(53):53-63. doi: 10.54919/physics/53.2023.53

*Corresponding author

Abstract

Relevance. Crystalline and amorphous lithium tetraborate ($Li_2B_4O_7$) has a wide range of practical applications due to its physical properties. The knowledge of the mechanical characteristics of the surface layers of these materials, which are studied by nanoindentation, is necessary for optimising the technological processes for obtaining "optically perfect" samples.

Aim. A comparative study of the mechanical properties and deformation mechanisms of glassy and crystalline $Li_2B_4O_7$ samples in a wide range of applied loads.

Methodology. The elastic-plastic properties of crystalline and glassy lithium tetraborate were investigated using the multiple-loading cyclic nanoindentation method. The samples were measured at maximum loading forces of 50, 100, 150, 200, 250, 300, 350, 400, 450, and 500 mN. Four measurements (in the form of a 2x2 matrix) were made at a distance of 50 μm from each other on each sample and at each load. Young's modulus, hardness, and Poisson's ratio of $Li_2B_4O_7$ glass were also calculated using the Makishima-Mackenzie theory.

Results. The load-displacement curves and graphs of the dependence of the average contact pressure on the displacement of the diamond Berkovich indenter were obtained, which have a "smooth" shape and no anomalies associated with "pop-in" or "pop-out" effects. The indentation modulus (Young's modulus *E*) and hardness *H* of the studied samples were obtained from the experimental *P-h* load-displacement diagrams. The measured values mainly depend on the applied load or the contact depth of the indenter penetration into the crystalline and vitreous lithium tetraborate.

Conclusions. Both the hardness and Young's modulus of $Li_2B_4O_7$ glass are lower than those of the single crystal, indicating a lower resistance of amorphous lithium tetraborate to elastic and plastic deformations. The obtained experimental values of hardness and Young's modulus of $Li_2B_4O_7$ glass correlate well with the results of the calculation within the framework of the Makishima-Mackenzie theory. Multiple-loading cyclic nanoindentation leads to deformation densification of glassy $Li_2B_4O_7$ due to changes in the angles and lengths of chemical bonds, which leads to a decrease in the free volume in the medium-order structure of glass, as well as a change in the coordination of Boron atoms relative to Oxygen, i.e., the transformation of three-coordinated Boron into four-coordinated Boron

Keywords: lithium tetraborate crystals; Li_2O-$2B_2O_3$ glass; deformation densification; Young's modulus; hardness; phase transition

Introduction

The research interest in the superionic conductor lithium tetraborate ($Li_2B_4O_7$) is determined by its broad prospects for use in nonlinear optical and piezoelectric devices. Lithium tetraborate is a promising nonlinear material for laser frequency conversion, including for generating the fourth and fifth harmonics of Nd:YAG lasers [1] and sub-terahertz radiation [2]. In addition, following Sahil *et al.* [3] and Mehrabi *et al.* [4], $Li_2B_4O_7$ crystals (doped with various impurities) have wide application possibilities in radiation dosimetry. The study by J. Puebla *et al.* [5] indicates that other applications of $Li_2B_4O_7$ include surface and bulk acoustic wave devices, cellular phones, and data transmission devices. Lithium-borate glasses are of great interest due to their good ionic conductivity properties [6] and potential use in solid-state batteries [7; 8].

F. Pöhl [9] substantiated that indentation testing, in particular nanoindentation, is widely used to determine the local mechanical characteristics of materials and individual phases in multiphase materials. A. Gouldstone [10] found that it allows determining important mechanical parameters (e.g., hardness and Young's modulus) and energy characteristics of load-unload cycles, and greatly contributes to the understanding of mechanical behaviour on the nanometre scale, during which unique deformation phenomena often occur. Thus, previously, in [11; 12], nanoindentation of crystalline $Li_2B_4O_7$ was carried out in a limited range of applied loading forces. In particular, the authors of [11] recorded a discontinuity in the graph of the dependence (the so-called "pop-in" effect) of the indenter loading force on the depth of its penetration into the plane (100) of the lithium tetraborate crystal, which was explained by the nucleation of dislocations or possible phase transitions in the $Li_2B_4O_7$ crystal under compression. However, later, the authors of [12] did not observe the "pop-in" effect on the load-depth indentation curves in the same plane [100]. The corresponding experimental studies were conducted with only two loading forces, which did not allow to fully study the dimensional effects of nanoindentation. Interestingly, the pop-in effect can also be caused by pressure-induced surface amorphisation of the crystal [13]. Given that reversible or irreversible amorphisation (depending on the magnitude of the external force) of lithium tetraborate crystals during bulk compression was previously reported [14], as well as the presence of conflicting literature data on mechanical properties and possible phase transformations under pressure, this study was conducted.

The study aims to conduct a comparative study of the mechanical properties and deformation mechanisms of glassy and crystalline $Li_2B_4O_7$ samples in a wide range of applied loads.

Materials and Methods

Experimental measurements were performed by cyclic nanoindentation with multiple loading with a maximum force of 50-500 mN and hold at the peak load for a certain time, which allows considering the viscoelastic component of the deformation and avoiding errors in determining elastic moduli from unloading curves [15; 16]. Lithium tetraborate was obtained according to the author's method [17] by gradual melting of pre-dewatered high-purity boron oxide B_2O_3 and lithium carbonate Li_2CO_3 in a platinum crucible in the air. Single crystals of $Li_2B_4O_7$ were grown by the Chokhralsky method in an air atmosphere in an HX-620 unit with automatic diameter control.

To obtain vitreous $Li_2B_4O_7$, the composition of which corresponded to the stoichiometric composition and contained a minimum number of impurities, a part of a single crystal of $Li_2B_4O_7$, which did not contain solid-phase and gas inclusions, was used as a starting material. It was melted in a platinum crucible in the air at a temperature of 1240-1290 K and then cooled in the quenching mode. To relieve thermal stresses, the glass removed from the crucible was annealed for 2-4 hours at 550-600 K. The glassy state of the obtained samples was confirmed by X-ray diffraction analysis, which confirmed the absence of characteristic peaks in the X-ray diffraction patterns that would indicate the presence of crystalline inclusions.

The samples used to study the mechanical properties were cut from crystalline and glassy $Li_2B_4O_7$ in the form of rectangular parallelepipeds with dimensions of about 5×5×10 mm. The orientation accuracy of the single-crystal samples relative to the crystallographic direction [100] was at least 0.5°. Both samples were ground and polished.

To determine the mechanical properties, indentation tests were performed on a Nanoindenter G200 using a Berkovich pyramidal diamond indenter. The nanoindentation procedure is performed by applying a load to the diamond indenter and recording the depth of its penetration into the material under test. This is done in the loading and unloading mode. Based on the obtained load-displacement curve, the elastic modulus and hardness of the sample material are automatically calculated following ISO 14577 [18] and the Oliver-Farr method [19].

The samples ($Li_2B_4O_7$ glass and single crystal of orientation [100]) were measured with a maximum force of 50, 100, 150, 200, 250, 300, 350, 400, 450, and 500 mN. Four measurements were made (in the form of a 2x2 matrix) at a distance of 50 μm from each other on each sample and under each load. The Poisson's ratios used for the calculation were 0.202 for vitreous [20] and 0.35 for crystalline $Li_2B_4O_7$ (averaged value [21]), the speed of approach to the surface was 10 nm/s, and the permissible drift rate was 0.05 nm/s.

The experiment was conducted by the method of multiple-loading cyclic nanoindentation with a trapezoidal function of the loading force (Fig. 1).

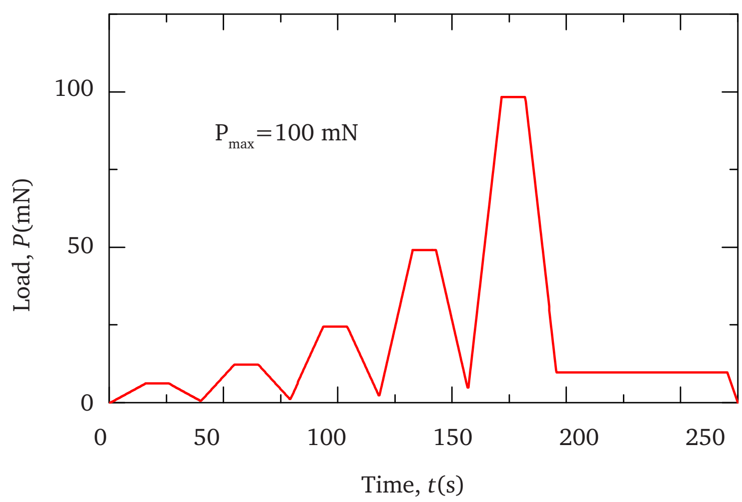

Figure 1. Typical load force dependence on indentation time used in this study
Source: compiled by the authors

Each test consisted of 5 loading and unloading cycles with a clear time interval: loading and unloading lasted 15 s, and peak force hold was 10 s (to avoid errors in determining experimental parameters due to the possible influence of viscoelastic and visco-plastic deformations). To calculate the hardness and elastic moduli of the studied materials during multiple nanoindentations in each indentation cycle, the NIGET software [22] was used within the framework of the Oliver-Farr technique [19].

For glassy lithium tetraborate, the elastic modulus *E* and Poisson's ratio ν were also calculated within the framework of Makishima and Mackenzie's theory [23; 24], which assumes that *E* is a function of the packing density of glass components V_i (determined by the ionic radii of the elements) and the dissociation energy G_i, which characterises the average strength of chemical bonds in glass:

$$E = 2V_t G_t\,, \tag{1}$$

$$\nu = 0.5 - \frac{1}{7.2V_t} \tag{2}$$

$$V_t = \frac{\rho}{M}\sum_i X_i V_i\,, \tag{3}$$

$$G_t = \sum_i X_i G_i\,, \tag{4}$$

where X_i – a molar fraction of the i-th glass component, ρ – density, M – a molar mass of the glass under study.

Results and Discussions

Figure 2 shows a typical dependence of the loading force (*P*) on the depth of penetration of the indenter (*h*) into the surface of the materials under study after 5 loading and unloading cycles with a maximum force of 100 mN in the crystallographic direction [100] of $Li_2B_4O_7$ crystals (Fig. 2a) and glassy $Li_2B_4O_7$ (Fig. 2b).

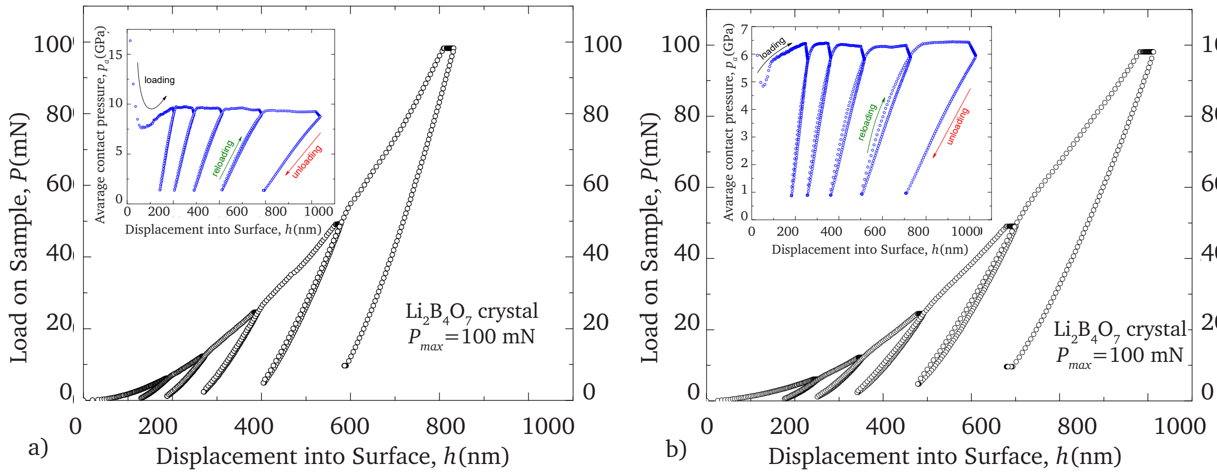

Figure 2. Dependence of the loading force (*P*) on the indenter displacement (*h*) into the surface (100) of a single crystal (a) and glassy $Li_2B_4O_7$ (b). The insets show the dependence of the average contact pressure on the indenter penetration depth

Source: compiled by the authors

The shape of the *P-h* diagrams is determined by the elastic, viscoelastic, and plastic properties of the materials under study. In particular, a preliminary conclusion can be made about the higher values of hardness and elastic moduli of crystalline $Li_2B_4O_7$, as well as a slight predominance of viscoelastic properties of vitreous lithium tetraborate (estimated by the area of hysteresis loops [25; 26]) based on the comparison of the obtained curves (Fig. 2). For a detailed analysis of the results obtained, the average contact pressure exerted on the sample during indentation was also estimated (insets in Fig. 2) using the ratio of the loading force P_i to the area of contact between the indenter and the material at the contact depth $A=f(h_c)$. It is worth noting that the indenter displacement *h* is automatically measured during the nanoindentation test, which is the sum of the contact depth h_c and the elastic deflection h_{el} of the sample surface at the contact edge. Therefore, to monitor the average contact pressure during the indenter movement, the method proposed by the authors of [27; 28] was used. In particular, the instantaneous value of the elastic deflection $h_{el(i)}$ of the sample surface near the contact perimeter was obtained by Eq:

$$h_{el(i)} = h_{el(max)}\left(\frac{P_i}{P_{max}}\right)^{\frac{1}{2}}, \tag{5}$$

where P_i, P_{max} – instantaneous and maximum loads on the sample, respectively; $h_{el(max)}$ – elastic deflection of the sample surface at the maximum load, determined according to the Oliver-Farr method [16]:

$$h_{el(max)} = \varepsilon\frac{P_{max}}{S}\,, \tag{6}$$

where ε – geometric constant (ε=0.75 for the Berkovich indenter used in this study), and *S* – contact stiffness of the specimen at the maximum load P_{max}.

The analysis of the obtained *P-h* diagrams and graphs of the dependence of the average contact pressure on the depth of penetration of the indenter into the surface of vitreous and crystalline $Li_2B_4O_7$ over the entire range of studied loads indicates their smooth shape and the absence of anomalies associated with "pop-in" or "pop-out" effects. At the initial stage of the curves, a directly proportional relationship between load and strain was recorded, indicating a purely elastic mechanism of deformation of lithium tetraborate in the nanoregion. The unloading curve at the initial stage, which describes the elastic recovery of the material, is also linear. According to the Oliver-Farr methodology [16], the slope of this *dP/dh* dependence determines the contact stiffness *S* at the point of maximum load (P_{max}, h_{max}):

$$S = \frac{dP}{dh}|_{h=h_{max}} . \qquad (7)$$

By knowing the contact stiffness, it is possible to determine the reduced modulus E_r, which considers the deformation of both the indenter and the sample, and accordingly allows determining Young's indentation modulus *E* and the hardness *H* of the test sample [29]:

$$E_r = \frac{S\sqrt{\pi}}{2\beta\sqrt{A}}, \qquad (8)$$

$$E = (1-\nu^2)\left[\frac{1}{E_r} - \frac{1-\nu_i^2}{E_i}\right]^{-1}, \qquad (9)$$

$$H = \frac{P_{max}}{A}. \qquad (10)$$

A – an area of contact between the indenter and the material; β – factor determined by the geometry of the indenter and equal to 1.034 for the Berkovich indenter; ν_i=0.07 and E_i=1140 GPa (Poisson's ratio and Young's modulus, respectively, for diamond indenter).

Figure 3 shows the results of *E* and *H* measurements obtained by analysing the *P-h* diagrams of nanoindentation during a series of tests with maximum loads of 50-500 mN. As can be seen from the figure, Young's modulus and hardness measurements of lithium tetraborate with a relatively small standard error of the experiment depend on the applied load (Figs. 3a, 3c) or the contact depth of the indenter (Figs. 3b, 3d). This is a manifestation of the so-called Indentational Size Effect (ISE), for which various mechanisms have been previously proposed [30; 31].

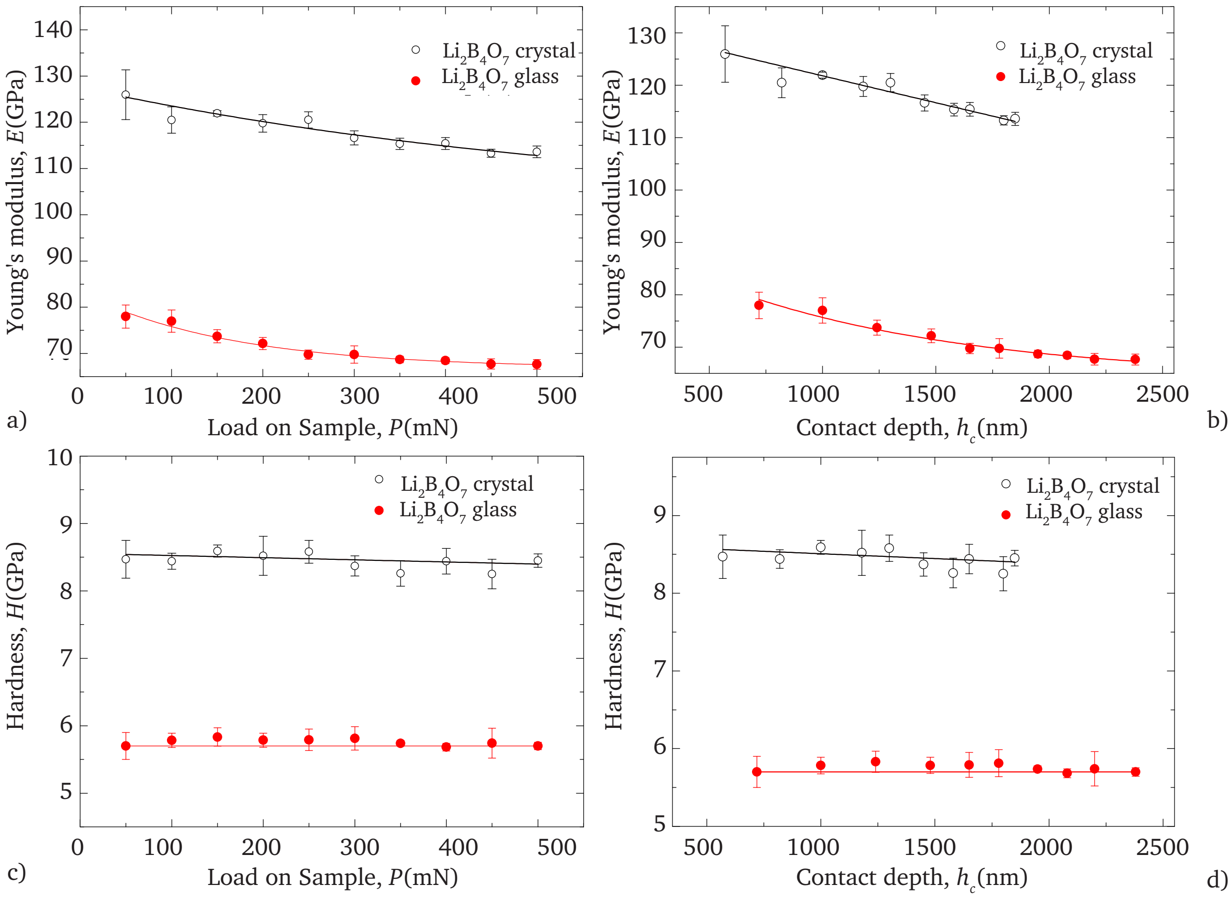

Figure 3. Young's modulus (a, b) and hardness (c, d) as a function of applied load (a, c) and contact depth (b, d) for the $Li_2B_4O_7$ glass and (100) plane of the single crystal
Source: compiled by the authors

As can be seen from Figures 3a, and 3b, the value of Young's modulus for both single crystal and glass samples is higher on the free surface and tends to decrease with increasing load and contact depth. For vitreous $Li_2B_4O_7$, a tendency to saturate the obtained *E* values with an increase in the penetration depth in the studied range was recorded. Study [32] reports the value of Young's modulus of the $Li_2B_4O_7$ crystal $E_{[100]}=12.8 \cdot 10^{10}$ Nm^{-2}, which was obtained from measuring ultrasonic wave velocities. The results of the *E* measurement by nanoindentation are in good agreement with these data, considering the size effects. Figures 3c, and 3d show the hardness versus loading force for single crystal and glassy lithium tetraborate samples. It was found that the hardness value for the $Li_2B_4O_7$ crystal in the studied load range decreases very slowly with increasing load, which also indicates a moderate ISE. At the same time, the hardness of lithium tetraborate glasses is practically independent of the indentation depth and applied load. In general, the obtained experimental values of *H* and *E* for crystalline lithium tetraborate are higher compared to the glassy one, which indicates a much lower resistance of $Li_2B_4O_7$ glass to elastic and plastic deformations.

Let us compare the experimentally obtained values of Young's modulus and hardness of glassy $Li_2B_4O_7$ with those calculated theoretically within the framework of Makishima and Mackenzie's theory [23; 24]. Lithium tetraborate glass consists of lithium oxide Li_2O and boron oxide B_2O_3 in a ratio of 1:2. According to S. Inaba [33], the values of the packing density coefficient V_{Li_2O} and dissociation energy G_{Li_2O} for lithium oxide are 8.0 cm^3/mol and 77.9 kJ/cm^3, respectively. The same parameters for boron oxide depend on the structural units from which the glass is formed. It is known from the study [34] that lithium tetraborate glass contains BO_3 and BO_4 structural units in equal proportions, i.e., the amount of tricoordinate boron relative to oxygen is equal to the amount of tetracoordinate boron ($N_3=N_4$). Accordingly, the dissociation energy and packing density coefficient of B_2O_3 has two values each: $G_3=15.6$ kJ/cm^3 [33], $V_3=15.2$ cm^3/mol [35] (three-coordinated boron atoms) and $G_{4\,t}=82.8$ kJ/cm^3 [33], $V_4=20.8$ cm^3/mol [35] (four-coordinated boron atoms). Therefore, to calculate the elastic modulus according to Y.B. Saddeek [36], the values of the dissociation energy and packing density were used, considering the ratio of fractions of three-coordinated and four-coordinated boron ($N_3=N_4=0.5$) in amorphous Li_2O-$2B_2O_3$:

$$G_{B_2O_3} = N_4 G_4 + N_3 G_3 \,, \tag{11}$$

$$V_{B_2O_3} = N_4 V_4 + N_3 V_3 \,. \tag{12}$$

Thus, using formulas (1-4) and (11-12), the value of Young's modulus for $Li_2B_4O_7$ glass was calculated – $E=67.2$ GPa, which is in full agreement with the experimentally obtained value of the indentation modulus within the measurement error. The calculated Poisson's ratio $\nu=0.25$ is slightly higher than the experimental value $\nu=0.202$ [20].

Considering the relationship between Young's modulus of an isotropic medium, Poisson's ratio and hardness:

$$H = \frac{(1-2\nu)}{6(1+\nu)} E, \tag{13}$$

the hardness of $Li_2B_4O_7$ glass $H=5.58$ GPa was also calculated, which almost completely coincides with the microhardness value obtained by nanoindentation.

The modulus of elasticity and hardness of amorphous and crystalline lithium tetraborate quantify the general variations in elastic and plastic deformation of materials under contact loading, but they do not fully describe the nature of the deformation process. A better understanding of the deformation features can be obtained by analysing the cyclic processes of multi-step loading and unloading within the energy approach [37; 38]. As a factor of mechanical losses during macroscopic fatigue tests, researchers usually use the ratio of the work W_{plast} spent on plastic deformation to the total work W_{total} consumed by the nanoindenter actuator: $\Psi=W_{plast}/W_{total}$. The proportion of plastic deformation energy (W_{plast}) in the work consumed by the nanoindenter actuator is determined by the area of the loop formed by the loading and unloading curves in one cycle [38]. As follows from the results obtained (Fig. 4), after five loading and unloading cycles, Ψ decreases for lithium tetraborate glass and remains almost constant for $Li_2B_4O_7$ single crystal over the number of cycles used in the experiment. In each loading-unloading cycle during multiple nanoindentations, the elastic modulus and hardness of lithium tetraborate glass were determined using the NIGET software [22] using the unloading curves (Fig. 2b). The results indicate that the hardness of glassy $Li_2B_4O_7$ increases with each indentation cycle from about 5.4 to 6.9 GPa, and Young's modulus varies between 81 and 92 GPa, showing an upward trend in some areas.

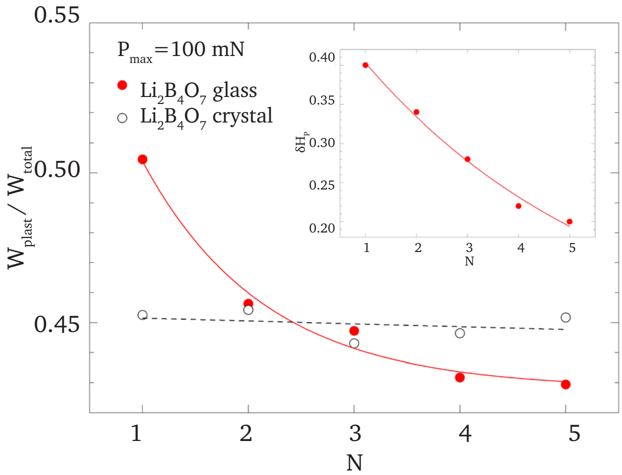

Figure 4. Variation W_{plast}/W_{total} during cyclic nanoindentation of $Li_2B_4O_7$ single crystal and glass. The inset shows the change in the plasticity parameter δH_p of glassy $Li_2B_4O_7$ during five nanoindentation cycles
Source: compiled by the authors

Thus, the observed decrease in the proportion of plastic strain energy in $Li_2B_4O_7$ glass can be qualified as the strengthening of the near-surface layers under the action of local loading. Knowing the *H/E* ratio in each nanoindentation cycle and the Poisson's ratio, the plasticity parameter δH_p of the material can be calculated by the equation [39]:

$$\delta H_P = 1 - 14.3(1 - \nu - 2\nu^2)H/E \ . \quad (14)$$

Considering the increase in the *H/E* ratio with each subsequent indentation cycle, we conclude that the plasticity parameter of glassy $Li_2B_4O_7$ decreases (inset in Fig. 4), which is consistent with the previous conclusion based on the energy approach. Thus, the comparative analysis of the deformation mechanisms of crystalline and glassy lithium tetraborate indicates the dominance of the elastic deformation mechanism of crystalline $Li_2B_4O_7$, which does not depend on the number of indentation cycles. Instead, the contribution of the plastic component to the deformation of glassy $Li_2B_4O_7$ gradually decreases, transforming into an elastic and viscoelastic deformation mechanism.

The plastic deformation of glass is mainly determined by two competing mechanisms – glass densification under the indenter or plastic shear flows [40]. Given the relatively low value of the Poisson's ratio of $Li_2B_4O_7$ glass ($\nu \approx 0.2$), according to the results of [41], it can be concluded that the densification effect will be dominant compared to the processes of plastic shear flow in the glass under study. Also, the *H/E* ratio for the glass under study is about 0.1. This indicates the covalent nature of the chemical bonds and a very low probability of plastic shear according to [42]. At the same time, the obtained estimates of the average pressure generated in the contact plane (Fig. 2b) of vitreous $Li_2B_4O_7$ with the indenter indicate the occurrence of variable contact pressure in the range of 1-6.5 GPa during loading and unloading. This pressure corresponds to areas I, and II of hydrostatic compression of lithium tetraborate glass in [43], where it was concluded that in these intervals glass compaction processes occur due to topological variations in the angles and lengths of chemical bonds, which leads to a decrease in the free volume, as well as the transformation of three-coordinated boron into four-coordinated boron.

Finally, the possibility of amorphisation of crystalline $Li_2B_4O_7$ in the process of nanoindentation is evaluated. The average contact pressure during the indentation of a single crystal of lithium tetraborate (inset in Fig. 2a) is about 15 GPa at the beginning of indentation, and then gradually decreases, reaching constant values of about 10 GPa, and decreases to 1-2 GPa during unloading. Thus, comparing these values with the results of [14], we conclude that the indenter pressure is insufficient for the amorphization of the crystalline sample, requiring more than 17 GPa for the reverse amorphization of crystalline $Li_2B_4O_7$. This conclusion is qualitatively consistent with the results of [12], where no features associated with phase transformations were found on the nanoindentation curves of lithium tetraborate crystals in the (100) plane.

Conclusions

The elastic and plastic properties of crystalline and vitreous lithium tetraborate have been investigated by cyclic nanoindentation with repeated loading with a maximum force of 50-500 mN. The load-unload curves depending on the displacement of the diamond indenter and the graphs of the average contact pressure dependence were obtained, which have a smooth shape and no anomalies associated with "pop-in" or "pop-out" effects. The values of the indentation modulus (Young's modulus *E*) and the hardness *H* of the studied samples were obtained from the experimental

P-h diagrams. It is shown that the measured values mainly depend on the applied load or the contact depth of the indenter penetration into crystalline and glassy $Li_2B_4O_7$. The experimentally obtained parameters of mechanical deformation of lithium tetraborate glass are in good agreement with the theoretically calculated hardness, elastic modulus, and Poisson's ratio within the framework of Makishima and Mackenzie's theory. In general, the obtained experimental values of H and E for lithium tetraborate crystals are higher compared to the same parameters for glasses of the same composition, which indicates a much lower resistance of glassy $Li_2B_4O_7$ to elastic and plastic deformations.

The contrasting evolution of the relative work of plastic deformation and the plasticity parameter of the studied samples during cyclic nanoindentation indicates significantly different mechanisms of their deformation. In particular, repeated loading leads to densification of glassy $Li_2B_4O_7$ along with an increase in its hardness. These processes occur mainly due to the variation of the angles and lengths of chemical bonds, which leads to a decrease in the free volume in the medium-order structure of glass, as well as a change in the coordination of boron atoms relative to oxygen, i.e., the transformation of three-coordinated boron into four-coordinated boron. A comparative analysis of the deformation processes of glassy and crystalline lithium tetraborate, as well as estimates of the average contact pressure, indicate that the amorphization of crystalline lithium tetraborate does not occur during nanoindentation. At the same time, direct structural studies of lithium tetraborate under high pressure using synchrotron X-rays seem promising.

Conflict of Interest

The authors declare no conflict of interest.

Acknowledgements

The authors are sincerely grateful to Prof. Vadym Holovey, PhD, for kindly providing samples for the study.

References

[1] Komatsu R, Sugawara T, Sassa K, Sarukura N, Liu Z, Izumida S, *et al*. Growth and ultraviolet application of $Li_2B_4O_7$ crystals: Generation of the fourth and fifth harmonics of Nd:Y3Al5O12 lasers. *Appl Phys Lett.* 1997;70(26):3492-4. doi: 10.1063/1.119210.

[2] Ezhov D, Turgeneva S, Nikolaev N, Mamrashev A, Mikerin S, Minakov F, *et al*. The potential of sub-THz-wave generation in $Li_2B_4O_7$ nonlinear crystal at room and cryogenic temperatures. *Crystals*. 2021;11(11):1321. doi: 10.3390/CRYST11111321.

[3] Sahil, Kumar R, Yadav MK, Kumar P. OSL and TA-OSL properties of $Li_2B_4O_7$:Al for radiation dosimetry. *J Alloys Compd*. 2022;908:164628. doi: 10.1016/J.JALLCOM.2022.164628.

[4] Mehrabi M, Zahedifar M, Hasanloo S, Nikmanesh H, Gheisari R, Li Y. Preparation and characterization of $Li_2B_4O_7$ nanoparticles co-doped with Mg and Cu for thermoluminescence dosimetry of gamma-rays. *Radiat Phys Chem*. 2022;194:110057. doi: 10.1016/J.RADPHYSCHEM.2022.110057.

[5] Puebla J, Hwang Y, Maekawa S, Otani Y. Perspectives on spintronics with surface acoustic waves. *Appl Phys Lett*. 2022;120(22):220502. doi: 10.1063/5.0093654.

[6] Wohlmuth D, Epp V, Bernhard Stanje, Welsch AM, Behrens H, Wilkening M. High-energy mechanical treatment boosts ion transport in nanocrystalline $Li_2B_4O_7$. *J Am Ceram Soc*. 2016;99(5):1687-93. doi: 10.1111/JACE.14165.

[7] Han X, Zhou W, Chen M, Luo L, Gu L, Zhang Q, *et al*. Liquid-phase sintering enabling mixed ionic-electronic interphases and free-standing composite cathode architecture toward high energy solid-state battery. *Nano Res*. 2022;15(7):6156-67. doi: 10.1007/s12274-022-4242-5.

[8] Deng R, Tao J, Zhong W, Wen L, Yang Y, Li J, *et al*. Tri-functionalized $Li_2B_4O_7$ coated $LiNi_{0.5}Co_{0.2}Mn_{0.3}O_2$ for boosted performance lithium-ion batteries. *J Alloys Compd.* 2023;940:168767. doi: 10.1016/j.jallcom.2023.168767.

[9] Pöhl F. Pop-in behaviour and elastic-to-plastic transition of polycrystalline pure iron during sharp nanoindentation. *Sci. Rep*. 2019;9:15350. doi: 10.1038/s41598-019-51644-5.

[10] Gouldstone A, Chollacoop N, Dao M, Li J, Minor AM, Shen YL. Indentation across size scales and disciplines: Recent developments in experimentation and modelling. *Acta Mater*. 2007;55(12):4015-39. doi: 10.1016/j.actamat.2006.08.044.

[11] Stus NV, Dub S, Stratiychuk DA, Lisnyak VV. Pop-in effect at nanoindentation of lithium tetraborate (100) face. *J Alloys Compd*. 2005;403(1-2):305-7. doi: 10.1016/j.jallcom.2005.04.205.

[12] Gurga A, Juliano T, Gogotsi Y, Dub S, Stus N, Stratiichuk D, *et al*. The mechanical properties of lithium tetraborate (100), (011) and (112) faces. *Mater Lett*. 2007;61(3):770-3. doi: 10.1016/j.matlet.2006.05.058.

[13] Nazarov MV, Nazarova TA, Dub SN, Banini GK. SEM and AFM studies on micro- and nanoindentation of material. *Microscopy Analysis*. 2003;9:13-5.

[14] Li Y, Lan G. Pressure-induced amorphization study of lithium diborate. *J Phys Chem Solids*. 1996;57(12):1887-90. doi: 10.1016/S0022-3697(96)00081-9.
[15] Chudoba T, Richter F. Investigation of creep behaviour under load during indentation experiments and its influence on hardness and modulus results. *Surf Coat Technol*. 2001;148(2-3):191-8. doi: 10.1016/S0257-8972(01)01340-8.
[16] Briscoe BJ, Fiori L, Pelillo E. Nano-indentation of polymeric surfaces. *J Phys D: Appl Phys*. 1998;31(19):2395-405. doi: 10.1088/0022-3727/31/19/006.
[17] Holovey VM, Puga PP, Turok II, Holovey MI, inventors; Institute of Electron Physics of the National Academy of Sciences of Ukraine, patent holder. Method for growth of single crystals of lithium tetraborate [Internet]. Patent of Ukraine No. 34204. 2001 Feb 15 [cited 16 Jan 2023]. Available from: https://sis.nipo.gov.ua/uk/search/detail/342653/.
[18] ISO 14577-1:2002 – Metallic materials – Instrumented indentation test for hardness and materials parameters – Part 1: Test method. [Internet]. 2002 [cited 2023 May 15]. Available from: https://www.iso.org/standard/30104.html.
[19] Oliver W, Pharr G. An improved technique for determining hardness and elastic modulus using load and displacement sensing indentation experiments. *J Mater Res*. 1992;7:1564-83. doi: 10.1557/JMR.1992.1564.
[20] Gaafar M, El-Batal F, El-Gazery M, Mansour S. Effect of doping by different transition metals on the acoustical properties of alkali borate glasses. *Acta Phys Pol, A*. 2009;115(3):671-8. doi: 10.12693/APhysPolA.115.671.
[21] Goldstein RV, Gorodtsov VA, Lisovenko DS, Volkov MA. Auxetics among 6-constant tetragonal crystals. *Lett Mater*. 2015;5(4):409-13. doi: 10.22226/2410-3535-2015-4-409-413.
[22] Campbell AC, Grolich P, Šlesinger R. Niget: Nanoindentation general evaluation tool. *SoftwareX*. 2019;9:248-54. doi: 10.1016/j.softx.2019.03.001.
[23] Makishima A, Mackenzie J. Direct calculation of Young's modulus of glass. *J Non-Cryst Solids*. 1973;12(1):35-45. doi: 10.1016/0022-3093(73)90053-7.
[24] Makishima A, Mackenzie J. Calculation of bulk modulus, shear modulus and Poisson's ratio of glass. *J Non-Cryst Solids*. 1975;17(2):147-57. doi: 10.1016/0022-3093(75)90047-2.
[25] Nowicki M, Richter A, Wolf B, Kaczmarek H. Nanoscale mechanical properties of polymers irradiated by UV. *Polymer*. 2003;44(21):6599-606. doi: 10.1016/S0032-3861(03)00729-8.
[26] Gilbert JL, Cumber J, Butterfield A. Surface micromechanics of ultrahigh molecular weight polyethylene: Microindentation testing, crosslinking, and material behavior. *J Biomed Mater Res*. 2002;61(2):270-81. doi: 10.1002/jbm.10143.
[27] Novikov NV, Dub SN, Milman YV, Gridneva IV, Chugunova SI. Application of nanoindentation method to study a semiconductor-metal phase transformation in silicon. *J Superhard Mater*. 1996;18:32-40.
[28] Dub S, Novikov N, Milman Y. The transition from elastic to plastic behaviour in an Al-Cu-Fe quasicrystal studied by cyclic nanoindentation. *Philos Mag A*. 2002;82(10):2161-72. doi: 10.1080/01418610208235725.
[29] Agilent Technologies. Nano indenter G200 User manual. [Internet]. 2012 [cited 2022 Dec 11]. Available from: https://www.manualslib.com/manual/1254115/Agilent-Technologies-Nano-Indenter-G200.html.
[30] Weaver MA, Stevenson M, Bradt RC. Knoop microhardness anisotropy and the indentation size effect on the (100) of single crystal NiAl. *Mater Sci Eng*. 2003;345(1-2):113-7. doi: 10.1016/S0921-5093(02)00454-9.
[31] Mukhopadhyay NK, Paufler P. Micro- and nanoindentation techniques for mechanical characterisation of materials. *Int Mater Rev*. 2006;51(4):209-45. doi: 10.1179/174328006X102475.
[32] Sidek H, Saunders G, James B. The pressure and temperature dependences of the elastic behaviour of lithium tetraborate. *J Phys Chem Solids*. 1990;51(5):457-65. doi: 10.1016/0022-3697(90)90184-H.
[33] Inaba S, Fujino S, Morinaga K. Young's modulus and compositional parameters of oxide glasses. *J Am Ceram Soc*. 2004;82(12):3501-7. doi: 10.1111/j.1151-2916.1999.tb02272.x.
[34] Adamiv VT. Thermal properties of alkaline and alkaline-earth borate glasses. *Funct Mater*. 2013;20(1):52-8. doi: 10.15407/fm20.01.052.
[35] Inaba S, Oda S, Morinaga K. Heat capacity of oxide glasses at high temperature region. *J Non-Cryst Solids*. 2003;325(1-3):258-66. doi: 10.1016/S0022-3093(03)00315-6.
[36] Saddeek YB. Structural analysis of alkali borate glasses. *Phys B*. 2004;344(1-4):163-75. doi: 10.1016/j.physb.2003.09.254.
[37] Cheng Y, Cheng C. Scaling, dimensional analysis, and indentation measurements. *Mater Sci Eng: R: Reports*. 2004;44(4-5):91-149. doi: 10.1016/j.mser.2004.05.001.

[38] Attaf M. New ceramics related investigation of the indentation energy concept. *Mater Lett*. 2003;57(30):4684-93. doi: 10.1016/S0167-577x(03)00375-6.
[39] Milman Y, Galanov B, Chugunova S. Plasticity characteristic obtained through hardness measurement. *Acta Metall Mater*. 1993;41(9):2523-32. doi: 10.1016/0956-7151(93)90122-9.
[40] Kilymis DA, Delaye J. Deformation mechanisms during nanoindentation of sodium borosilicate glasses of nuclear interest. *J Chem Phys*. 2014;141(1):014504. doi: 10.1063/1.4885850.
[41] Rouxel T, Ji H, Guin JP, Augereau F, Rufflé B. Indentation deformation mechanism in glass: Densification versus shear flow. *J Appl Phys*. 2010;107(9):094903. doi: 10.1063/1.3407559.
[42] Wang JG, Choi BW, Nieh TG, Liu CT. Crystallization and nanoindentation behavior of a bulk Zr-Al-Ti-Cu-Ni amorphous alloy. *J Mater Res*. 2000;15(3):798-807. doi: 10.1557/JMR.2000.0114.
[43] Lee SK, Eng PJ, Mao H, Meng Y, Shu J. Structure of alkali borate glasses at high pressure: B and LiK-Edge inelastic X-Ray scattering study. *Phys Rev Lett*. 2007;98(10):105502. doi: 10.1103/PhysRevLett.98.105502.

Пружно-пластичні властивості $Li_2B_4O_7$ досліджені шляхом наноіндентування

Ірина Василівна Чобаль
Асистент
Ужгородський національний університет
88000, пл. Народна, 3, м. Ужгород, Україна
https://orcid.org/0009-0002-5021-5184

Олександр Ілліч Чобаль
Кандидат фізико-математичних наук, доцент
Ужгородський національний університет
88000, пл. Народна, 3, м. Ужгород, Україна
https://orcid.org/0000-0002-8042-8052

Юлія Михайлівна Мисло
Кандидат фізико-математичних наук, доцент
Ужгородський національний університет
88000, пл. Народна, 3, м. Ужгород, Україна
https://orcid.org/0000-0001-6771-2844

Іван Петришинець
Кандидат технічних наук, провідний науковий співробітник
Інститут матеріалознавства Словацької Академії Наук
04001, вул. Ватсонова, 47, м. Кошице, Словаччина
https://orcid.org/0000-0001-8001-5349

Василь Михайлович Різак
Доктор фізико-математичних наук, професор
Ужгородський національний університет
88000, пл. Народна, 3, м. Ужгород, Україна
https://orcid.org/0000-0002-9177-0662

Анотація

Актуальність. Кристалічний і аморфний тетраборат літію ($Li_2B_4O_7$) має широкі можливості практичного застосування завдяки своїм фізичним властивостям. Знання механічних характеристик поверхневих шарів цих матеріалів, що досліджуються шляхом наноіндентування, є важливим для оптимізації технологічних процесів отримання «оптично ідеальних» зразків.

Мета. Порівняльне вивчення механічних властивостей і механізмів деформації склоподібних та кристалічних зразків $Li_2B_4O_7$ в широкому діапазоні прикладених навантажень.

Методологія. Пружно-пластичні властивості кристалічного та склоподібного тетраборату літію досліджено методом багаторазового циклічного наноіндентування. Зразки вимірювали за допомогою максимальної сили навантаження 50, 100, 150, 200, 250, 300, 350, 400, 450 та 500 мН. Виконано чотири вимірювання (у вигляді матриці 2x2) на відстані 50 мкм одне від одного на кожному зразку та при кожному навантаженні. Модуль Юнга, твердість і коефіцієнт Пуассона скла $Li_2B_4O_7$ також було розраховано в рамках теорії Makishima-Mackenzie.

Результати. Отримано криві навантаження-розвантаження та графіки залежності середнього контактного тиску від переміщення алмазного індентора Берковича, що мають «гладку» форму та відсутність аномалій, які пов’язують з «pop-in» або «pop-out» ефектами. Із експериментальних *P-h* діаграм навантаження – переміщення отримано значення модуля індентування (модуль Юнга *E*) і значення твердості *H* досліджуваних зразків. Виміряні значення переважно залежать від прикладеного навантаження або контактної глибини проникнення індентора в кристалічний і склоподібний тетраборат літію.

Висновки. Як твердість, так і модуль Юнга скла $Li_2B_4O_7$ є меншими порівняно з відповідними даними монокристалу, що вказує на нижчу стійкість аморфного тетраборату літію до пружних і пластичних деформацій. Отримані експериментальні значення твердості та модуля Юнга скла $Li_2B_4O_7$ добре корелюють з результатами розрахунку в рамках теорії Makishima-Mackenzie. Багаторазове циклічне наноіндентування призводить до деформаційного ущільнення склоподібного $Li_2B_4O_7$ за рахунок зміни кутів і довжин хімічних зв’язків, що веде до зменшення вільного об’єму в структурі середнього порядку скла, а також зміни координації атомів Бору відносно Оксигену, тобто перетворення три-координованого Бору в чотири-координований

Ключові слова: кристали тетраборату літію; скло Li_2O-$2B_2O_3$; деформаційне ущільнення; модуль Юнга; твердість; фазовий перехід

НАУКОВИЙ ВІСНИК
УЖГОРОДСЬКОГО УНІВЕРСИТЕТУ
СЕРІЯ «ФІЗИКА»

Науковий журнал

Випуск 53. 2023

Заснований у 1997 р. Виходить двічі на рік

Оригінал-макет видання виготовлено
у редакційно-видавничому відділі Ужгородського національного університету

Відповідальний редактор:
Г. Івченко

Редагування англомовних текстів:
С. Воровський, К. Касьянов

Комп'ютерна верстка:
М. Кришталь

Підписано до друку 20.06.2023 р. Формат 60*84/8
Умовн. друк. арк. 7,6
Наклад 300 примірників

Адреса видавництва:
ДВНЗ «Ужгородський національний університет»
88000, вул. Університетська, 54, м. Ужгород
Закарпатська область, Україна
тел/факс: (03122) 3-20-24
E-mail: info@physics.uz.ua
www: https://physics.uz.ua/uk

SCIENTIFIC HERALD
OF UZHHOROD UNIVERSITY
SERIES “PHYSICS”

Scientific Journal

Issue 53. 2023

Founded in 1997. Published two times per year

The original layout of the publication is made
in the publishing department of Uzhhorod National University

Managing editor:
H. Ivchenko

Editing English-language texts:
S. Vorovsky, K. Kasianov

Desktop publishing:
M. Kryshtal

Signed for print 06/20/2023. Format 60*84/8
Conventional printed pages 7.6
Circulation 300 copies

Publishing Address:
Uzhhorod National University
88000, 14 Universytetska Str., Uzhhorod
Transcarpathian region, Ukraine
Tel./fax: (03122) 3-20-24
E-mail: info@physics.uz.ua
www: https://physics.uz.ua/en